JOINT INVERSION OF SURFACE WAVE DISPERSION AND RECEIVER FUNCTIONS FOR CRUSTAL STRUCTURE IN OKLAHOMA

Hao Guo, B.S.

A Thesis Dissertation Presented to the Graduate Faculty of
Saint Louis University in Partial Fulfillment
of the Requirements for the Degree of
Master of Science

2015

COMMITTEE IN CHARGE OF CANDIDACY:

Reinert Chair Professor Robert Herrmann，
Chairperson and Advisor

Professor Lupei Zhu

Professor John Encarnación

TABLE OF CONTENTS

LIST OF TABLES

LIST OF FIGURES

CHAPTER 1: INTRODUCTION

Oklahoma has been "seismically quiet" for a long time until shortly after the sharp increase in earthquakes began in 2008 (Figure 1.1). Numerous studies in the past few years have suggested that massive fluid injection, especially of wastewater, might be the determining factor of the increased seismicity in Oklahoma (Keranen *et al.*, 2014; Keranen *et al.*, 2013, Hough, 2014). Figures 1.2 and 1.3 illustrate the distribution of active injection wells and earthquakes since 2008 in Oklahoma, respectively. The coincidence in the locations of the wells and earthquakes (especially in central Oklahoma) implies some connection between them. However, a new paper, published in 2015, does not draw a link between the fluid injection and the earthquakes. Instead, it focuses on reactivated hidden and old faults that are the locations of causing the increased occurrence of earthquake in Oklahoma (McNamara *et al.*, 2015). The cause of the reactivation was not identified. The relation between the fluid injection and old faults remains a significant unsolved problem.

The basis for understanding and solving this problem is a well-established seismic velocity model, which is important for defining accurate earthquake locations for a high-precision earthquake catalog. In this study, a joint inversion of surface wave dispersion and teleseismic P-wave receiver functions is performed to develop the 1-D S-wave velocity models at selected locations in Oklahoma. Figure 1.4 shows the area of the study.

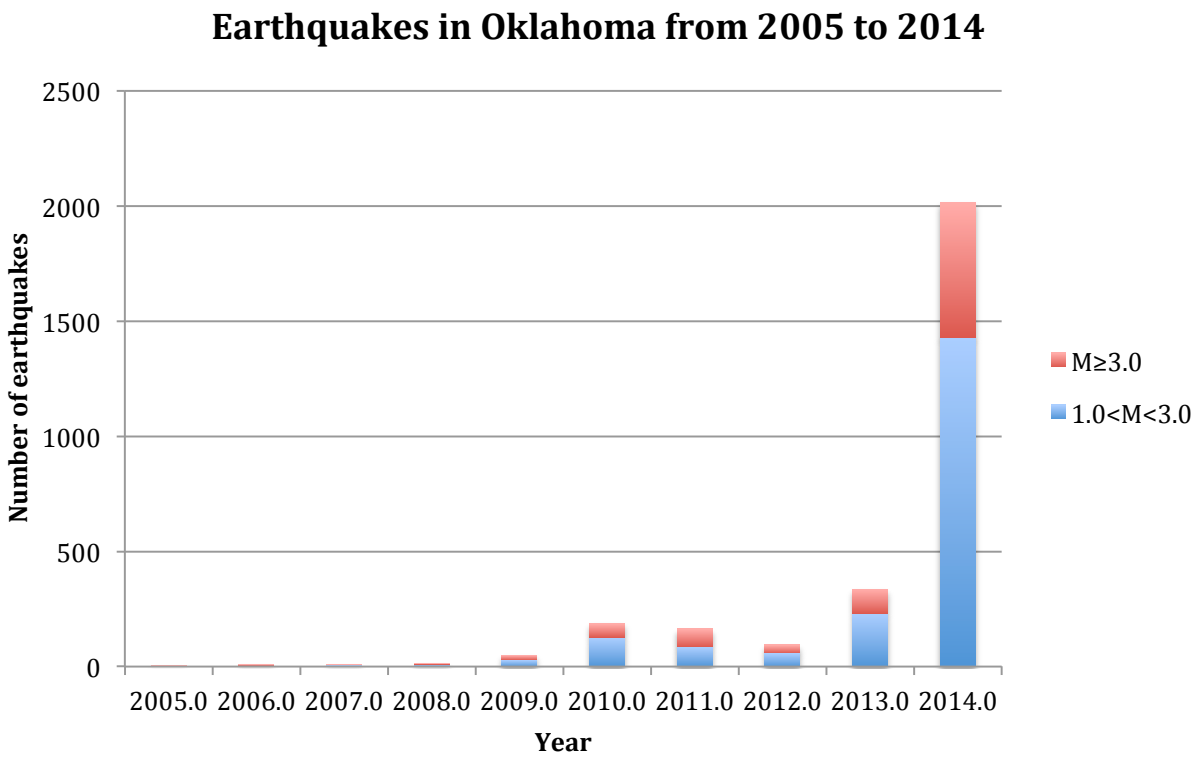

Figure 1.1: The number of earthquakes from 2005 to 2014 in Oklahoma. Red: Magnitude of earthquake is higher than or equal to 3.0. Blue: Magnitude of earthquake is smaller than 3.0 (USGS NEIC earthquake catalog).

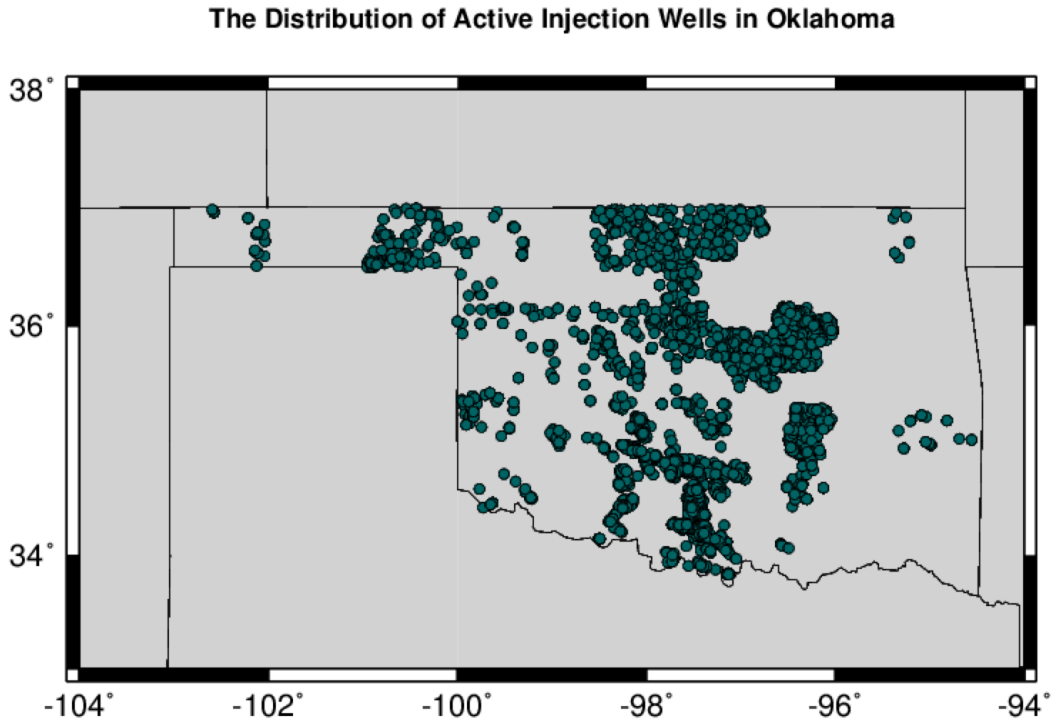

Figure 1.2: The distribution of active injection wells in Oklahoma (Oklahoma Corporation Commission well data).

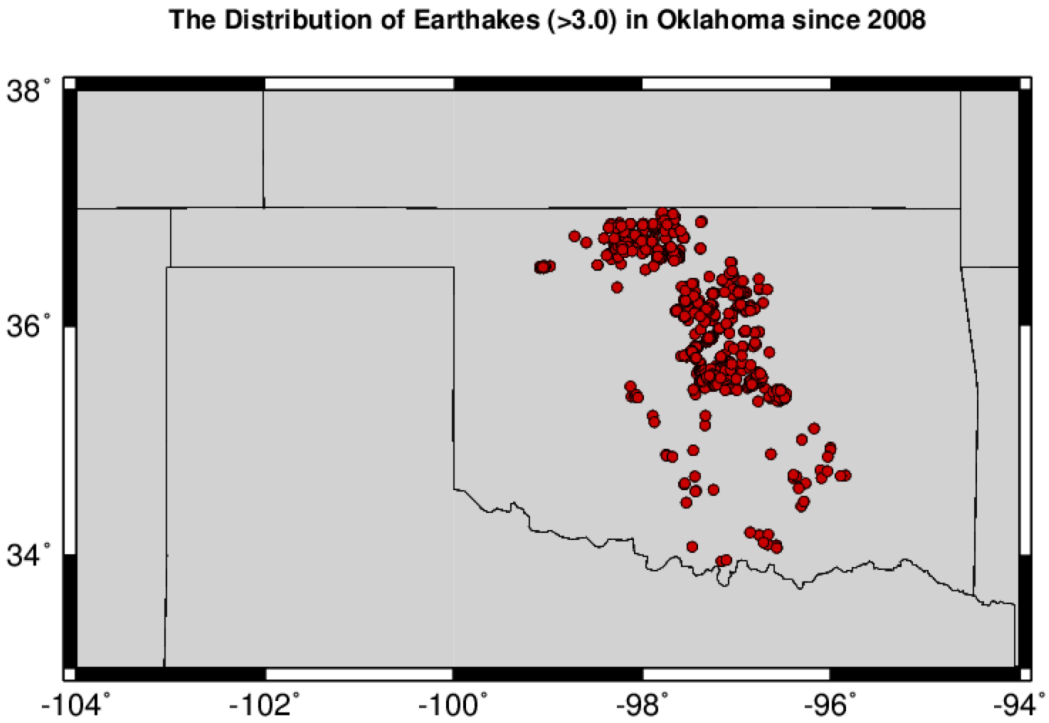

Figure 1.3: The distribution of earthquakes (M>3.0) in Oklahoma (USGS NEIC earthquake catalog).

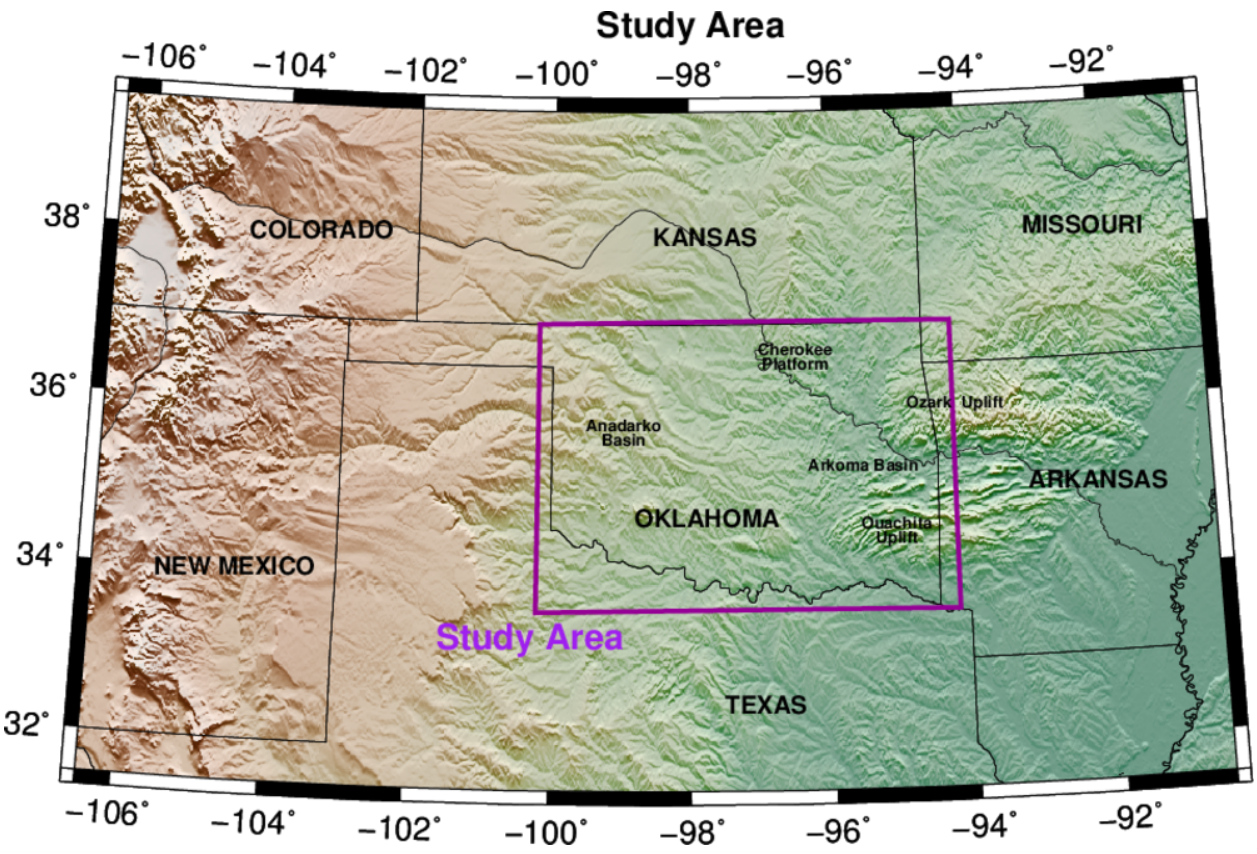

Figure 1.4: Study area.

1.1 Seismic Activity

Oklahoma has experienced a dramatic increase in seismicity since 2008. According to previous studies, Oklahoma had not only almost half (45%) of the small magnitude seismicity, but also the majority of larger earthquakes occurring in central United States between 2008-2013 (Keranen *et al.*, 2014). On November 5, 2011, an earthquake with M_w of 5.6 occurred in central Oklahoma. Based on the report from U.S Geological Survey, it was the largest and most powerful earthquake ever located in Oklahoma, and also one of the two largest earthquakes in the central and eastern U.S in a century. The earthquake had shaking intensity level of VIII

(heavily damaging), injured 2 people and damaged many buildings ("Magnitude 5.6 – Oklahoma, Earthquake Summary", 2011).

In general, the increased volume of wastewater disposed underground gradually raises the pore pressure in subsurface, which will spread out in every direction until it encounters faults, including previously dormant faults. As the pressure applied on faults increases, the faults will be eventually moved out of the "locked" positions when the pressure reaches a critical threshold (Keranen et al., 2014). Earthquakes will be triggered at the same time. Normally, the rupture of a large fault causes a large earthquake (Keranen et al., 2013). For instance, the earthquake mentioned above was controlled by the Wilzetta Fault zone, which is a 55 miles long strike-slip fault system that triggered not only the largest earthquake (M_w 5.6), but also a sequence of aftershocks.

Similar anomalous earthquakes were also recorded in other states, such as the M_w 4.8 earthquake near Timpson, East Texas in May 2012, and the M_w 4.0 earthquake near Youngstown, Ohio in Dec 2011 (Frohlich *et al.*, 2014). One of the most significant common features in those states is the flourishing oil and/or gas production. In Ohio, some oil companies use the hydraulic fracturing method to extract the gas from shale rocks, in which a large amount of wastewater is injected to increase the pressure ("Ohio Quakes Probably Triggered by Waste Disposal Well, Say Seismologists", 2012).

Recently, a new study suggests that the reactivation of hidden old faults, formed as a result of extensive orogeny during the Pennsylvanian Period, might be capable of producing

earthquakes (McNamara *et al.*, 2015). In addition, these shallow (< 6km) and vertically oriented ancient faults continuously raise the potential threat to people's lives and property. However, that study focused on the formation and orientation of the faults instead of the trigger of the earthquake, but it still provides a way to assess the earthquake hazards.

1.2 Geological background

The regions (Figure 4) covered by the seismic stations include the state of Oklahoma, which underwent many complete cycles of marine regression and transgression during its geologic history (Johnson and Luza, 2008). The oldest rock in Oklahoma is the Precambrian igneous and metamorphic rock, which gradually eroded and subsided underground, and then formed basement. Today, the rock is exposed in Wichita and Arbuckle Mountains due to the orogeny in Pennsylvanian Period and erosion in Cenozoic Era. During the Ordovician, Silurian and Devonian Periods, Oklahoma was tectonically quiet, except for a widespread uplift and erosion in Late Devonian. Limestone and dolomite formation dominated in this period due to the shallow marine environment. Similar to the Ordovician and Silurian Period, the shallow sea covered most of Oklahoma during Mississippian Period. Limestone was accumulated, and formed the thick carbonate sequences. The only important geological event was a rapidly subsided basin in southern Oklahoma where a large amount of sediments deposited, forming thick layers of limestone and sandstone.

The most important and complicated period in Oklahoma is the Pennsylvanian Period, which

lasted roughly from 323 million years ago to 299 million years ago (Walker *et al.*, 2012). Both rapid basin subsidence and intense mountain building activity occurred in this period. For example, the Wichita, Arbuckle, and Ouachita Uplifts, as the most notable feature in the southern Oklahoma, were formed by orogeny. Unlike the other two uplifts, the Ouachita uplift is dominated by sedimentary strata with intense folds and faults instead of igneous strata. Meanwhile, rapid subsidence occurring at the same period resulted in the current basin structure, which is represented by two major basins, Arkoma Basin and Anadarko Basin. These basins also received abundant sediments from the erosion of mountains during the subsiding process. Those sediments eventually formed Pennsylvanian rock, which occurs as marine shale that formed most of the petroleum reservoirs in Oklahoma. The Pennsylvanian sediments contain abundant fossils, including invertebrate and plant, which are the perfect source for the formation of oil and gas. In addition, several large fault systems, such as Wilzetta fault zones, formed in central Oklahoma as a result of orogeny in this period. Each fault system contains many faults, which can be considered as the traps that preserve oil and gas (Luza and Lawson, 1982).

Following the Pennsylvanian Period, the Permian Period was relatively quiet. Most of Oklahoma was covered by shallow sea in the entire Permian Period except for the Late Permian Period, which suggests that a large scale of regression occurred in this period, and lasted until at least the end of the Permian Period. In the Mesozoic Era, Oklahoma went through a complete transgression and regression cycle. A broad uplift of Oklahoma caused the regression in the Late Cretaceous, and formed today's major uplifts, such as Ouachita Uplift.

1.3 Purpose of the Study

The induced earthquake has become a major threat to people's lives and property in recent years. A high-precision earthquake catalog for Oklahoma including the actual locations of earthquakes should be developed as soon as possible to assess earthquake-shaking hazards. The key to relocating earthquakes is a well-established velocity model, which can also be used to assess the earthquake hazards by generating simulations of shaking from known sources.

This study is divided into 4 parts to address the goal of developing crustal velocity structures. First we will obtain the surface wave dispersion maps across Oklahoma on a 25 × 25 km grid that images shallow geological structures. Second, we will compute the receiver functions of selected seismic stations. Third, 1-D crustal models will be developed at selected locations through a joint inversion of receiver functions and surface-wave dispersion. The S-wave velocity model is obtained in this step. Finally, the reliability of velocity models will be tested by performing a series of forward modeling studies using data sets not included into the joint inversion.

1.3.1 Surface wave dispersion

The basic idea of ambient noise surface wave tomography is that the surface wave empirical Green functions can be extracted from cross-correlations of ambient noise data recorded by two seismic stations. Phase velocity dispersion can then be estimated from the empirical Green functions (Snieder, 2004). In this study, I estimate group and phase velocity data for each station

pair by following the procedure of the modified multiple filter analysis (Herrmann and Ammon, 2002), which was introduced by Dziewonski *et al.* (1969) and Herrmann (1973). The last step of this section is to perform a tomography study to define the spatial variation of the phase and group velocity dispersion across the study region. A damped least-square tomographic inversion developed by Dr. C. Ammon (personal communication) is used.

1.3.2 Joint inversion

The receiver functions are obtained by iterative, time-domain deconvolution (Ligorria and Ammon, 1999). I follow the theory introduced by Herrmann and Ammon (2002) to invert two different data sets including the dispersion data and receiver functions to estimate the shear wave velocity models for selected stations, which are also constrained by geological information. The derived velocity models not only match the observed receiver functions and dispersion well, but also provide more information at shallow depths than previous studies.

1.3.3 Forward tests of velocity models

While determining regional moment tensors for earthquakes in Oklahoma, Herrmann (personal communication) noted an interesting character on the transverse components of some stations. These recordings showed a sequence of pulses that could be interpreted as S-waves reverberating in the shallow sedimentary layers. I test the joint inversion velocity models by generating theoretical transverse waveforms at these selected seismic stations. By comparing the

observed waveforms for real earthquakes and the theoretical waveforms, the agreements in timing and appearance of multiples with distance will provide confidence in the local velocity models so that it can be used by others to study the hypocenter relocation in the region.

CHAPTER 2: LITERATURE REVIEW

Numerous geophysical investigations had been conducted in central United States. Some studies provide the crustal structure over large scales that cover Oklahoma (e.g., Kane and Godson, 1989; van der Lee and Nolet, 1997); however, the resolution of their models is limited to a few hundreds of kilometers. The seismic velocity structure with high resolution has not yet been released.

2.1 Gravity/magnetic and seismic reflection studies

The gravity and magnetic data have been used in studies of the composition and structure of the continental crust in North America (e.g., Kane and Godson, 1989; Jachens *et al.*, 1989). Kane and Godson (1989) used millions of gravity observations to obtain both short-wavelength (<250 km) and long-wavelength (>1000 km) gravity maps across the United States, which reveal the major tectonic regions and the causes of the tectonic events in the United States.

Geophysicists have also conducted several seismic reflection experiments since 1980. For example, Phinney and Roy-Chowdhury (1989) used the seismic reflection transects running across the Ouachita Mountains to study the crustal structure of Ouachita orogen, which is caused by an important orogeny during the late Paleozoic. Although the resolution of their crustal images is limited due to the sparse distribution of the reflection lines and the presence of noise, they provide a framework of the structure and evolution of the orogen. However, the seismic reflection method is typically designed to study local crustal structures, and larger features, such

as seismic zones and orogenic belts, are not investigated due to cost. Thus reflection techniques might not be the best way to study the crustal structure over a large area, such as Oklahoma.

2.2 Seismic body wave tomography study

It is apparent that the lack of large earthquakes and the relatively sparse distribution of seismic stations resulted in the limited observational seismic data, which prevented the use of seismic body wave tomography study in Oklahoma. Recently, the USArray Transportation Array (TA) with a station spacing of about 70 km was deployed across Oklahoma, and its purpose was to study the upper mantle structure. In a new paper, published in 2014, Evanzia *et al.* (2014) produced more accurate Vp and Vs tomographic models across Texas and Oklahoma by combining the data from TA stations with other two seismic networks (the SIENCAR and GCP) instead of using the TA stations alone. However, they had not yet solved the limitation of the body wave tomography. Although they revealed more details about the seismic velocity variations in the crust and upper mantle, the resolution is still limited, especially in the crust. The newly added two networks are distributed in the southeast of New Mexico and a small region of Gulf Coastal Plain, respectively. Due to the lack of coverage of the new network, they only used TA stations to produce the velocity models in Oklahoma. In addition, the crustal expression of the geological structure (about 100 km wide) in southern Oklahoma is close to the spacing of TA stations (70 km). The geological features look “fuzzy”, and they are difficult to be identified in their models.

2.3 Surface wave tomography study

A number of early geophysical studies (before the 2000's) focus on surface-wave tomography. They used teleseismic earthquake events to produce an S-wave velocity model (e.g., Alsina *et al.*, 1996; Van der Lee and Nolet, 1997; Ekström *et al.*, 1997). For example, Van der Lee and Nolet (1997) obtained the upper mantle S-wave velocity models across North America by using the inversion of Rayleigh waves. They found some interesting features that showed velocity anomalies in the mantle transition zone, but the structure of crust is poorly resolved in this study. Normally, in an aseismic region, it is difficult to obtain the earthquake data at short periods (<20s) due to the attenuation of the signals due to long propagation, which results in the lack of constraints for the crust velocity structure in early studies (Bensen *et al.*, 2008).

Fortunately, this situation has been gradually changed in the last decade. Shapiro *et al*. (2005) demonstrated that the cross-correlation of signals of ambient seismic noise between 2 stations could yield data to estimate the surface-wave measurements at short periods, even through the station spacing is relatively sparse. The TA network obviously became an ideal seismic network for studying of crust structure by using ambient noise surface wave tomography. Previous studies had developed surface-wave dispersion maps on both regional (e.g., Lin *et al.,* 2008; Liang and Langston, 2008) and continental scale (e.g., Bensen *et al.,* 2008; Ekström *et al.*, 1997) across the United States. However, the majority of regional studies had relatively large scales that did not focus on Oklahoma as the results of lack seismicity and the sparse inter-station ray path coverage. Although some studies of continental scale cover Oklahoma, the resolution of those dispersion

maps is relatively low (~100 × 100 km grid). For instance, using the LH (1 Hz sample interval) waveforms, Bensen *et al.*, (2008) presented surface-wave tomographic dispersion maps at periods between 8s and 40s across the contiguous United States, which are parameterized on 100 × 100 km grids. This resolution enables them to study the relatively large geological and tectonic structures (such as deep sediments in the Gulf of Mexico) on a continental scale, but it is not good enough to develop seismic velocity models in regional scale (such as Oklahoma). Similarly, while this study provides lots of information about geological features in the crust and uppermost mantle beneath the United States, the structure in the upper crust is difficult to be recognized in their dispersion maps due to the insufficient measurements at shorter periods (< 8 s). In fact, most of the recent seismicity in Oklahoma is located at uppermost crust (upper 10 km of the crust). Thus the well-established surface dispersion at shorter periods is necessary to construct the velocity model that forces on the upper crust.

Most recently, Ekström (2014) presented high-resolution (0.25° × 0.25° grid) phase velocity dispersion maps at periods from 5 s to 40 s of the western and central U.S., which appear to be the highest resolution dispersion maps ever obtained. Compared to Bensen's study, a larger data set recorded on 1600 USArray stations was used in Ekström's paper to compute the dispersion. In his study, he applied two-step process to eliminate the influence of the outliers in the data set. In the first step, all of the data were included to construct a coarse tomographic dispersion model (0.5° × 0.5° grid). The misfit of data was then used to identify the outliers, and determine the phase-velocity uncertainty (Ekström, 2014). This step makes those bad data exert

much less influence on the final inversion. In the second step, He computed the inversion on a finer grid (0.25° × 0.25°), and the high resolution dispersion maps were finally determined after the inversion (Ekström, 2014), which illustrate velocity anomalies of major shallow geological structures in western and central United States. However, there are still some limitations in the study. For example, they did not provide any group velocity analysis, considering that group velocity may be more sensitive to shallow structures than phase velocity.

2.4 S-wave velocity model study

The seismic velocity model study has always been a hot research field, since it is the key to build a high-precision earthquake catalog, which is usually used to assess the earthquake hazards. Numerous velocity model studies had been conducted in the central United States. Although most of them focus on New Madrid Seismic Zone (e.g., Chiu et al., 1992; Langston and Horton, 2014), there are velocity models are also available for source inversion in Oklahoma; even through they were designed on a large scale (e.g., Herrmann and Ammon, 1997; Pollitz and Mooney, 2014). For example, Herrmann et al. (2011) states that the velocity model constructed for the mid-continent region can be used to model the relatively small regions. They present two velocity models, the central United Stated model (CUS) and the western United States model (WUS), respectively. The WUS was designed for the mountain region, and has been used for recent earthquake relocation studies in Oklahoma (e.g., McNamara et al., 2015). In another study, Ramírez-Guzmán et al., (2012) developed a new 3-D seismic velocity models for the Central U.S,

which combines the results of decades of crustal research, and provide the most detailed information about the crustal structure. Although the coverage of that study did not include Oklahoma, it can still be considered as an important reference for the study of velocity structure in Oklahoma. However, both of the two studies focus on relatively large spatial scales. It is still necessary to build a new velocity for Oklahoma based on the regional seismic data and geological information. In addition, the uppermost part of the crust, where the majority of triggered earthquakes in Oklahoma occurred in this region, is not well constrained in the previous models. In other words, the earthquake catalog for Oklahoma constructed by using either model of the two studies might not provide the best estimation of hypocentral parameters.

CHAPTER 3: METHODOLOGIES

3.1 Surface wave analysis

Seismic waves are the waves that travel through and around the Earth, which are caused by the release of energy from earthquakes or explosions. Normally, they are classified as body waves and surface waves in terms of the different properties, such as the wave speed and the propagation direction. For example, body waves include the P-wave (or primary wave) and the S-wave (or shear wave), which propagate through the interior of the Earth, whereas, the surface waves travel along the Earth's surface, and decay in amplitude with respect to depth. On a seismogram (Figure 3.1), the strongest arrivals for shallow earthquakes are the surface waves, which arrive at a seismometer just after the body waves, and usually cause heavy damage and destructions to the foundations of structures.

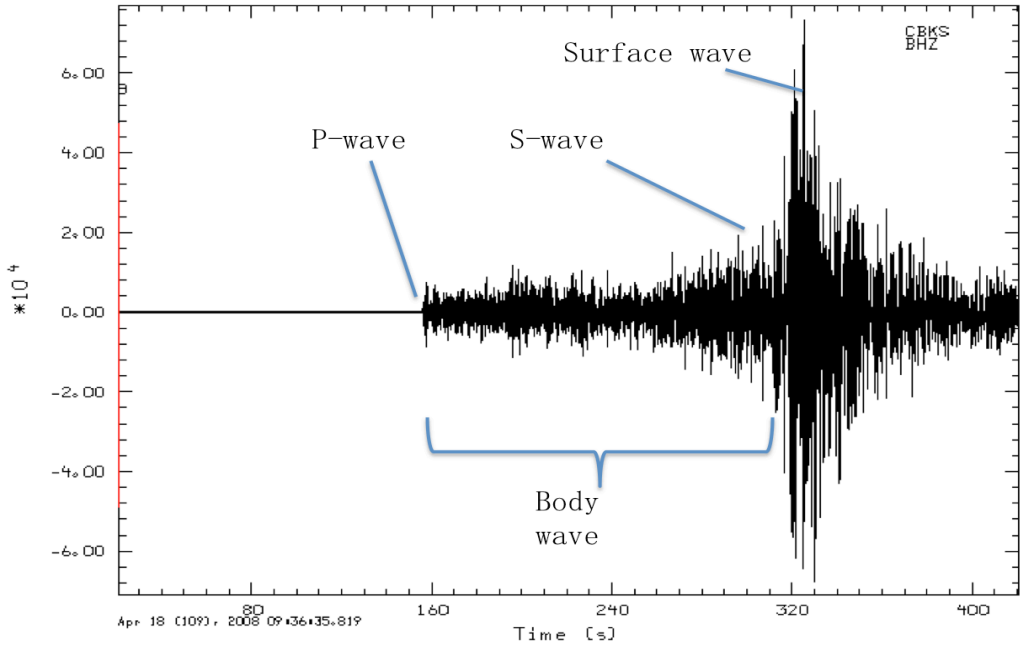

Figure 3.1: A typical seismogram (BHZ channel) recorded at station CBKS from the M_w5.2 earthquake in Illinois.

3.1.1 Rayleigh wave and Love wave

Similar to body waves, surface waves are also divided into two categories: Rayleigh waves and Love waves, respectively. The Rayleigh wave is named for Lord Rayleigh, who first described this type of surface wave in 1885. Figure 3.2 (a) shows the particle motion of a Rayleigh wave, which moves along a counterclockwise elliptical trajectory in the vertical – radial plane. The particle motion can provide the information about the wave propagation direction, which is revealed by the motion of the elliptical trajectory. Rayleigh waves travel relatively slower than other seismic waves in most cases. For instance, they usually appear as the last seismic waves on the vertical and horizontal components on seismograms. For a halfspace, the Rayleigh wave gives a velocity to about 0.91 of the S-wave's velocity. An important

characteristic of Rayleigh waves propagation in a more realistic medium is the dispersion, which means the waves travel with different speeds at the different periods.

The Love wave is another type of surface wave. It is named for A. E. H. Love, who found that the SH waves within a low-velocity layer at the Earth surface might generate a new type of surface waves in some cases. Love waves vibrate in the horizontal plane, and perpendicular to the direction of wave propagation (Figure 3.2 b). Similar to Rayleigh waves, Love waves also show dispersion, but they generally travel faster than Rayleigh waves. Moreover, the velocity dispersion of the Love wave (V_L) varies between the two velocities of S-wave ($\beta_1 < V_L < \beta_2$) where the β_1 and β_2 are the velocities of S-wave at the surface and underlying half-space, respectively, for a simple single layer over a halfspace model.

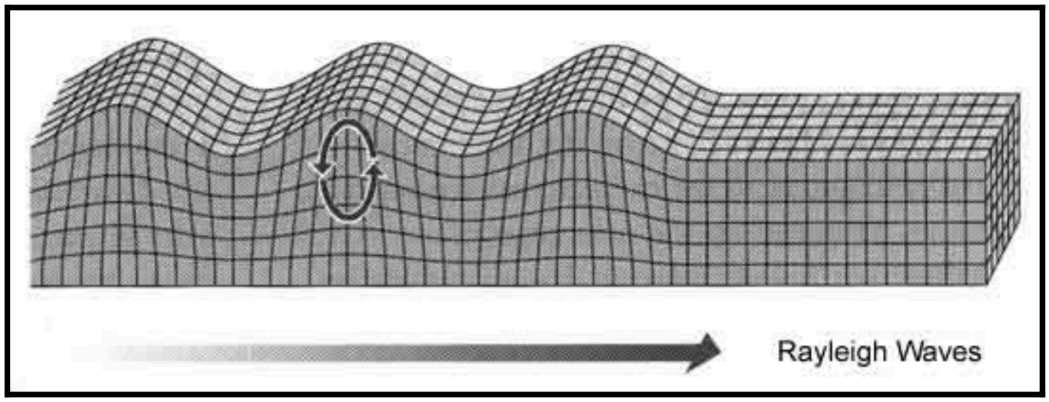

(a)

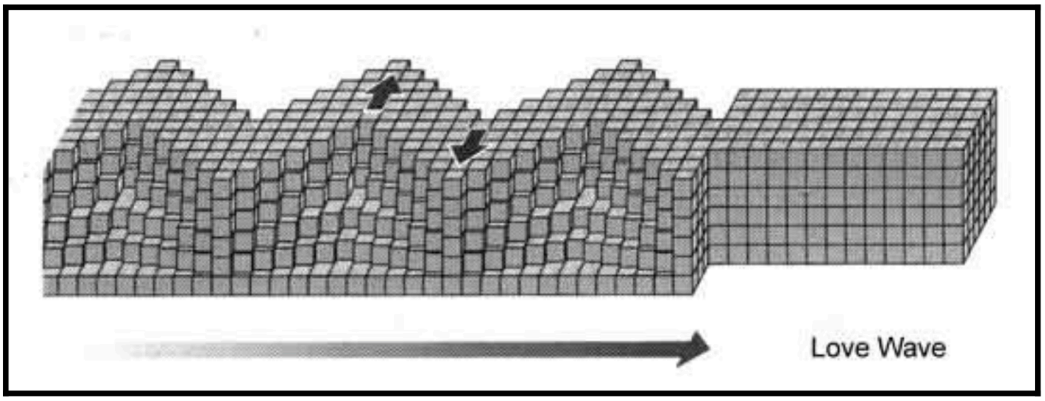

(b)

Figure 3.2: Surface waves travel through a medium. (a) Rayleigh wave; (b) Love wave. ("Types of Earthquake waves")

3.1.2 The dispersion of surface waves

One of the most important characteristics of surface waves is dispersion, which plays an important role in studying the crust and the upper mantle structures. Surface waves are normally dispersive in a vertically heterogeneous medium (different horizontal layers with different mechanical properties), which means that different velocities are corresponding to different periods. Usually, surface waves with longer periods travel faster than those with shorter periods,

since they are sensitive to the deeper structure of the Earth. Thus, the velocity of the surface wave has a function that is related to the period instead of the depth.

If a wave, such as a sinusoidal wave, propagates with a constant wavelength, every point on this wave will move with the phase velocity (c). However, a surface wave usually propagates through a medium as the envelope of the wave packet, which contains a spectrum of wavelengths. The phase velocity alone cannot thoroughly describe the features of the surface wave, since it is much more complicated than a simple harmonic wave. Thus, we use another wave velocity, called group velocity (U), to represent the speed of the envelope of the wave packet. Figure 3.3 shows the difference between the phase velocity and the group velocity.

Phase velocity can be defined as:

$$c = \omega/k, \tag{3.1}$$

where ω refers to the angular frequency. k is the wave number, and $k = 2\pi/\lambda$. We also have the relation $\omega = \omega(k)$.

The group velocity is related to the phase velocity by:

$$U = \frac{d\omega}{dk}. \tag{3.2}$$

From the relations above, we have:

$$U = \frac{d}{dk}(ck) = c + k\frac{dc}{dk} = c - \lambda\frac{dc}{d\lambda}, \tag{3.3}$$

where λ is the wavelength.

In the usual case, the phase velocity increases with increasing the wavelength. Thus the group velocity is slower than the phase velocity, since $dc/d\lambda$ are positive in Eq. (3.3).

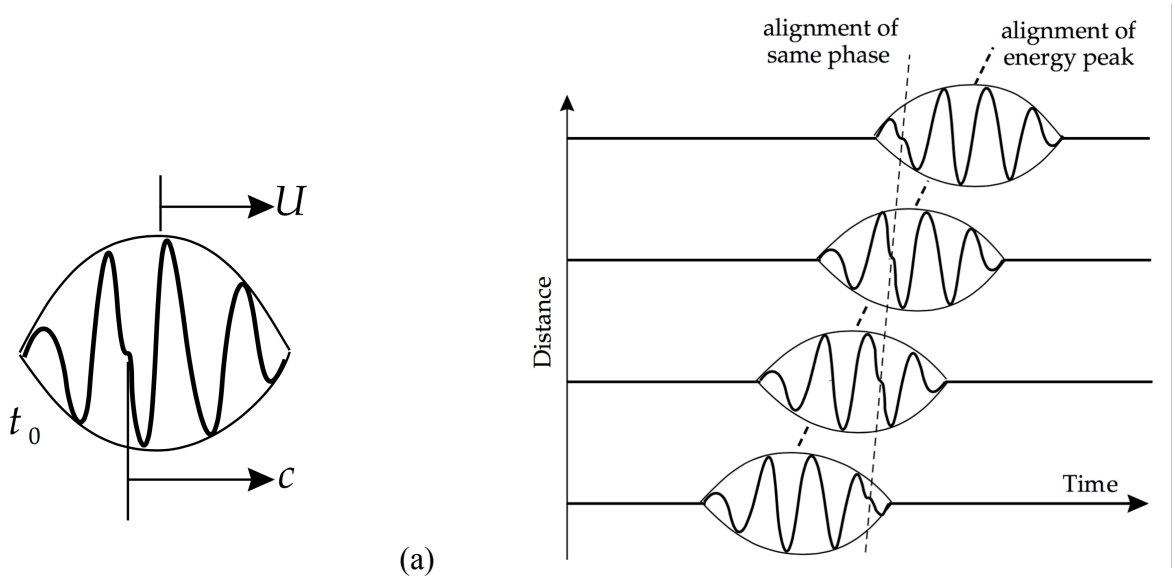

(a)

(b)

Figure 3.3: The comparison of the phase velocity and the group velocity. (a) The group velocity U and the phase velocity c. Note that the envelop of the wave packet travels with the group velocity, and the phase of any component of the wave propagates with the group velocity. (b) The arrivals of a dispersive wave at different receivers (Lowrie, 2007).

3.2 Ambient noise surface wave tomography

The estimation of the velocity structure for the crust and the upper mantle is the first and the most important step of studying earthquake source parameters. Traditional method is based on teleseismic waves, which are generated from earthquakes. However, most of large earthquakes occur at the plate boundary, and are far from seismic stations. Thus, it is usually difficult to obtain a satisfactory spatial sampling. In addition, the high frequency information of seismic waves might be lost due to the effect of attenuation and scattering (Shapiro *et al.*, 2005), which results in the limited resolution for the shallow crust.

Campillo and Paul (2003) introduced a new method, called the ambient noise tomography (ANT), which had become one of the most effective tools to image the Earth's structure. This method is based on the idea that ambient seismic noise contains a significant component of Rayleigh and Love wave energy, whose empirical Green functions between a pair of seismic stations can be extracted from cross-correlations of ambient noise data (Snieder, 2004; Ritzwoller *et al*., 2005). Since the Green functions describe the wave propagation between the station pair, both phase and group velocities can then be estimated by applying the multiple filter analysis (Herrmann, 1973; Snieder, 2004). Finally, the phase and group velocity dispersion curves for each station pair are inverted to tomographic dispersion maps.

3.2.1 Multiple filter technique

Multiple filter technique, developed by Dziewonski *et al.* (1969), is used to determine the group velocities of dispersive waves. This method is based on the fact that different frequencies of a surface wave have different arrival times. However, a surface wave spectrum might contain more than one mode, which might arrive at the same time with the same frequency. In order to solve this problem, Herrmann (1973) used the narrow band-pass filtering analysis to extract the spectral amplitudes and group velocities of each mode from surface wave signals.

We follow Herrmann's (1973) notes. Assume that a displacement caused by a surface wave at distance r and time t can be represented by:

$$f(t,r) = \frac{1}{2\pi}\int_{-\infty}^{\infty} A(\omega)e^{i(\omega t - kr + \phi)}dw, \tag{3.4}$$

where k is the wave number, ω is the angular frequency, $A(\omega)$ is the complex amplitude.

We simplify Dziewonski *et al.*'s (1969) filter function, and define the filter as

$$H(\omega) = e^{-\alpha(\omega-\omega_0)^2/\omega_0^2}. \tag{3.5}$$

This filter is a Guassian filter. Subscript 0 refers to the fundamental mode. α controls the width of the filter. Thus, the expression of the filtered function is given by

$$g(t) = \frac{1}{2\pi}\int_{-\infty}^{\infty} A(\omega)H(\omega)e^{i(\omega t - kr + \phi)}dw. \tag{3.6}$$

According to Bhattacharya (1983), we assume that $A(\omega)$, $\phi(\omega)$, and $k(\omega)$ can be approximated in the neighborhood of the filter center frequency ω_0 by the Taylor series expansion

$$k(\omega) = k_0 + \left(\frac{dk}{d\omega}\right)_{\omega=\omega_0}(\omega - \omega_0) + \frac{1}{2}\left(\frac{d^2k}{d\omega^2}\right)_{\omega=\omega_0}(\omega - \omega_0)^2, \tag{3.7}$$

$$\phi(\omega) = \phi_0 + \left(\frac{d\phi}{d\omega}\right)_{\omega=\omega_0}(\omega - \omega_0) + \frac{1}{2}\left(\frac{d^2\phi}{d\omega^2}\right)_{\omega=\omega_0}(\omega - \omega_0)^2, \tag{3.8}$$

and we also have

$$A(\omega) = A_0 e^{-\gamma(\omega-\Omega)^2/\omega_0^2} e^{+\gamma(\omega-\Omega)^2/\omega_0^2}. \tag{3.9}$$

The $A(\omega)$ peaks at $\omega = \Omega$, and γ determines the width of the signal spectrum. Based on the definition of group velocities, $1/U_0 = k_0' = (dk/d\omega)|\ \omega=\omega_0$.

Assume the filter $H(\omega)$ has cutoff frequencies at $\omega = \omega_0 \pm \omega_c$, we have

$$H(\omega \pm \omega_c) = e^{-\alpha\omega_c/\omega_0^2}. \tag{3.10}$$

We change the ω *to* $\omega_0 \pm \omega_c$. For the filter cutoff $\omega = \omega_0 \pm \omega_c$, we have

$$g(t) = \frac{1}{2\pi} A_0 e^{i(\omega_0 t - k_0 r + \phi_0)} \int_{-\omega_c}^{\omega_c} e^{-(ax^2+2bx+c)} dx, \tag{3.11}$$

where,

$$\begin{aligned} a &= \frac{\gamma}{\omega_0^2} + \frac{\alpha}{\omega_0^2} + \frac{i}{2}(k_0'' r - \phi_0') = \rho e^{i\psi} = a_R + i a_I, \\ b &= \frac{\gamma}{\omega_0^2}(\omega_0 - \Omega) - \frac{i}{2}\left(t - \frac{r}{U_0} + \phi_0'\right) = \sigma e^{i\chi} = b_R + i b_I, \\ c &= 0. \end{aligned} \tag{3.12}$$

From Abramowitz and Stegun (1965), we have the equation

$$\int e^{ax^2+2bx+c} dx = \frac{1}{2}\sqrt{\frac{\pi}{a}}\, e^{(b^2-ac)/a} \operatorname{erf}\left(\sqrt{a}x + \frac{b}{\sqrt{a}}\right), \tag{3.13}$$

and the relation

$$\operatorname{erf}(-z) = -\operatorname{erf}(z). \tag{3.14}$$

Thus, the new expression of g(t) is given by

$$\begin{aligned} g(t) = \frac{1}{2\pi} A_0 e^{i(\omega_0 t - k_0 r + \phi_0)} \cdot \sqrt{\frac{\pi}{a}}\, e^{-i\frac{1}{2}\psi} e^{i(2\chi - \psi)} \\ \cdot \left[\frac{1}{2}\operatorname{erf}\left(\sqrt{a}\omega_c + \frac{b}{\sqrt{a}}\right) + \frac{1}{2}\operatorname{erf}\left(\sqrt{a}\omega_c - \frac{b}{\sqrt{a}}\right)\right], \end{aligned} \tag{3.15}$$

and Eq. (3.15) can also be written as

$$\begin{aligned} g(t) = \frac{1}{2\pi} A_0 e^{i(\omega_0 t - k_0 r + \phi_0)} \cdot \sqrt{\frac{\pi}{a}}\, e^{-i\frac{1}{2}\psi} e^{\frac{a_R(b_R^2 - b_I^2) + 2a_I b_R b_I}{a_R^2 + a_I^2}} e^{i\frac{-a_I(b_R^2 - b_I^2) + 2a_R b_R b_I}{a_R^2 + a_I^2}} \\ \cdot \left[\frac{1}{2}\operatorname{erf}\left(\sqrt{a}\omega_c + \frac{b}{\sqrt{a}}\right) + \frac{1}{2}\operatorname{erf}\left(\sqrt{a}\omega_c - \frac{b}{\sqrt{a}}\right)\right]. \end{aligned} \tag{3.16}$$

Herrmann (1973) ignored the effect of the shape of the signal amplitude spectrum on the Gaussian filtered surface wave output. In order to obtain the bias free estimates of group velocities and spectral amplitudes, Bhattacharya (1983) provided two applications of multiple filter analysis. At this point, we follow Bhattacharya's (1983) presentation. The two *erf* terms

can be replaced by the single real term

$$\left[\text{erf}\,(\sqrt{\rho}cos\frac{1}{2}\psi)\right]. \tag{3.17}$$

Group velocities are estimated at the envelope maximum, which means that the spectral amplitudes reach the peak. Thus, we have

$$\delta\omega_{0i} = -\frac{b_I}{a_I} = -\frac{b_R}{a_R}, \tag{3.18}$$

and we also have the equation from Eq. (3.18)

$$t - \frac{r}{U_0} + \phi_0' \equiv -2b_I = -\frac{2a_I b_R}{a_R} = \frac{-2a_I\gamma(\omega_0 - \Omega)}{\gamma+\alpha}. \tag{3.19}$$

Consider the two values of the filter parameter α, we have

$$t_1 - \frac{r}{U_0} + \phi_0' = \frac{-2a_I\gamma(\omega_0 - \Omega)}{\gamma + \alpha_1} = 2a_I\delta\omega_1, \tag{3.20}$$

and

$$t_2 - \frac{r}{U_0} + \phi_0' = \frac{-2a_I\gamma(\omega_0 - \Omega)}{\gamma + \alpha_2} = 2a_I\delta\omega_2, \tag{3.21}$$

subtract Eq. (3.21) from Eq. (3.20)

$$t_1 - t_2 = -2a_I\gamma(\omega_0 - \Omega)\left(\frac{1}{\gamma+\alpha_1} - \frac{1}{\gamma+\alpha_2}\right), \tag{3.22}$$

and from Eq. (3.18)

$$\delta\omega_1 = \frac{\gamma(\omega_0 - \Omega)}{\gamma + \alpha_1}, \tag{3.23}$$

and

$$\delta\omega_2 = \frac{\gamma(\omega_0 - \Omega)}{\gamma + \alpha_2}. \tag{3.24}$$

Thus, we have

$$t_1 - t_2 = 2a_I(\delta\omega_1 - \delta\omega_2), \tag{3.25}$$

and

$$t_2 - \frac{r}{U_0} + \phi_0' = \frac{t_1 - t_2}{\delta\omega_1 - \delta\omega_2}\delta\omega_2. \tag{3.26}$$

Finally, we obtain the expression for group velocity

$$U_0 = \frac{r}{t_2 - \frac{\delta\omega_2(t_1 - t_2)}{\delta\omega_1 - \delta\omega_2} + \phi_0'}, \tag{3.27}$$

where ϕ_0' refers to the derivative of the source phase.

The multiple filter analysis can also be used to estimate phase velocities through the cross-correlation of recorded noise (Herrmann, 2013). We apply the filter $H(\omega - \omega_0)$ to the wave equation (Eq. 3.4) under the condition that $(\alpha/\omega_0^2)^2 \gg (r/2d^2k/d\omega_0^2)^2$, so the filtered signal is

$$g(t,r) = \frac{1}{2\pi}A(\omega_0)\omega_0\sqrt{\frac{\pi}{\alpha}}e^{i(\omega_0 t - k_0 r + \phi_0)}e^{-\frac{\omega_0^2}{4\alpha}\left(t-\frac{r}{U_0}\right)^2}. \tag{3.28}$$

The phase term is used to estimate the phase velocity if the source term is known. The phase at the group velocity arrival, e.g., $t = r/U_0$, is given by

$$\Phi = tan^{-1}\left[\frac{Im\ g\left(\frac{r}{U_0}, r\right)}{Re\ g\left(\frac{r}{U_0}, r\right)}\right] = \frac{r\omega_0}{U} - \frac{r\omega_0}{c} + \phi + N2\pi. \tag{3.29}$$

Thus, we have the expression for phase velocities

$$c = \frac{\omega_0 r}{-\Phi + \frac{\pi}{4} + \frac{\omega_0 r}{U_0} + N2\pi}. \tag{3.30}$$

The multiple filter technique is implemented by the computer program *do_mft* (Herrmann and Ammon, 2002), which estimates not only group velocity, but also phase velocity dispersion measurements from the possibilities. This program provides friendly graphic interfaces, which make easier to manually select the correct dispersion. Figure 3.4 shows the output of the

program.

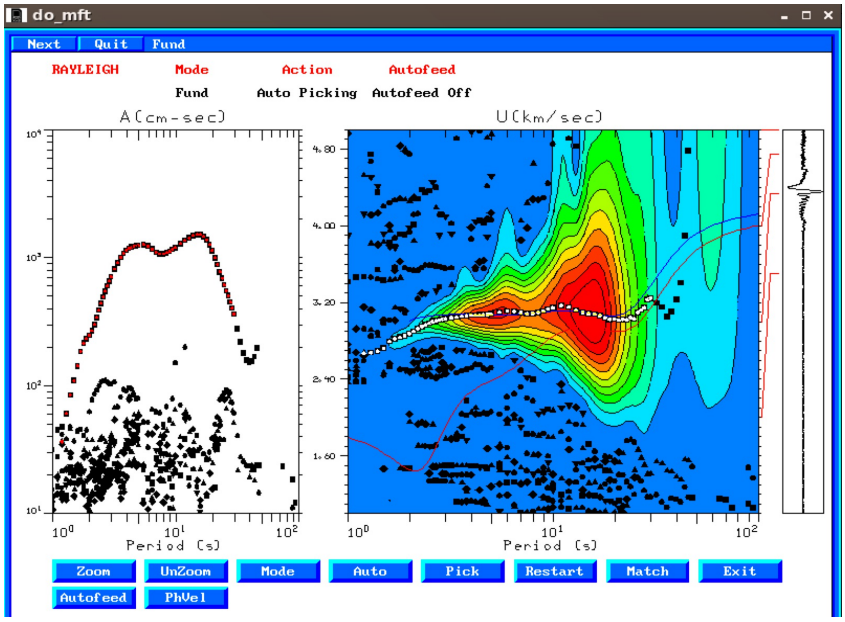

(a)

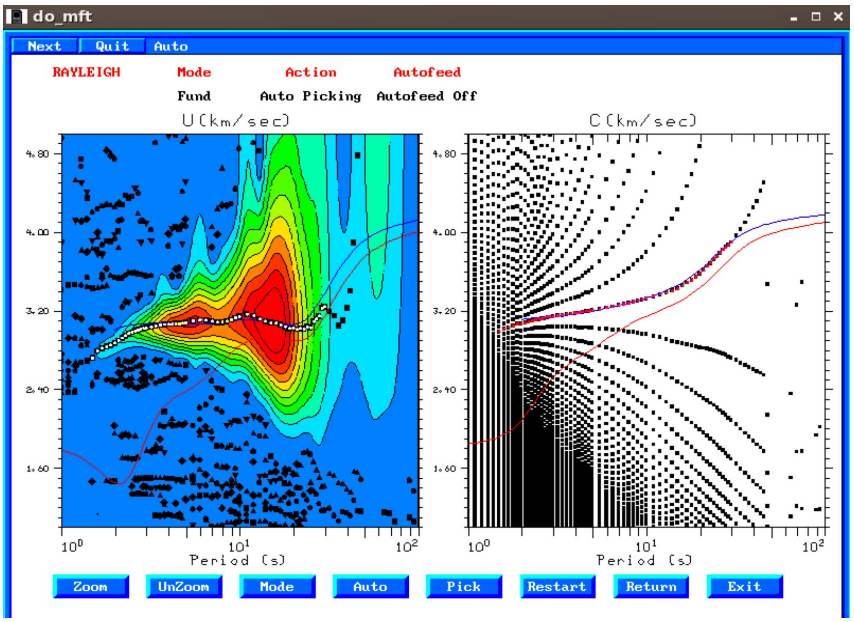

(b)

Figure 3.4: Graphic output of *do_mft*. (a) Left: spectral amplitudes. Right: estimated group velocity dispersion (write dots); (b) Left: estimated group velocity dispersion, same as the right figure in (a). Right: estimated phase velocity dispersion (red dots). Note that the blue and red curves are two reference curves, which are generated by the CUS and the WUS models (Herrmann, 1979; Herrmann *et al.*, 2011).

3.2.2 Least square tomographic inversion

Surface wave tomography has been used in studying of the crustal structure for over 30 years (e.g., Kafka and Reiter, 1987; Kocaoglu and Long, 1993). In this study, we use damped iterative least square algorithm (LSQR) to perform an approximate inversion for the Rayleigh/Love wave group/phase velocity tomography maps (Ammon, personal communication).

In order to obtain high-resolution maps, we set the inversion grid of the study area to uniform and small length cells (25 × 25 km). We also construct a starting model to provide the predicted data, which is the travel time of the surface wave along the ray path between each seismic station pair. The equation of the model is given by

$$\Delta t_{ij} = \sum_{n}^{N} X_{ij}^{n} \, p_n , \tag{3.31}$$

where subscript *i* - *j* refers to the station pair (i-j). *n* represents each cell on the grid. *N* is the total number of the cells. Δt is the travel time of surface wave. *X* is the fractional path length of each cell on the ray path. If the surface wave does not pass through a cell, the path length *X* for this cell will be zero. *p* refers to the slowness of a cell, which is defined as the reciprocal of the surface wave velocity $1/V_{Surf}$.

In the starting model, we assign a mean slowness *p* of the entire data set in the cells along the ray path. Since the ray path length *X* in each cell is known, the travel time Δt for each station pair can be determined from Eq. (3.31). We consider the travel time as the predicted data, thus

we have the equation for the inversion problem

$$d_{pre} = G\, m, \tag{3.32}$$

where d_{pre} refers to the predicted travel time of each station pair obtained from the start model. The data kernel, G, represents the length (X_{ij}^{n}) of ray path (i-j) in the *kth* cell. Similarly, if the cells that are not on the ray path, the length (X_{ij}^{n}) in kernel G will be zero. m is the model parameters that indicate the slowness p_k of the *kth* cell.

Thus, each term in Eq. (3.32) are given by

$$\begin{aligned} d_{pre} &= [\Delta t_{11},\ \Delta t_{12}, \cdots, \Delta t_{21}, \Delta t_{22},\ \cdots]', \\ \vec{m} &= [p_1, p_2,\ \cdots, p_{N-1}, p_N]', \\ G &= \begin{bmatrix} X_{11}^{1} & X_{11}^{2} & X_{11}^{3} & \cdots & X_{11}^{N} & X_{11}^{N} \\ X_{12}^{1} & X_{12}^{2} & X_{12}^{3} & \cdots & X_{11}^{N} & X_{12}^{N} \\ \vdots & \vdots & \vdots & \vdots & \vdots & \vdots \\ X_{21}^{1} & X_{21}^{2} & X_{21}^{3} & \cdots & X_{11}^{N} & X_{21}^{N} \\ X_{22}^{1} & X_{22}^{2} & X_{22}^{3} & \cdots & X_{11}^{N} & X_{22}^{N} \end{bmatrix}. \end{aligned} \tag{3.33}$$

The true phase and group velocities between each station pair (i-j) are obtained from the program *do_mft*. Thus, the true travel time for each station pair, or the observed data d_{obs}, can be determined by dividing the velocities from the distance between two stations, which is shown as

$$d_{obs} = [t_{11},\ t_{12}, \cdots, t_{ij},\ \cdots]', \tag{3.34}$$

$$t_{ij} = X_{ij}/v_{ij}, \tag{3.35}$$

where v_{ij} refers to the surface wave velocity.

In order to solve the model parameters in Eq. (3.32), we apply the least square method (Menke, 2012)

$$MIN = ||e||_2 = ||d_{obs} - d_{pre}|| = \left|\left|d_{obs} - G\,m\right|\right|. \tag{3.36}$$

For linear inverse problem, we have:

$$E = e^T e = (d_{obs} - Gm)^T (d_{obs} - Gm) = \sum_{i=1}^{N}\left[d_{obs_i} - \sum_{j=1}^{M} G_{ij} m_j\right]\left[d_{obs_i} - \sum_{k=1}^{M} G_{ik} m_k\right]$$

$$= \sum_{j=1}^{M}\sum_{k=1}^{M} m_j m_k \sum_{i=1}^{N} G_{ij} G_{ik} - 2\sum_{j=1}^{M} m_j \sum_{i=1}^{N} G_{ij} d_{obs_i} + \sum_{i=1}^{N} d_{obs_i}^2. \tag{3.37}$$

The derivative of the error E with respect to one of the model parameters m_q is given as:

$$\frac{\partial E}{\partial m_q} = \frac{\partial}{\partial m_q}\left[\sum_{j=1}^{M}\sum_{k=1}^{M} m_j m_k \sum_{i=1}^{N} G_{ij} G_{ik}\right] - 2\,\frac{\partial}{\partial m_q}\left[\sum_{j=1}^{M} m_j \sum_{i=1}^{N} G_{ij} d_{obs_i}\right] + \frac{\partial}{\partial m_q}\left[\sum_{i=1}^{N} d_{obs_i}^2\right]$$

$$= 2\sum_{k=1}^{M} m_k \sum_{i=1}^{N} G_{iq} G_{ik} - 2\sum_{i=1}^{N} G_{iq} d_{obs_i}\,. \tag{3.38}$$

Let $\partial E/\partial m_q$ equal to zero, we have:

$$\frac{\partial E}{\partial m_q} = 0 = 2\sum_{k=1}^{M} m_k \sum_{i=1}^{N} G_{iq} G_{ik} - 2\sum_{i=1}^{N} G_{iq} d_{obs_i}, \tag{3.39}$$

or,

$$G^T G m - G^T d = 0\,. \tag{3.40}$$

Thus, we obtain the estimated model parameters:

$$m_{est} = [G^T G]^{-1} G^T d\,. \tag{3.41}$$

In this study, we add *a priori* information to the inverse problem. Instead of minimizing the error E, we minimize the combination Φ of the prediction error E and the solution length L for the model parameter (Menke, 2012)

$$MIN = \Phi(m) = E + \varepsilon^2 L = e^T e + \varepsilon^2 m^T m\,, \tag{3.42}$$

where ε^2 is the weighting factor, which determines the relative importance given to the prediction error and solution length.

Similar to the standard least square method, we minimize Φ with respect to the model parameters m, and then obtain the estimated model parameters m_{est} from the damped least square solution:

$$m_{est} = [G^T G + \varepsilon^2 I]^{-1} G^T d \,. \tag{3.43}$$

The procedure for the inversion is iterative. When one inversion is finished, the resultant model parameters will be used to compute the new start model for the next inversion until all of the iteration cycles are finished.

In this study, we use the computer program, *multi_lsqr* (Ammon, personal communication) that incorporate smoothing in the spatial coordinates and also between periods to yield smoothed dispersion curves for each grid cell.

3.3 Receiver function

The study of the structure of the crust and upper mantle is a significant goal in geophysical research, in which the receiver function method is one of the most effective techniques in studying the discontinuities beneath seismic stations. This method is based on the idea that the recorded teleseismic body waveform, including direct P-wave and converted P-to-S wave (Ps), contains the information of the crustal structure near the receiver.

In 1979, Langston pointed out that the receiver function could be isolated from teleseismic

long-period body waves records by using the deconvolution of the radial component with the vertical components in frequency domain. Owens (1984) extended this method to higher frequency, and provided a way to study more detailed features of the crustal structure. However, the observations from large seismic events sometimes are very limited at some seismic stations, especially at temporary deployments. Although the number of small events are adequate to study the Earth's structure, the signal-to-noise ratio is too high to extract good receiver functions by using regular deconvolution techniques.

Ligorria and Ammon (1999) provided a new approach to solve the problem, which is based on Kikuchi and Kanamori's (1982) iterative deconvolution methods in time domain. This method is effective in estimating receiver functions not only from large events but also from noisy observations (Ligorria and Ammon, 1999).

When teleseismic P-waves are incident to the boundary between the crust and mantle, also known as Moho discontinuity, part of the P-waves will be converted to S-waves, which are usually slower than the direct P-waves (Figure 3.5 a). Since the incident angles of the incoming P-waves are very small, the influence of the crustal structure on the vertical components of the P-waves can be ignored (Ammon, 1991). However, the amplitude of the radial components of the converted S-waves is relatively large. In order to isolate the response of the crust and upper mantle, the observed vertical component that contains source and instrument effects is deconvoluted from the radial component of the seismogram (Langston, 1979). The resultant signal from the deconvolution is the receiver function, which consists the direct P-wave, the

direct P-to-S conversions (Ps), and several multiples (PsPhs, PsPhs, PpShs) (Figure 3.5 b).

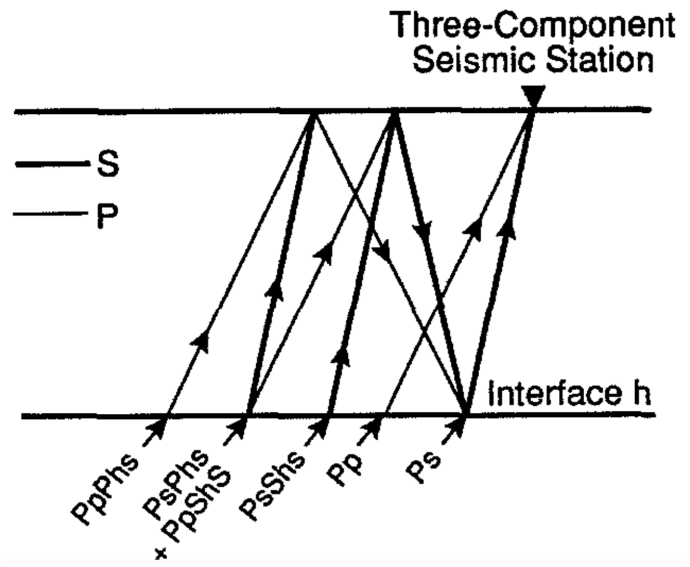

(a)

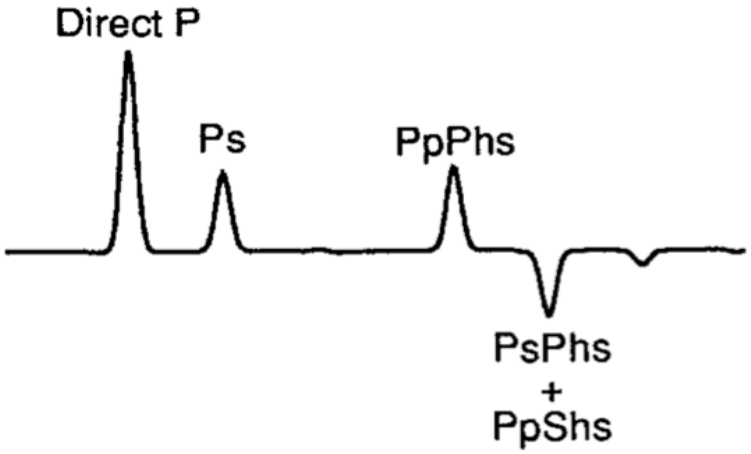

(b)

Figure 3.5: Receiver function ray diagrams. (a) Ray diagram including the major P-to-S converted phases. (b) The receiver function waveform. The phases in (b) are corresponding to the phases in (a). (Ammon, 1991)

The deconvolution procedure is simply shown as follows

$$D_i(t) = S(t) * G_i(t) * I_i(t), \tag{3.44}$$

where $D_i(t)$ represents the earthquake displacement response in time domain for a teleseismic P-wave, $S(t)$ is the source time function, $G_i(t)$ is the Green function of the impulse response of the path effects, and $I_i(t)$ is the instrument response. The subscript i refers to the three components, which are vertical (z), radial (r), and tangential (t) component, respectively.

The Green function $G_i(t)$ can be represented by the convolution of the three parts

$$G_i(t) = G_{S_i}(t) * G_{R_i}(t) * G_{M_i}(t), \tag{3.45}$$

where $G_{Si}(t)$ is the near-source response, $G_{Ri}(t)$ is the near-station response, and $G_{Mi}(t)$ is the other response (e.g., the mantle structure response).

Thus, for the vertical and radial components, the displacement response $D_i(t)$ is illustrated by

$$Vertical:\ D_z(t) = S(t) * G_{S_z}(t) * G_{R_z}(t) * G_{M_z}(t) * I_z(t). \tag{3.46}$$

$$Radial:\ D_r(t) = S(t) * G_{S_r}(t) * G_{R_r}(t) * G_{M_r}(t) * I_r(t). \tag{3.47}$$

For teleseismic P-waves, the steep incident angle results in the small crustal structure effects on the vertical component of P-waves. Thus, we approximate the near-station response $G_{Ri}(t)$ by letting

$$G_{R_z}(t) \approx \delta(t), \tag{3.48}$$

from which we obtain the revised Eq. (3.46)

$$D_z(t) = S(t) * G_{S_z}(t) * \delta(t) * G_{M_z}(t) * I_z(t). \tag{3.49}$$

We transfer the Eq. (3.46) and Eq. (3.47) to frequency domain

$$Vertical:\ D_z(\omega) = S(\omega)G_{S_z}(\omega)G_{M_z}(\omega)I_z(\omega), \tag{3.50}$$

$$Radial:\ D_r(\omega) = S(\omega)G_{S_r}(\omega)G_{R_r}(\omega)G_{M_r}(\omega)I_r(\omega), \tag{3.51}$$

Consider that the instrument responses of the both two components are same. The Eq. (3.50) and Eq. (3.51) can be simplified to:

$$Frequency\ domain:\ D_r(\omega) = G_{R_r}(\omega)D_z(\omega), \tag{3.52}$$

$$Time\ domain:\ D_r(t) = G_{R_r}(t) * D_z(t). \tag{3.53}$$

From the Eq. (3.53), we can use a simple deconvolution of $D_z(t)$ from $D_r(t)$ to extracts the near-station response $G_{Rr}(t)$ in redial component, which contains the information of the velocity structure beneath seismic stations (Langston, 1979).

Ammon (1991) extended Langston's (1979) receiver function technique in 1-D models, and obtained a new receiver function equation for the radial component:

$$G_R(t) = \frac{r_0}{z_0}[\delta(t) + \hat{r_l}\delta(t - t_l)], \tag{3.54}$$

where r_0 and z_0 refer to the amplitudes of the direct P arrival of radial and vertical components. $\hat{r_l}$ is the normalized amplitude of the *l*th ray. t_l is the arrival time of the *l*th ray.

Eq. 3.51 indicates the true amplitude of a receiver function, which provides a better constraint on the seismic velocity structure and discontinuities (e.g., Moho) than Langston's (1979) receiver function equation (Ammon, 1991).

However, most of the commonly used techniques require the observations with good signal-to-noise ratio, otherwise the resultant receiver functions will be noisy. Ligorria and Ammon (1999) introduced the iterative time-domain convolution approach into receiver function

studies to estimate good results from noisy observations. Firstly, they use the vertical component to cross-correlate with the radial component to obtain the lag of the first and largest spike, which is considered as the first estimated receiver function. Secondly, this receiver function is convolved with the vertical component of the observed seismogram. The new radial component seismogram can be obtained by subtracting the convolution from the previous radial component. Then they repeat these steps to estimate other spikes. One of the advantages of this approach is that the important features and other details in the original signal can be extracted one by one, and preserved as much as possible in resultant receiver functions (Ligorria and Ammon 1999). In this study, we follow this technique to perform the receiver function analysis.

3.4 Joint Inversion

We use joint inversion of receiver functions and surface wave dispersion measurements to construct 1-D S-wave velocity models for selected stations. Normally, receiver functions are sensitive to the velocity transitions at interfaces and vertical travel times. In contrast, surface wave dispersion provides better estimations of average velocities at different depth ranges (Julia *et al.*, 2000). The resultant velocity model from the joint inversion should be sensitive to both interface sharpness and velocity variations of the crust. Previous research had shown that this method provides tighter constraints to subsurface structure than either individual data set in some instance (e.g., Julià *et al.*, 2003; Shen *et al.*, 2012).

The joint inversion attempts to simultaneously invert receiver functions and surface wave

dispersion measurements for the S-wave velocity model. We follow Herrmann and Ammon's (2002) instructions to perform the joint inversion. The resultant velocity model should minimize the joint prediction error, which is shown as follows

$$E = \frac{(1-p)}{N_r}\sum_{i=0}^{N_r}\left(\frac{O_{r_i} - P_{r_i}}{\sigma_{r_i}}\right)^2 + \frac{p}{N_s}\sum_{j=0}^{N_s}\left(\frac{O_{s_j} - P_{s_j}}{\sigma_{r_j}}\right)^2, \tag{3.55}$$

where O refers to observed data, and P refers to predicted data. N represents the total number of the observations for each data set. σ is the standard error. Subscript r and s refer to the two data sets, receiver function and surface wave dispersion, respectively. Subscript i refers to the receiver function at time t_i, and j means the j^{th} surface wave dispersion. The factor p is an a priori parameter that controls the relative contribution of each data set to the solution. Thus, it is also called the influence factor. The value of p should be given by between 0 and 1. If $p = 0$, the receiver function will be the only data set to contribute to the solution. On the contrary, if $p = 1$, the surface wave dispersion is the only data set for the inversion. The computer program *joint96* implements the joint inversion method (Herrmann and Ammon, 2002). The 1-D S-wave velocity models are directly obtained from the program.

CHAPTER 4: RESULTS

In this chapter, we present the surface wave tomography maps of Rayleigh and Love waves at selected periods: 4s, 10s, 20s and 40s. The maps were obtained from the inversion program, *multi_lsqr* (Ammon, personal communication), which was also used to perform the checkerboard test for the tomography study. In addition, the results of geological information, receiver function and S-wave velocity model are presented in this chapter.

4.1 Checkerboard resolution test

The ambient noise tomography study for surface-wave dispersion uses BH channel waveforms of 133 TA stations across Oklahoma from 2009 to 2011. To reduce the computations, cross-correlations were made from 31 selected TA stations to each of the other stations. This selection ensures the reasonably uniform ray path coverage over the study area for tomography. Figure 4.1 shows the distribution of the TA stations. The blue circles indicate the master 31 stations. Figure 4.2 illustrates the ray path coverage used in tomographic inversion.

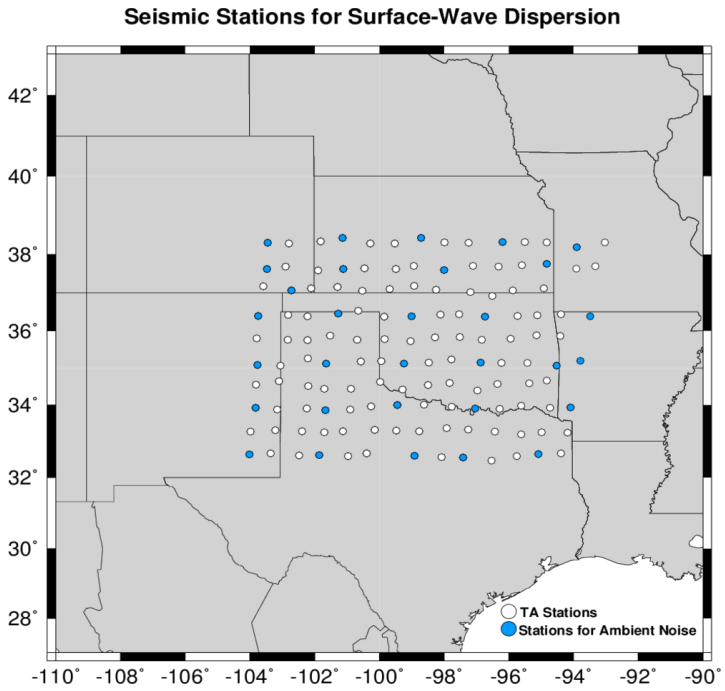

Figure 4.1: The distribution of TA stations. Blue circles refer to the master stations.

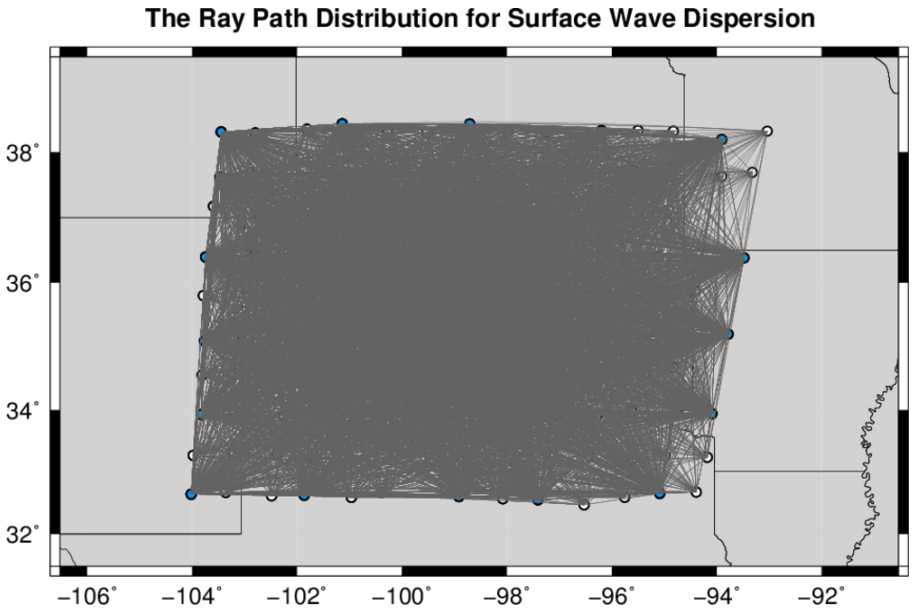

Figure 4.2: Ray path coverage.

To assess the resolution and the stability of the inversion, we performed a series of standard checkerboard tests for the Rayleigh/Love wave phase/group velocities. First, we create true

surface wave velocity models with ±5% velocity perturbation (between 2.85 and 3.15 km/s), which are distributed in the 2° × 2° grid checkerboard pattern. The synthetic travel time for each observed ray path was then computed through the true velocity model. Secondly, we applied the same inversion parameters as in the real data inversion, such as damping factors, to estimate the predicted velocity models at select periods.

Figure 4.3 – Figure 4.6 show the comparisons between the true and predicted models for the Rayleigh/Love wave phase/group velocities at periods of 4s, 10s, 20s, and 40s. The ability to recover the checkerboard patter mainly depends on the total number of the rays for each period. In addition, the grid cells located at the edge of the study region might show the poor fits due to limited rays across those cells.

The predicted Love and Rayleigh wave phase velocity models are well resolved between 4 s to 40 s, with an exception of the relatively poor fit at 4 s due to the smaller number of rays (Figures 4.3 and 4.4). The Love and Rayleigh wave group velocity models show some different patterns comparing with the phase velocity models. As shown in Figures 4.5 and 4.6, the inverted group velocity models are well recovered between 4 s and 20 s, but the resolution is limited at 40 s, especially for the Love wave group velocity (Figure 4.5 e). Although the predicted models do not perfectly recover the true models at some periods, we still believe that the resolution (2° × 2° grid) of the models are acceptable to perform the tomography study using real surface wave dispersion measurements at short periods.

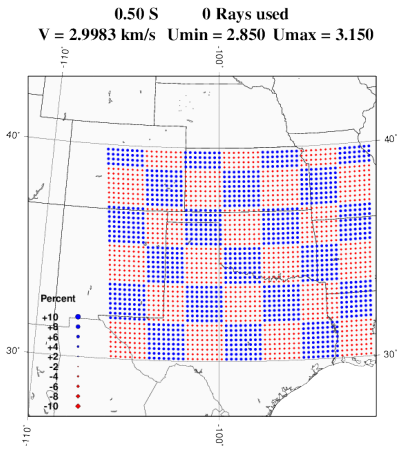

(a)

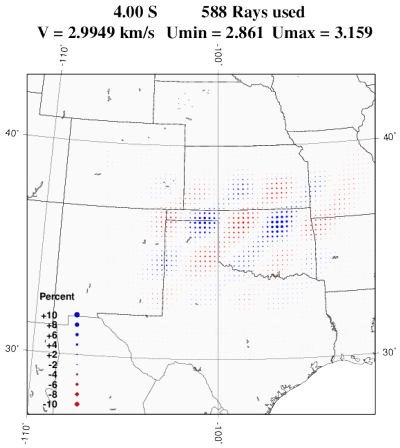

(b)

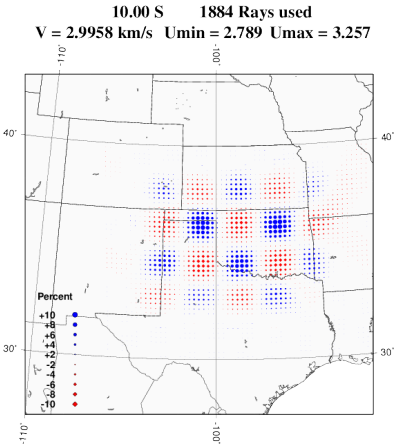

(c)

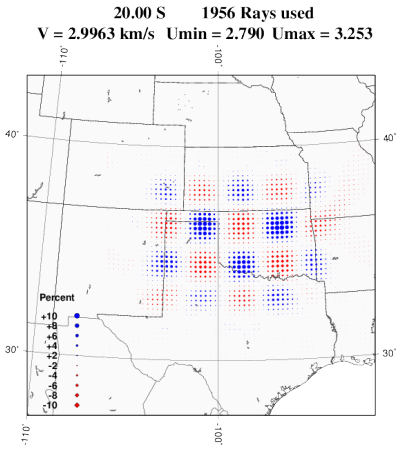

(d)

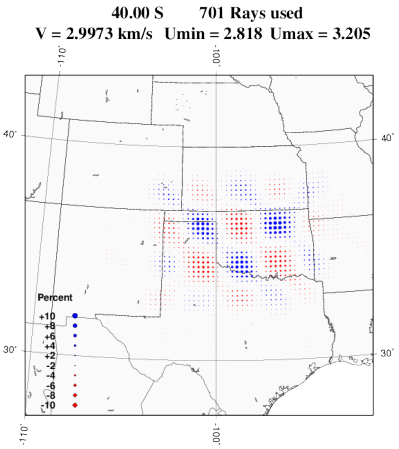

(e)

Figure 4.3: Checkerboard test for the Love wave phase velocity. (a) True velocity model. Tomographic inversions at 4 s (b), 10 s (c), 20 s (d), 40 s (e).

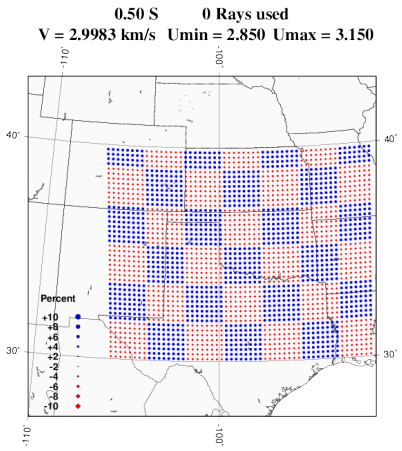

(a)

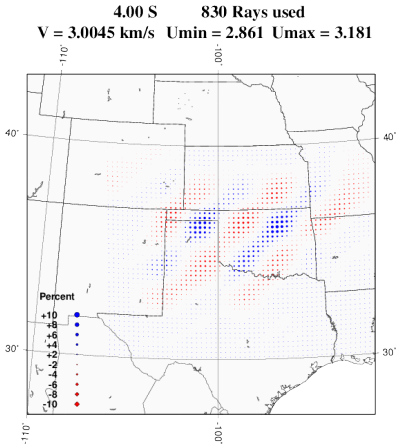

(b)

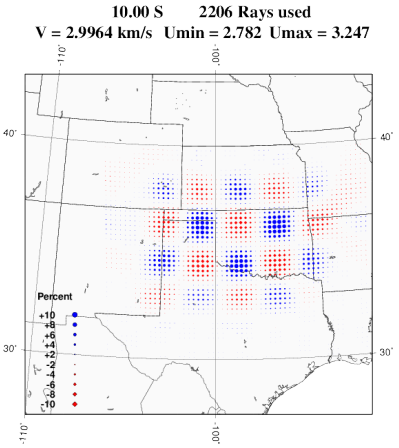

(c)

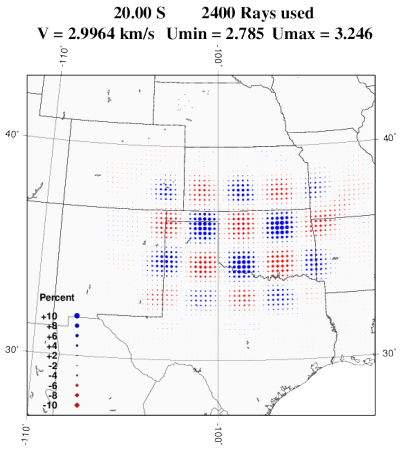

(d)

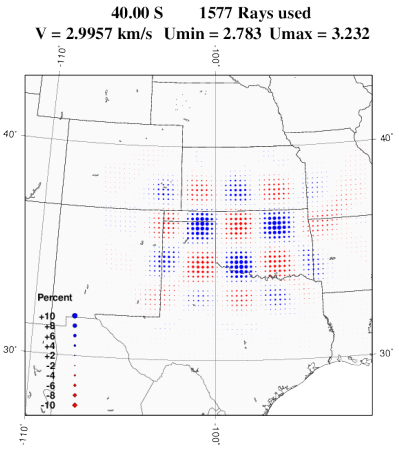

(e)

Figure 4.4: Similar to Figure 4.3, but for Rayleigh wave phase velocity.

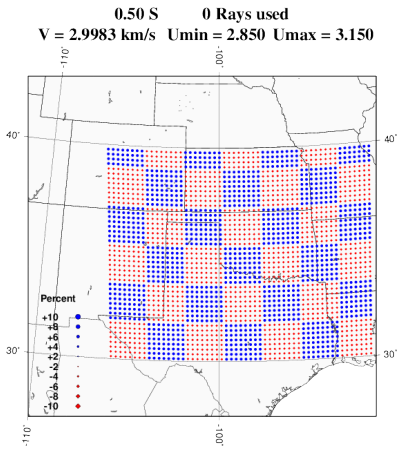

(a)

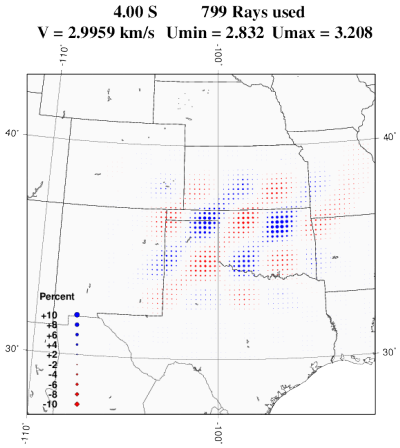

(b)

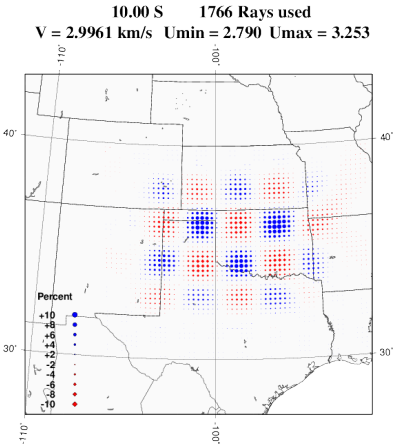

(c)

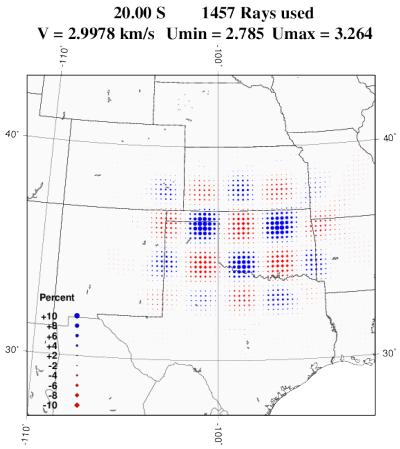

(d)

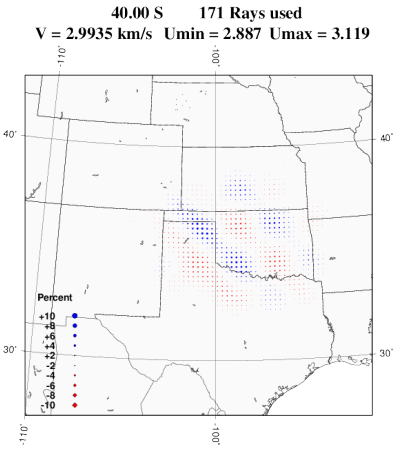

(e)

Figure 4.5: Similar to Figure 4.3, but for Love wave group velocity.

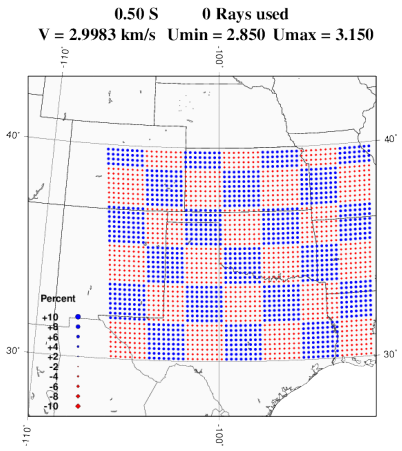

(a)

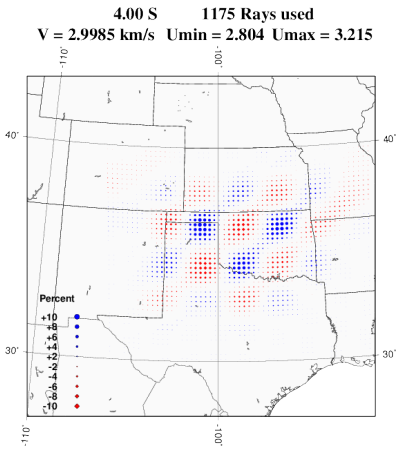

(b)

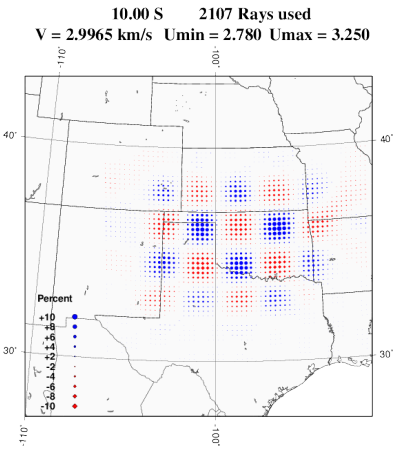

(c)

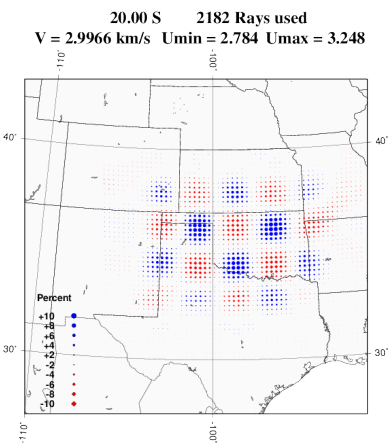

(b)

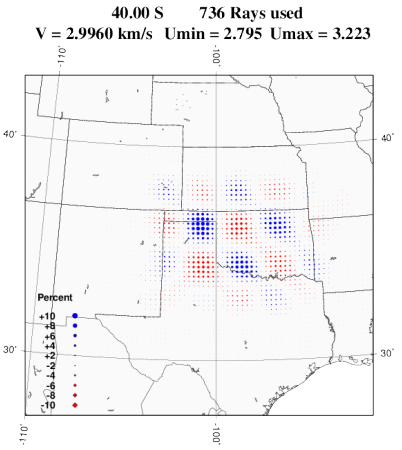

(c)

Figure 4.6: Similar to Figure 4.3, but for Rayleigh wave group velocity.

4.2 Surface wave tomography

We obtained the phase and group velocity tomography maps from 2 s to 60 s period for Rayleigh wave and 2 s to 50 s period for Love wave, which are parameterized on 25 × 25 km girds. Since some maps at very low periods (<3s) or very high periods (>45s) do not show the good results due to limited observations, only those maps constrained by more than 700 measurements (rays) are selected to present in this section. Examples of the resultant tomography maps are illustrated in Figure 4.7 – Figure 4.10, including the Rayleigh/Love wave phase/group velocity maps at 4 s, 10 s, 20 s and 40 s.

In these maps, red dots indicate the velocities lower than the average value, which illustrates sedimentary basins, except for the low velocity anomaly in southeast Oklahoma. Fast anomalies indicate mountains, which are shown by blue dots. The size of the dots is proportional to the percent of the velocity anomaly.

Figures 4.7 and 4.8 show the Rayleigh/Love wave phase/group velocity tomography maps at 4 s and 10 s, respectively. According to Cho *et al.*, (2007), surface wave tomography maps at certain period contain the geological structure information at the depth of about one-third of the wavelength. Thus, Figures 4.7 and 4.8 provide the average structure information of the upper crust over the depth of about 4 and 10 km, respectively. The transition between low and high velocity anomalies show the boundary of geological structures.

Most geological features are shown in both Figure 4.7 and Figure 4.8. The regions with low/high velocity anomalies in Figure 4.7 are correlated with the same regions in Figure 4.8.

However, some differences between the two figures are apparent. For example, Figure 4.7 shows much higher velocity anomaly in the northeastern Oklahoma, but a lower velocity anomaly in the southeastern Oklahoma than Figure 4.8. The group velocity tomography maps (Figure 4.7/4.8 b, d) present stronger velocity variations than the phase velocity tomography maps (Figure 4.7/4.8 a, c), especially at the period of 10 s. It is possible that group velocities are more sensitive to shallow structures than phase velocities.

Figure 4.9 presents the tomography maps at 20 s. Unlike 4 s and 10 s maps, the velocity variations are significantly reduced in 20 s maps, especially in the phase velocity maps (Figure 4.9 a, c). For example, the maximum velocity in Figure 4.7 (a) is about 18% faster than the average velocity, but this difference decreases to less than 4% in Figure 4.9 (a). In addition, it is difficult to identify geological structures in 20 s phase velocity maps due to the small velocity variations. However, they are shown in the group velocity maps (Figure 4.9 b, d), which is similar to the patterns in 4 s and 10 s maps. It is possible that the group velocity at 20s is more sensitive to the crust structure than the phase velocity. Figure 4.9 also illustrates the boundaries of major geological provinces.

The longest period maps shown in this section is the 40 s maps (Figure 4.10), which have the sensitivity to the uppermost mantle. Similar to the 20 s phase velocity maps, the velocity variation is too small to be used to identify the geological structures in Figure 4.10 (a, c) in which the maximum velocity is only 3% faster than the average velocity. Although the velocity anomalies are clearly shown in the group velocity maps (Figure 4.10 b, d), they are quite

different compared to with the 4 s and 10 s maps. The difference between maximum velocity and average velocity is approximately 4% in Love wave group velocity map and 6.6% in the Rayleigh wave group velocity map.

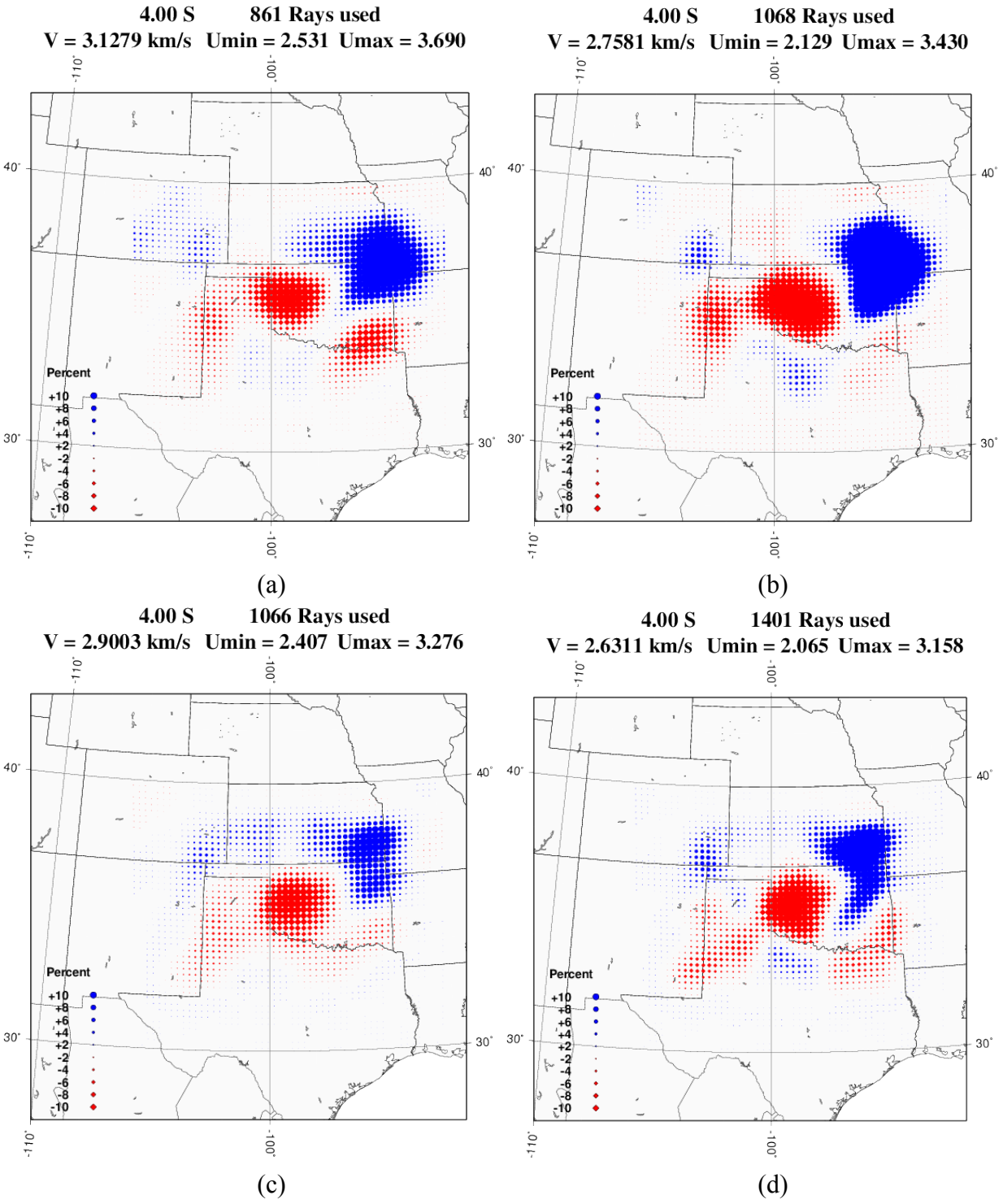

Figure 4.7: Love / Rayleigh wave phase / group velocity tomography maps at 4s period: (a) Love phase velocity, (b) Love group velocity, (c) Rayleigh phase velocity, (d) Rayleigh group velocity. Most of geological features in Figure 1.4 are illustrated in this figure. Notes that the red and blue dots indicate low and high velocity variation, respectively.

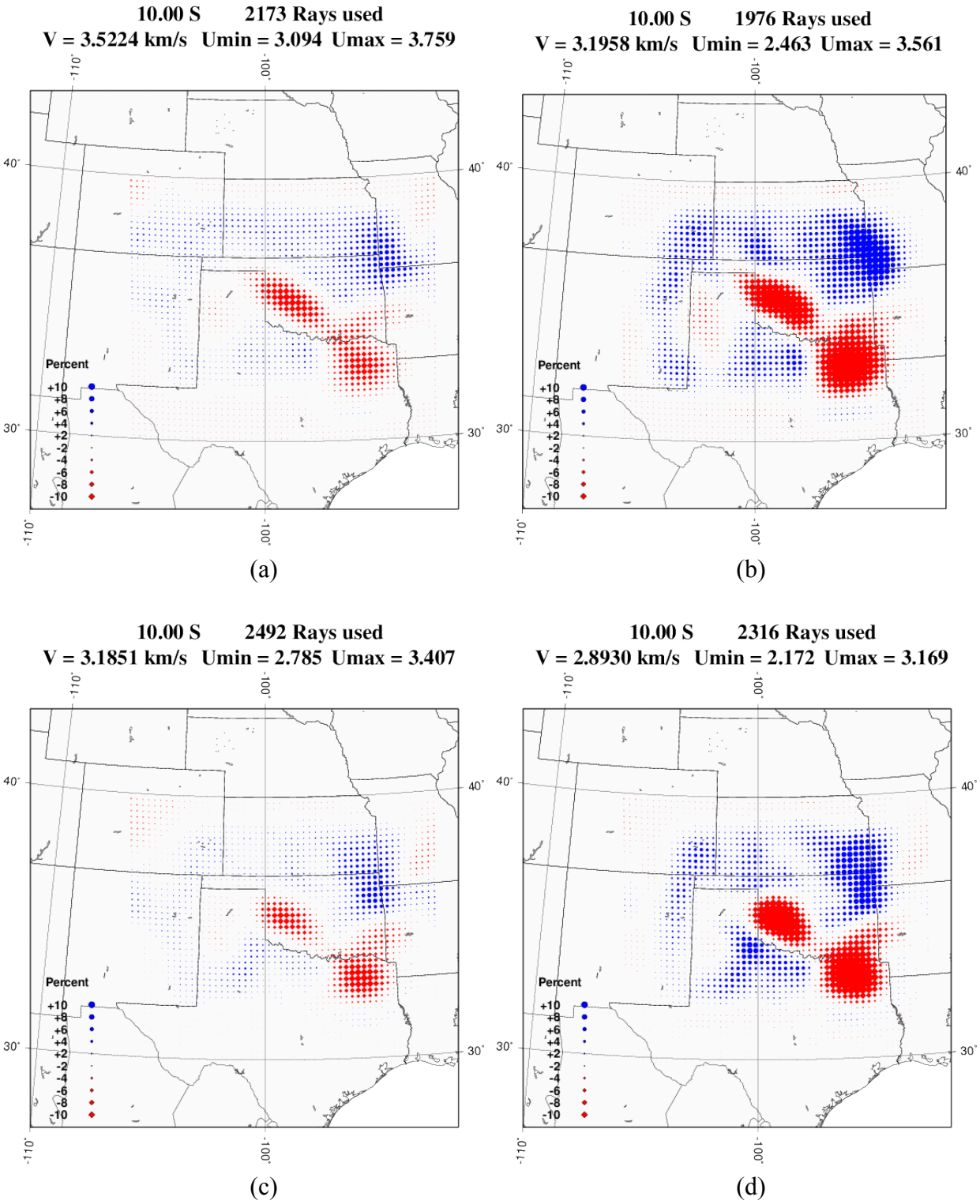

Figure 4.8: Similar to Figure 4.7, but at 10s period.

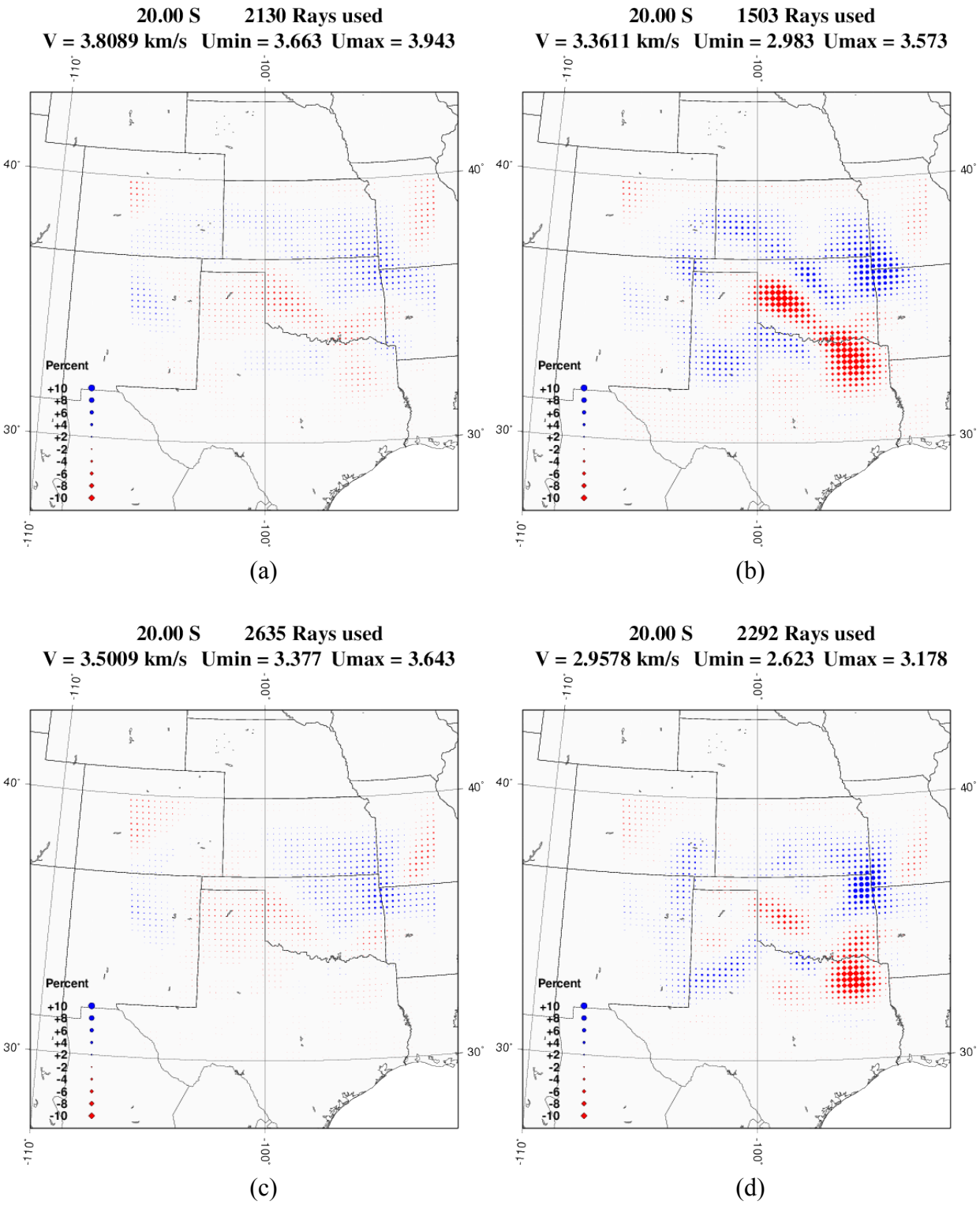

Figure 4.9: Similar to Figure 4.7, but at 20s period.

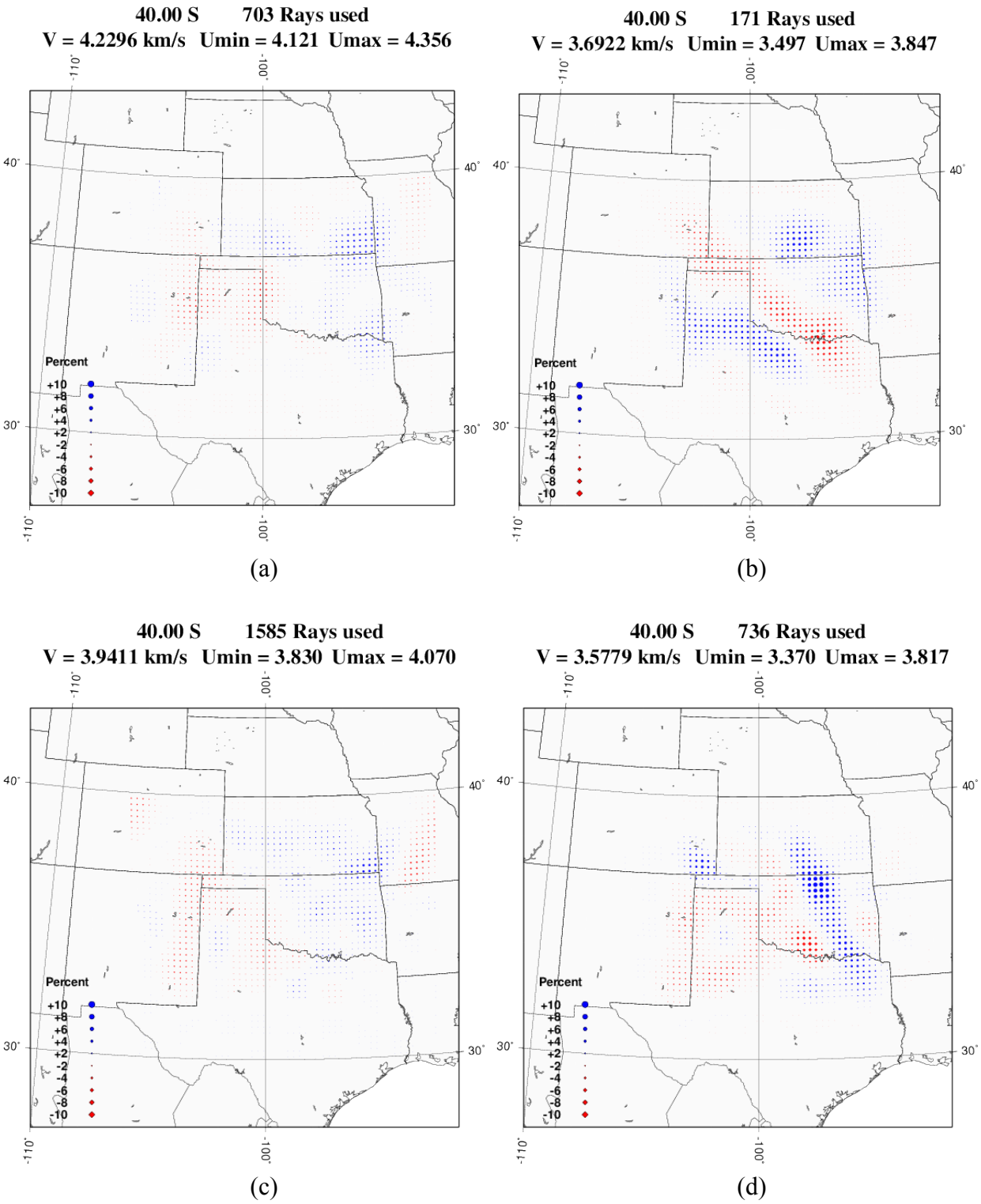

Figure 4.10: Similar to Figure 4.7, but at 40s period.

4.3 Geological information

Johnson *et al.*, (1988) provided detailed geological maps across the Southern Mid-Continent, which contain thickness and dominant lithologies of sedimentary rock of each period. In this study, we determined the depth to the basement of each OK and GS station by adding up the thickness of each sedimentary layer based on the maps. Detailed geological information for each station is shown in Table 1.

According to the depth of the basement, a relatively big weight was set at the interface between the sedimentary layer and basement in the joint inversion program. It is obvious that the information of depth constrains the velocity models, which might provide more accurate velocity profiles for the upper crust.

Table 1: Thickness and dominant lithologies of sedimentary rocks of major geological provinces in the Oklahoma (Johnson *et al.*, 1988).

Station / Geological time	CROK		QUOK		OK022		FNO		X34A		OK029/OK027/ BCOK/OK028	
	Lithology	Thickness (m)	Lithology	Thickness (m)	Lithology	Thickness (m)	Lithology	Thickness (m)	Lithology	Thickness (m)	Lithology	Thickness (m)
Upper Permian									Sandstone	150		0
Lower Permain	Shale	700					Sandstone	550	Sandstone	650	Sandstone	700
Upper Pennsylvanian	Shale	800	Shale	650	Shale	550	Sandstone	1050	Sandstone	900	Shale	950
Middle Pennsylvanian	Shale	200	Shale	300	Shale	600	Shale	300	Shale	1200	Shale	250
Lower Pennsylvanian									Shale	1650		0
Upper Mississippian	Limestone	75			Limestone	100			Limestone	150		0
Lower Mississippian	Limestone	100										0
Upper Devonian & Lowest Mississippian									Shale	180	Shale	≈0
Lower Devonian									Limestone	20	Limestone	≈0
Upper Ordovician & Silurian							Limestone	60	Limestone	270	Dolomite	≈40
Middle Ordovician	Carbonates	150	Carbonates	100	Carbonates	200	Carbonates	350	Carbonates	800	Carbonates	250
Upper Cambrian & Lower Ordovician	Dolomite	500	Dolomite	300	Dolomite	400	Dolomite	750	Limestone	2200	Dolomite	650
	Depth = 2525		Depth = 1350		Depth = 1850		Depth = 3060		Depth = 8170		Depth = 2840	

4.4 Receiver function

The teleseismic data for receiver function analysis is obtained from 3 U.S. Geological Survey (GS) stations and 6 Oklahoma Seismic (OK) stations from 2011 to 2014, which are shown as the red triangles in Figure 4.11. We selected these stations since all but one are in the areas of recent high seismicity.

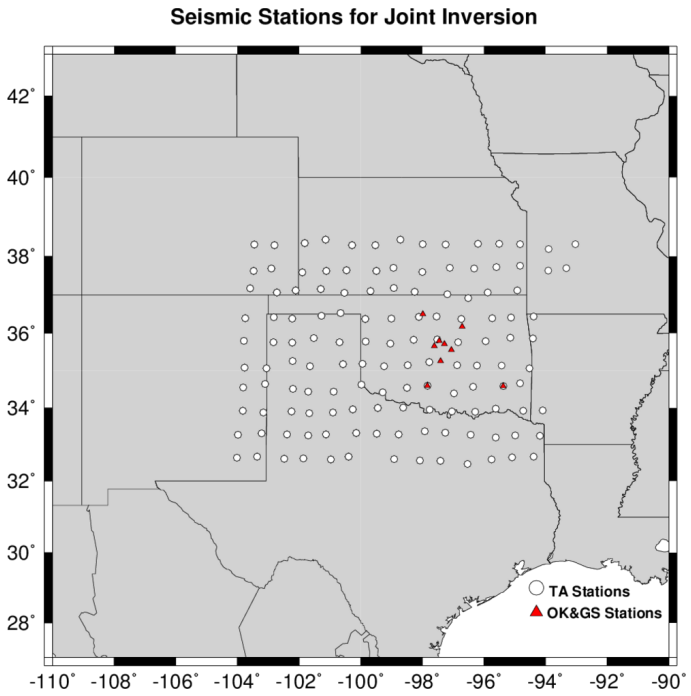

Figure 4.11: The distribution of seismic stations (red triangles) for the receiver function study.

Normally, receiver functions provide the information of shallow low velocity sediments, and are also sensitive to the Moho gradient. In this study, we computed the receiver functions from teleseismic data for three Gaussian filter parameters: α=0.5, α=1.0 and α=2.5 at 9 stations. Figure 4.12 shows an example of the receiver functions between 0 s and 40 s.

It is apparent that the peak of Ps is not strong, and the width of Ps is relatively wide for each receiver function trace. The last two arrivals, PpPhs and PsPhs + PpShs are difficult to be identified in this figure. These features suggest that the Moho might not be sharp. In addition, a strong trough can be observed in the 12–13 s time window (close to the peak of direct P wave) in each trace for two parameters, α=1.0 and α=2.5 (Figure 4.12 b, c). The strong troughs not only are due to the shallow low velocity sediments, but also imply relatively thick sedimentary layers.

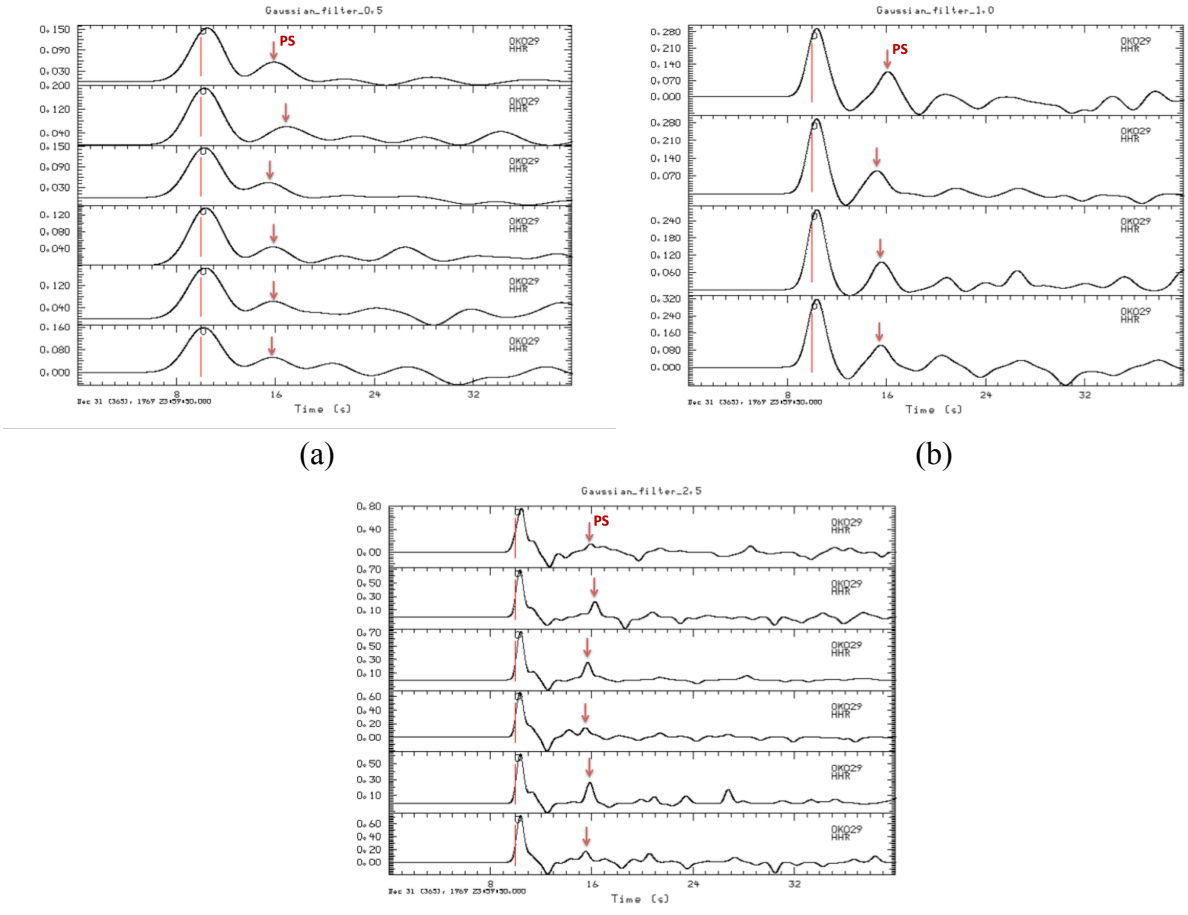

Figure 4.12: Examples of receiver functions at station OK029 for three Gaussian filter parameters: (a) α=0.5, (b) α=1.0 and (c) α=2.5. The arrows in each figure point out the P to S conversions (Ps).

4.5 S-wave velocity model

The 1-D S-wave velocity models (Figure 4.13 a-i) that we present in this study were determined by the joint inversion at 9 stations, which are mostly located at the central Oklahoma. Except for the station X37A, the most striking features of the models are the low S-wave velocities in uppermost crust (<8km), which suggest the existence of sedimentary layers above the basement. By applying the geological information, the inversion forced a sharp discontinuity at the contact between the Paleozoic and the basement. As shown in Figure 4.13 (a-g), this feature is illustrated as a "jump" of the velocity at the depth of about 3 km in each model. At depth near the Moho (about 40 km), all of the models show that the S-wave velocity gradually increases instead of abruptly changing with the depth, because the receiver function data do not require the Moho to be sharp.

At station X37A, previous geological studies did not provide enough information to constrain the depth of sedimentary layer due to the existence of folds. Thus the velocity model for X37A (Figure 4.13 i) was determined without any geological constraint at shallow depths.

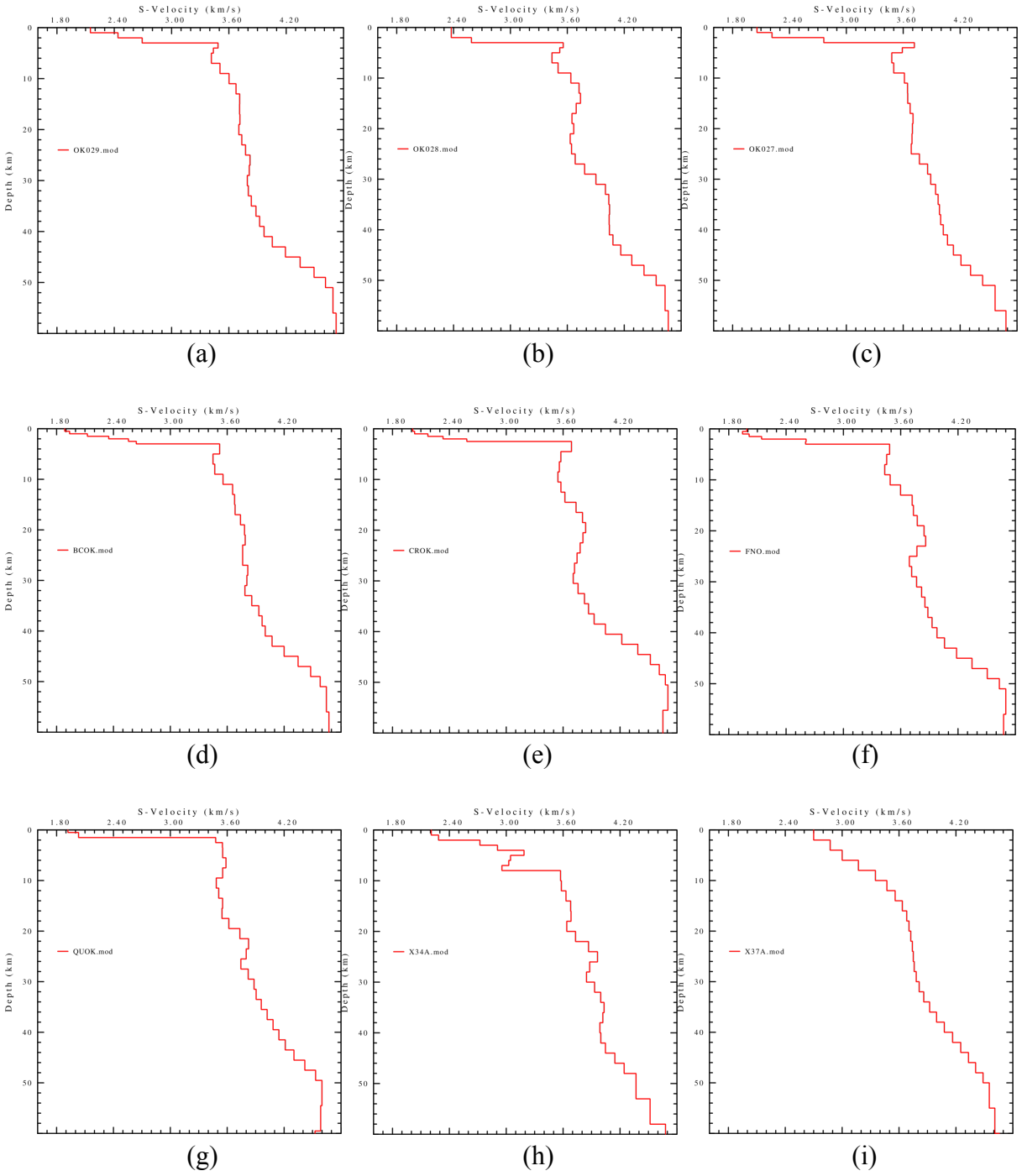

Figure 4.13: 1-D S-wave velocity models. Red solid lines show the model profiles as the function of depth from the surface to 60 km at selected stations: (a) OK029, (b) OK028, (c) OK027, (d) BCOK, (e) CROK, (f) FNO, (g) QUOK, (h) X34A and (i) X37A.

CHAPTER 5: DISCUSSION

In this Chapter, I provide the detailed interpretation and discussion of the results in given Chapter 4, including the tomography results and 1-D S-wave velocity models. I also compare the estimated surface wave dispersion with the dispersion from other studies at selected stations. The last section of this chapter is mainly about the tests of the velocity models. Specifically, I present the fit of the observed and the predicted data, including receiver function and surface wave dispersion, which are computed from the velocity models. In addition, a series of forward tests are also performed to test the velocity models.

5.1 Surface wave dispersion

5.1.1 Tomography results

Overall, the velocity variations in tomography maps are strong and localized at short periods ($\leq$ 20 s), but weak and varied at long period (40s). In the shallow crust, low velocity anomalies correspond to sedimentary basins; and high velocity anomalies are coincident with igneous mountains. Figure 5.1 illustrates the major geological structures. In the deep crust and the uppermost mantle, however, the velocity variations are affected more by the thickness than the composition of the crust. It is also the reason why the tomography maps show different patterns of velocity variations at the short and long periods.

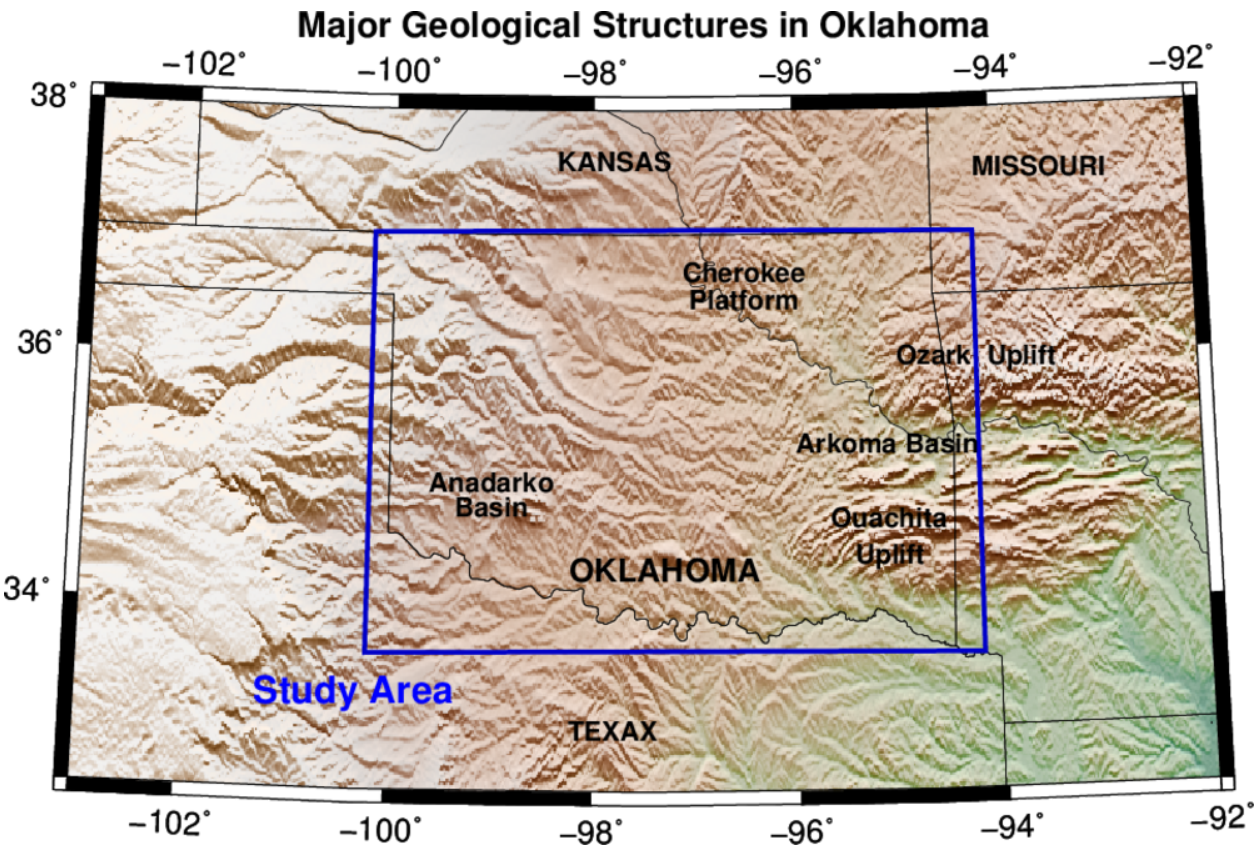

Figure 5.1: Major geological structures in Oklahoma.

Below 10 s (Figures 4.7 and 4.8), the tomography maps reflect strong velocity variations. At 4 s (Figure 4.7), the high velocity anomalies are associated with crystalline rocks in the Ozark Uplift, which covers northeastern Oklahoma, and extends northward into southwestern Missouri and southeastern Kansas. The low velocity anomalies are coincident with deep sediments in the Anadarko basin of western Oklahoma and the Arkoma basin of eastern Oklahoma. Most of the velocity anomaly features in 10 s maps (Figure 4.8) are similar to the features in 4 s maps, with a few exceptions. For instance, the 10 s maps show strong low velocity anomalies in the Ouachita Uplift, whereas this feature is not apparent in the 4 s maps.

Normally, uplifts correspond to high velocity anomalies in tomography maps, such as the Ozark uplift in Figure 4.8. However, the Ouachita Uplift is illustrated by the low velocity features in southeastern Oklahoma in 10 s maps. Previous geological studies suggest that the collision between the South American Plate and the North American Plate caused the Ouachita Orogeny, which buckled sedimentary strata, and produced Ouachita Uplift during the Pennsylvanian period (e.g., Viele and Thomas, 1989). In this region, the intense folds and faults are very common due to the orogeny, but volcanism and intrusions are absent. Therefore, the different patterns of the velocity anomalies between the Ouachita Uplift and the Ozark Uplift are probably resulted from the discrepancies in composition and structure of the two uplifts.

Many of the features in 4 s and 10 s maps are also seen in 20 s group velocity maps (Figure 4.9), such as the high velocity anomalies in the Ozark Uplift and the low velocity anomalies in the Anadarko basin. These features, however, are not apparent in 20 s phase velocity maps.

At long period (40 s, Figure 4.10), surface waves are sensitive to the structure to the depth of 50 km where the velocity variations are associated with the thickness instead of the composition of the crust. Normally, a low velocity anomaly indicates thick crust; and a high velocity anomaly corresponds to thin crust. As illustrated in the 40 s Rayleigh wave group velocity map (Figure 4.10, d), the strip-shaped high velocity anomalies are consistent with the Cherokee Platform and the west part of the Arkoma Basin. The low velocity anomalies in southwestern Oklahoma show the Wichita Uplift, which was developed during the Ouachita Orogeny. However, not all the low velocity anomalies are associated with the thick crust. One of the exceptions is that the Anadarko

Basin in western Oklahoma is illustrated by the low instead of the high velocity anomalies. According to Bensen et al. (2008), the shear wave velocity is not only sensitive to the structures but also to the very shallow structures, such as sedimentary basins at intermediate depth (40 km – 50 km).

Some earlier studies also provide the similar tomography results in Oklahoma (e.g., Bensen *et al.*, 2008; Liang and Langston, 2008; Ekstrom, 2014). For example, the tomography maps in this study have the similar patterns of velocity variations with Bensen *et al.*'s (2008) maps. However, our maps provide more detail than previous studies, such as the boundaries of the relatively small geological structures, because we expanded much effort to get surface wave dispersion of shorter periods. In addition, the tomography maps at very low periods (2 s – 4 s) are entirely new in Oklahoma.

5.1.2 Comparison to the other studies

We compare the tomographically estimated dispersion with the dispersion obtained from the other studies to test the tomography results, as shown in Figure 5.2. Different colors of the dots represent different data sets. The dark blue dots (OK) are from the dispersion of this study. The light blue dots (NELE) illustrate Su *et al.*'s (2015) results including the Rayleigh/Love wave phase/group velocities in the periods 2 – 60 s. Both the green (HRV) and yellow (EK13) dots are from Ekstom's dispersion results. The EK13 only contains phase velocities, and focuses more on relatively low periods (5 – 40 s) than HRV, which, however, contains both phase and group

velocities in the 35 – 150 period range (Ekstrom, 2011; Ekstrom 2014). The red dots (NA) are plotted for the group velocities in the periods 2 – 150 s, which is based on Herrmann *et al.*'s (2013) results for earthquake data. We also collected the Rayleigh wave phase velocities from Jin and Gaherty's (2015) study, which are shown by the white dots. The two reference curves shown in red and blue in Figure 5.2 are obtained from the WUS model and the CUS model (Herrmann, 1979; Herrmann *et al.*, 2011). Note that the surface wave velocities for the WUS model are lower than the velocities for the CUS model at the same periods. It is because the WUS model is designed for intermountain west where the large sedimentary basins are the dominant geological structures (Herrmann *et al.*, 2011).

Note that we treat all data sets for a given wave type and velocity type with equal weight in the inversion, but apply more weight to the phase velocity observations in the dispersion plots (Figure 5.2) since we forced them to have less measurement scatter than the group velocities.

Not all the data sets are presented in the same figures due to different path coverage and velocity types. In Figure 5.2, the Rayleigh/Love wave phase velocities for all the stations coincide well with the other data sets in the whole period range, except that the Love wave phase velocities at station X37A is slightly higher than the EK13's velocities at the periods less than 10 s (Figure 5.2, i). The Rayleigh/Love wave group velocities, however, not perfectly agree with the other data sets, especially with the NA's velocities at stations OK029, OK028, OK027 and X34A in the 10 – 15 s period range (Figure 5.2: a, b, c, h). For instance, our group velocities are lower than NA's velocities at the station X37A (Figure 5.2, i), but higher at the station OK029 (Figure

5.2: c, h). The difference between the group velocities derived using ambient noise tomography and earthquake data (refers to NA's results) are due to path coverage and error in earthquake source parameters. Figure 5.2 also reveals some problems in the tomography results. For example, at the periods shorter than 3 s, the group velocities unusually increase with the decrease of the periods, which is probably due to some bad observations at short periods.

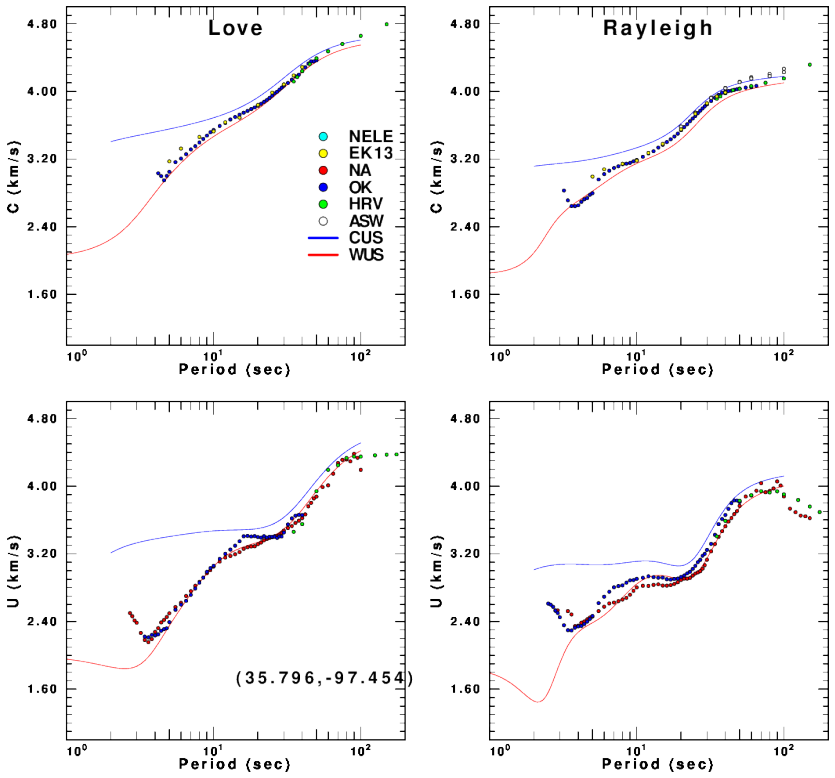

(a) OK029

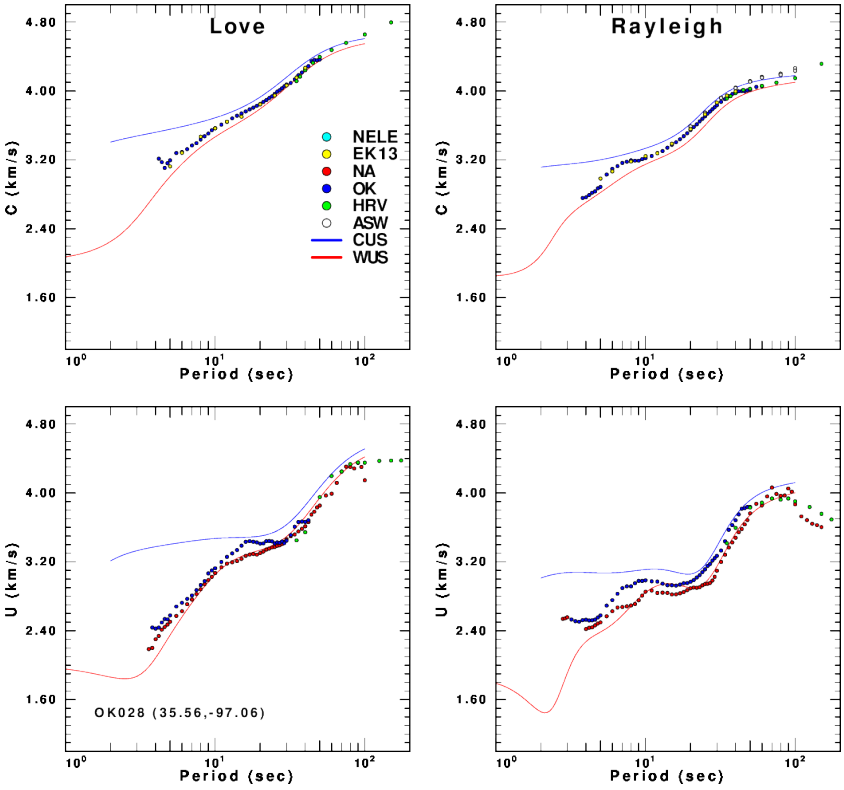

(b) OK028

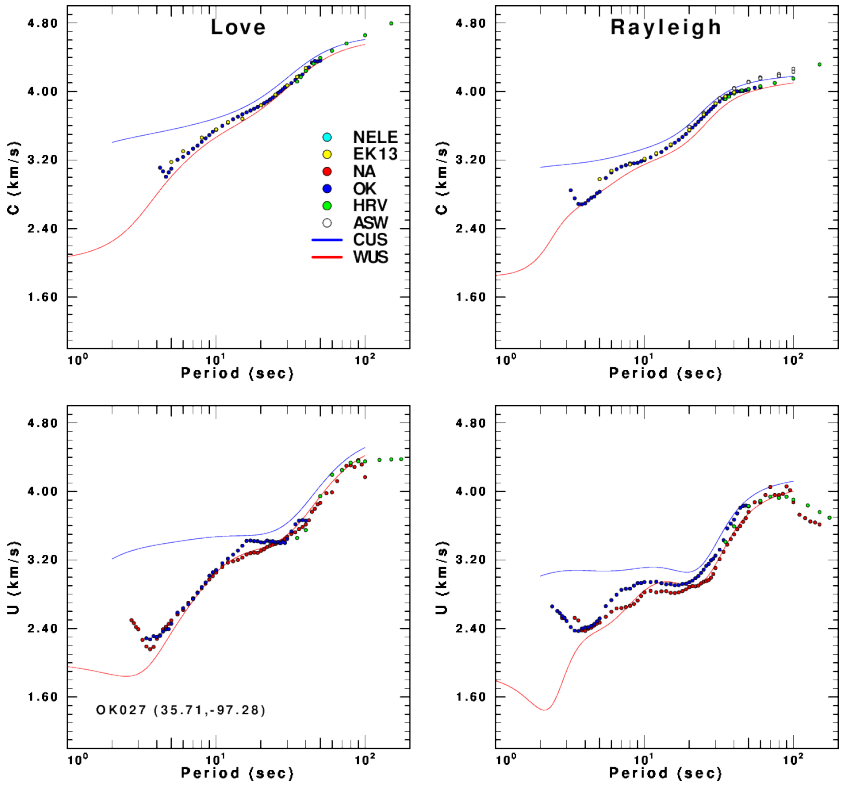

(c) OK027

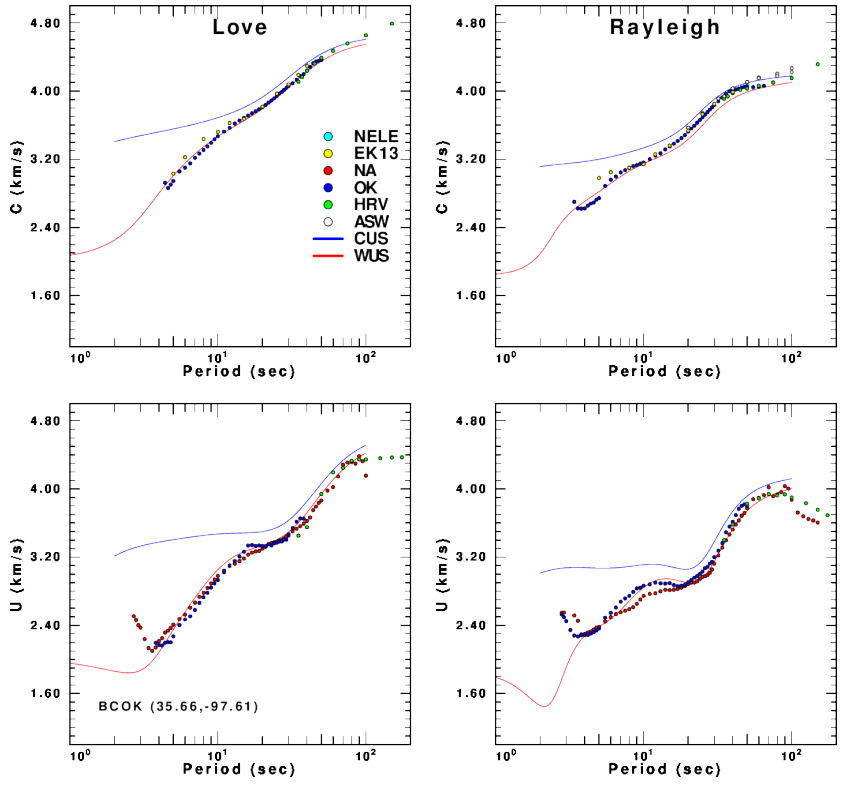

(d) BCOK

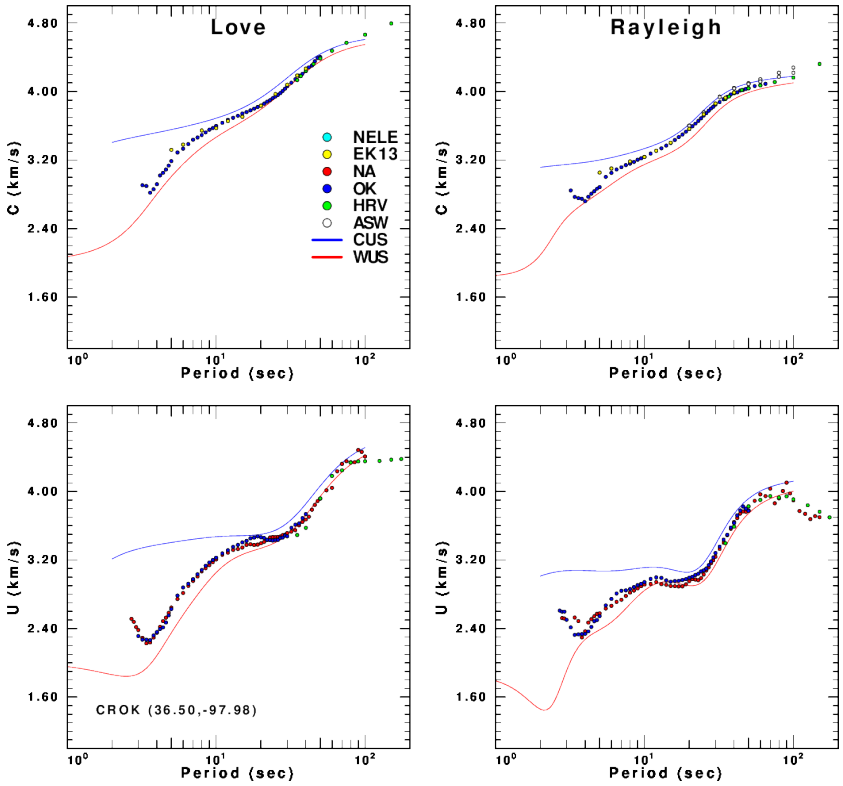
Love
Rayleigh
C (km/s)
U (km/s)
Period (sec)
NELE
EK13
NA
OK
HRV
ASW
CUS
WUS
CROK (36.50,-97.98)

(e) CROK

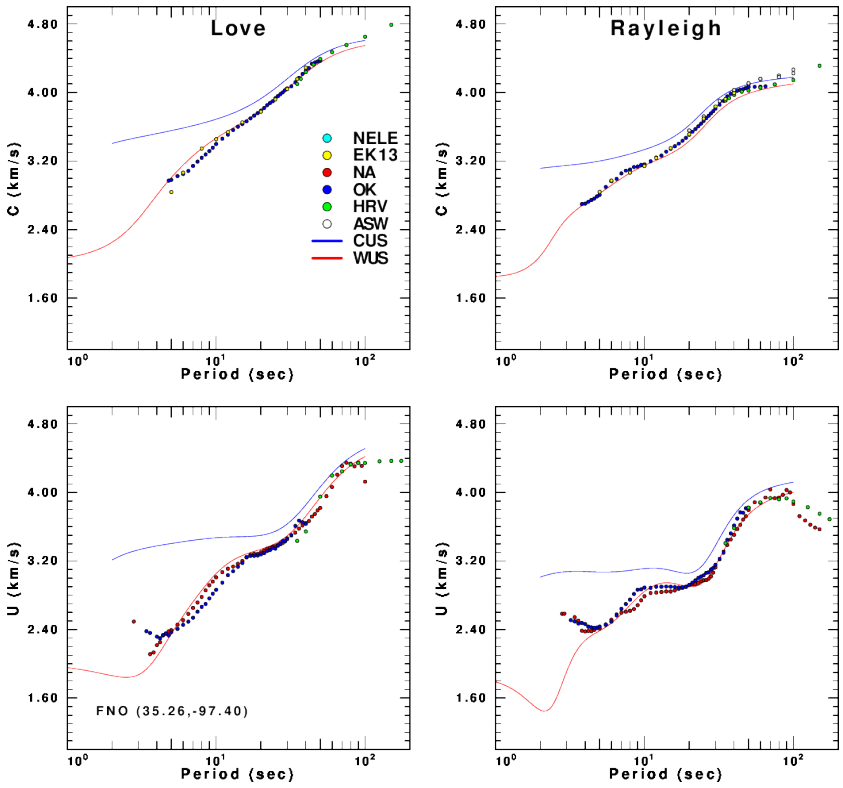
Love
Rayleigh
C (km/s)
U (km/s)
Period (sec)
NELE
EK13
NA
OK
HRV
ASW
CUS
WUS
FNO (35.26,-97.40)

(f) FNO

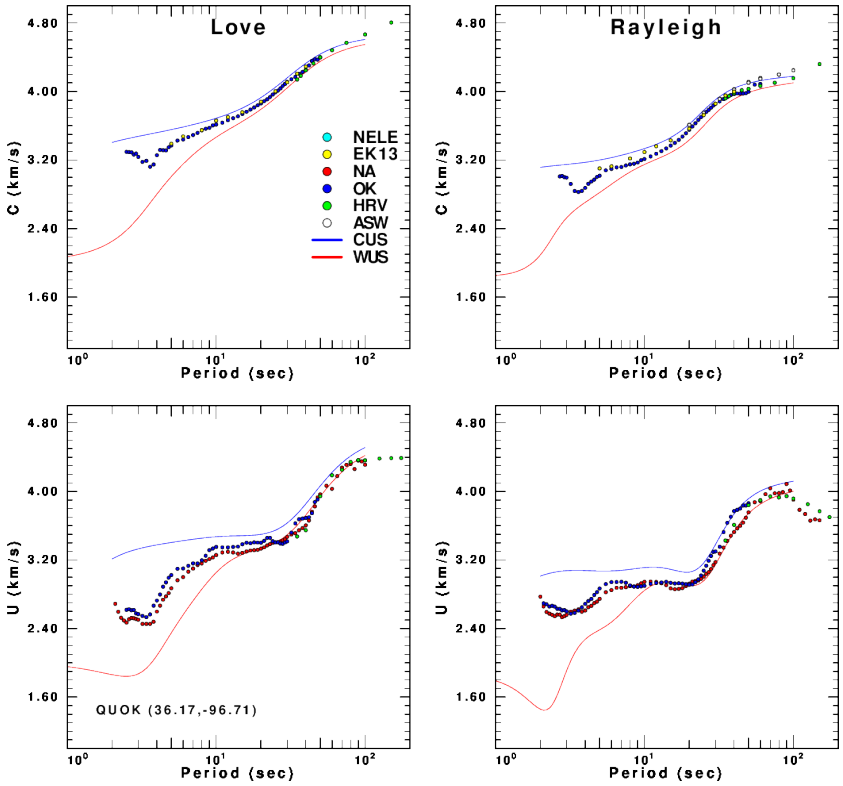
Love
Rayleigh
NELE
EK13
NA
OK
HRV
ASW
CUS
WUS
C (km/s)
U (km/s)
Period (sec)
QUOK (36.17,-96.71)

(g) QUOK

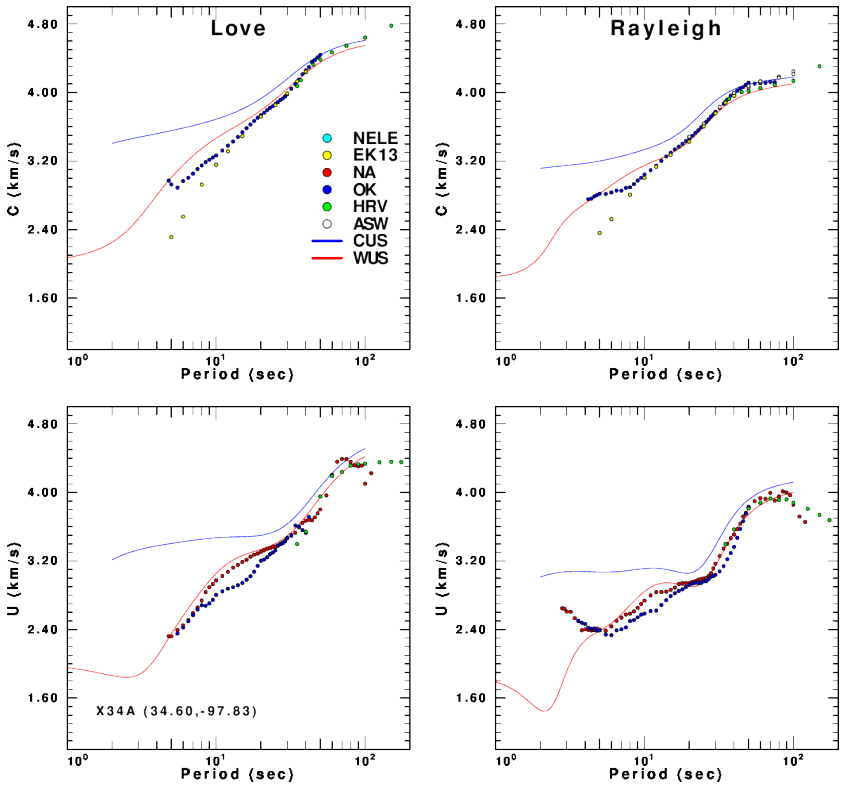
Love
Rayleigh
NELE
EK13
NA
OK
HRV
ASW
CUS
WUS
C (km/s)
U (km/s)
Period (sec)
X34A (34.60,-97.83)

(h) X34A

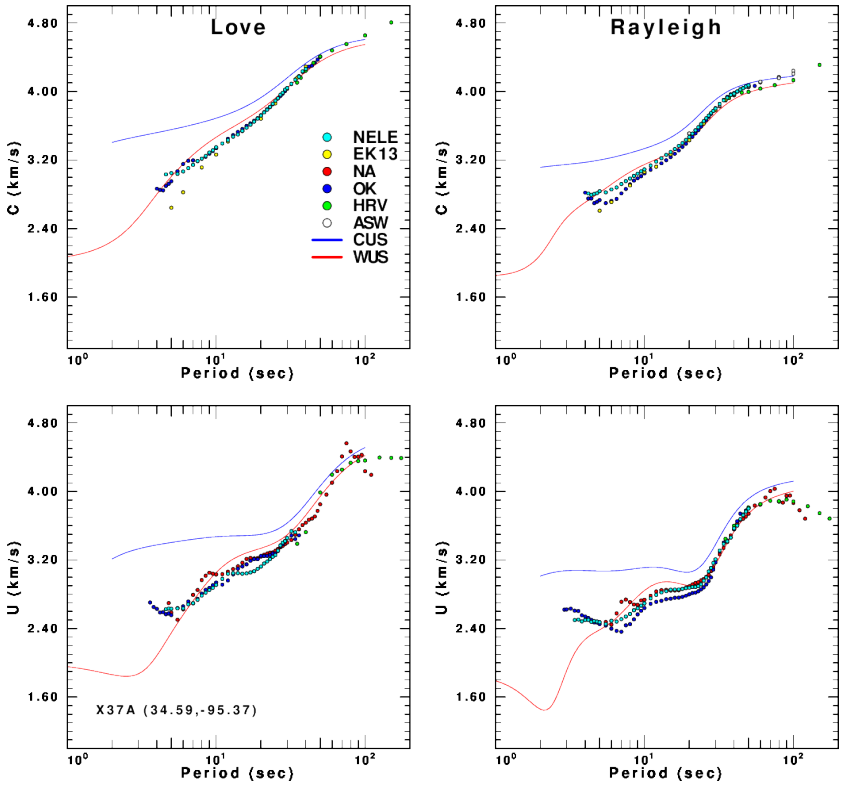

(i) X37A

Figure 5.2: The comparison of the tomographically estimated dispersion and the dispersion from other studies at selected stations, which are shown as follows: (a) OK029, (b) OK028, (c) OK027, (d) BCOK, (e) CROK, (f) FNO, (g) QUOK, (h) X34A, and (i) X37A. In each figure: Love wave phase velocity (upper left), Love wave group velocity (lower left), Rayleigh wave phase velocity (upper right), and Rayleigh wave group velocity (lower right). The colored dots represent the dispersion from different studies. Note that the blue dots (OK) are from the dispersion of this study. The blue curves are the CUS model predicted dispersion, and the red curves are the WUS model predicted dispersion.

5.2 S-wave velocity model

The 1-D S-wave velocity models were inverted from the surface wave dispersion and the receiver function at selected stations. Since only the shallow part of the velocity models are important to study the induced earthquakes in Oklahoma, I used the receiver function data between -5s and 15 s for the joint inversion to reduce the computations. Figure 4.13 shows the velocity models. It is apparent that they are similar to one another at the shallow depths and the Moho transitions, except for the models at station X34A and X37A. The low velocities in the uppermost crust (0 – 4 km) are associated with the thick sedimentary layers. At the depths between 40 km and 50 km, the gradually increased velocities suggest that the Moho is not sharp.

The X34A model is more complicated than the other models. Besides the low velocities at the shallow depths (0 – 4 km), it also contains another low velocity region in upper crust (6 – 8 km). Since the receiver functions are few and poor at this station, this problem might be solved as soon as more receiver functions are available. The X37A model is similar to the other models, except that it shows the relatively high velocities at shallow depths, because the geological information is not available at this station.

Previous studies have developed many S-wave velocity models for the continental North America. For example, Herrmann *et al.* (2011) presented two 1-D S-wave velocity models, which are the central United States model (CUS) and the western United States model (WUS), respectively. The CUS model is designed for the midcontinent region, whereas the WUS model is developed for the intermountain region (Herrmann *et al.* 2011). The WUS model had already

been used to study the earthquake relocations in central Oklahoma (McNamara *et al*., 2015). Although it acceptably estimates the S-wave velocities in upper 10 km crust for Oklahoma, the velocity models of this study might provide better velocity estimations in the same region, since we use geological information to constrain the velocity models.

5.3 Model testing

We test the 1-D S-wave velocity models by performing a series of forward simulations. On the one hand, we use the models to generate predicted surface wave dispersion curves and receiver functions for the 9 stations. The predicted results are then plotted with the observed data to test the consistency of each other. On the other hand, we compare the observed transverse waveforms for earthquakes with the predicted waveforms, which are obtained from the velocity models.

5.3.1 Fit to the surface wave dispersion

We use the joint inversion models to compute the predicted surface wave dispersion curves, which is given in red in Figure 5.3. The black circles and triangles show the observed dispersion estimations at each station from this study, which are obtained from the tomographic inversion. The phase and group velocities are plotted together. Since phase velocities are normally faster than group velocities at the same periods, so upper and lower curves in each figure represent phase and group velocities, respectively.

In Figure 5.3, the predicted Love/Rayleigh wave phase velocity dispersion curves accurately fit the observed dispersions at all stations throughout the whole period range except at the very short periods (< 3 s). Similarly, the predicted Love wave group velocity curves are also fit well with the observed dispersions, with a few exceptions. For example, the predicted curves are slightly lower, but smoother than the observed velocities in the periods 15 – 20 s at the stations OK029, OK028 and OK027 (Figure 5.3: a, b, c).

The predicted and the observed Rayleigh wave group velocities are fit acceptably at these stations except in the periods 10 – 20 s where the predicted velocities are higher than the observed velocities at the stations OK029, CROK, FNO, and QUOK (Figure 5.3: a, e, f, g). Moreover, they also show misfit in the 2 to 3 s period range at all stations, which is probably due to the bad observations at short periods.

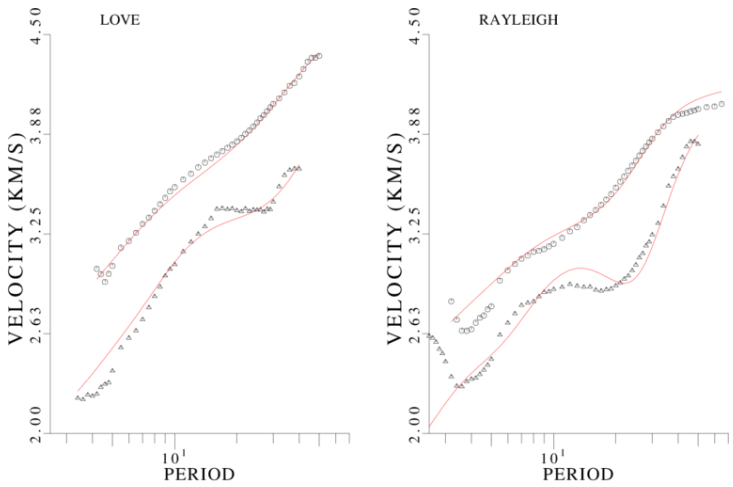

(a) OK029

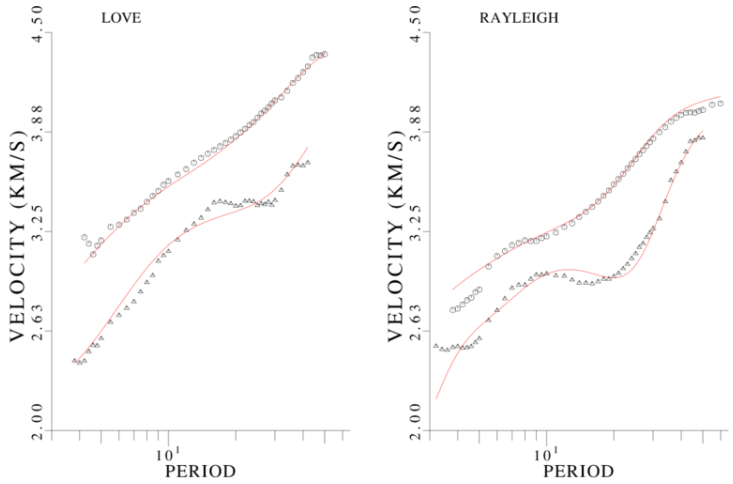

(b) OK028

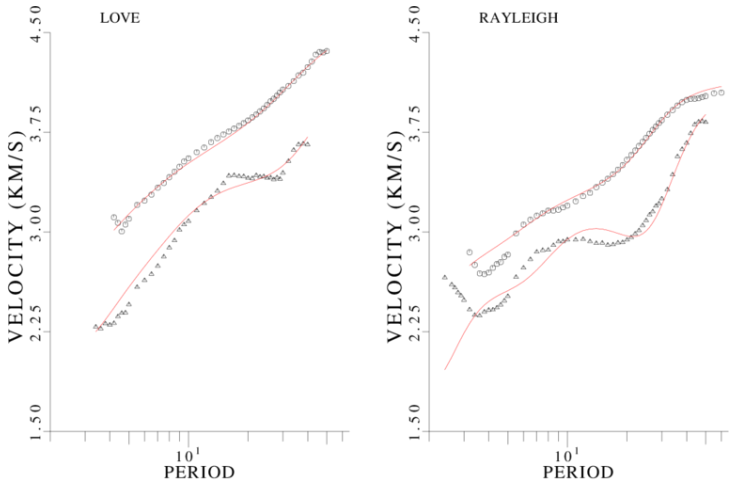

(c) OK027

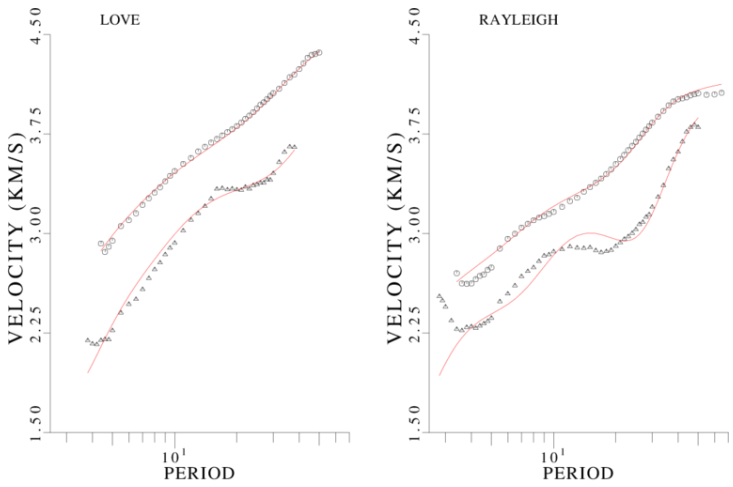

(d) BCOK

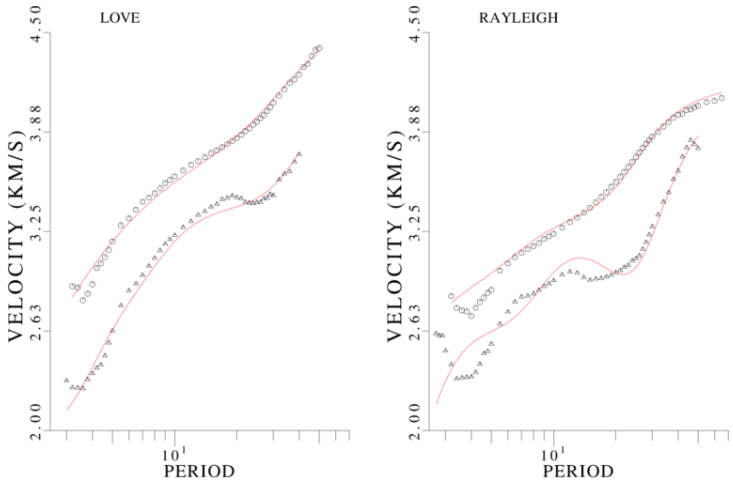

(e) CROK

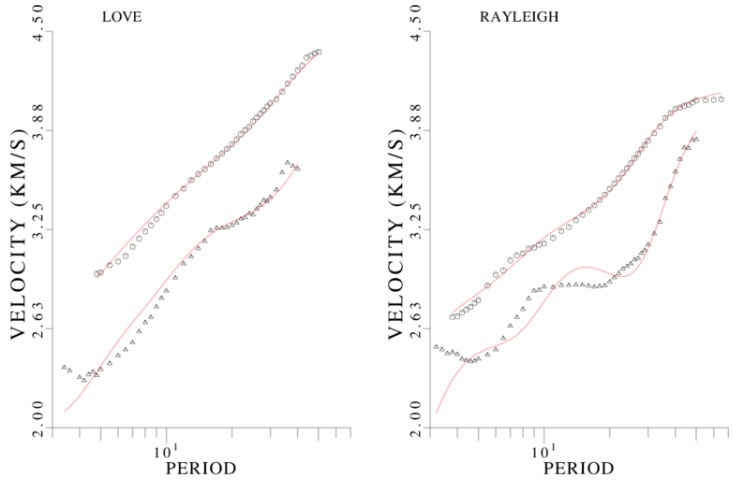

(f) FNO

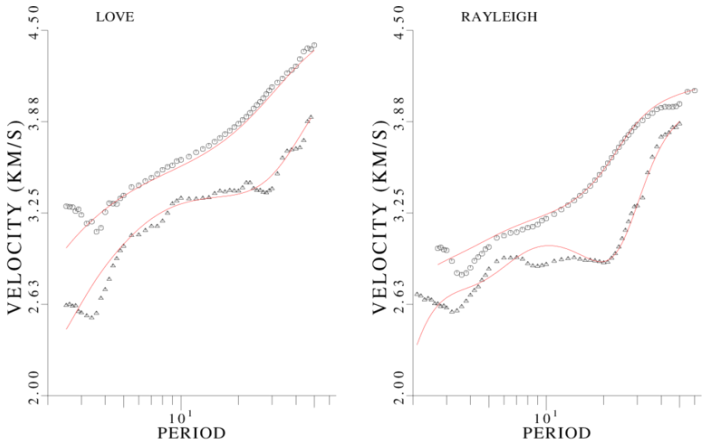

(g) QUOK

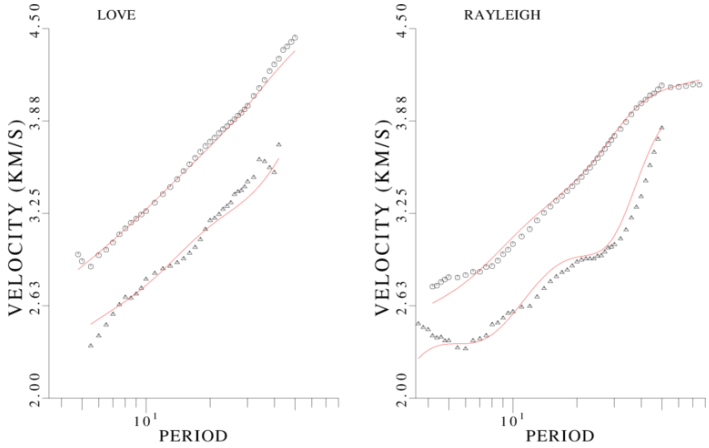

(h) X34A

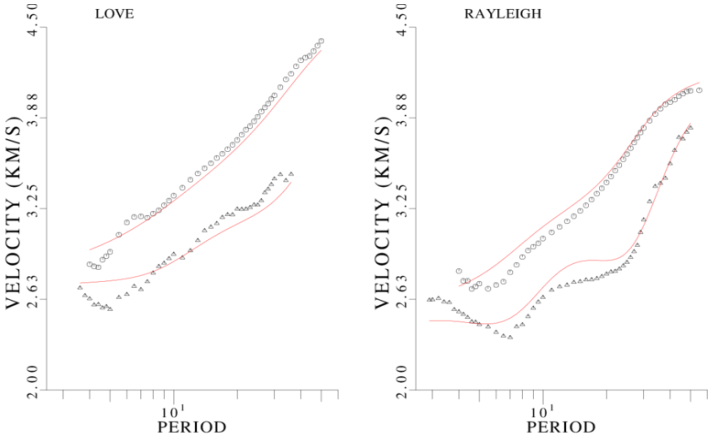

(i) X37A

Figure 5.3: The comparison of observed and predicted dispersion at selected stations, which are arranged by the same order in Figure 5.2. In each figure: Love wave dispersion (left), and Rayleigh wave dispersion (right). The observed phase velocity dispersion is given as black circles, and the observed group velocity dispersion is given as black triangles. The predicted dispersion is shown as red curves.

5.3.2 Fit to the receiver functions

Besides the surface wave dispersion, we also provide a comparison of observed and predicted receiver function. In Figure 5.4, red traces represent the predicted receiver functions, which are computed from the S-wave velocity models for three Gaussian filter parameters, α=0.5, α=1.0 and α=2.5. The observed receiver functions are given in blue. Some important information about receiver functions, such as α value and fit percent, are shown on the left side of each trace in Figure 5.4.

The predicted and the observed traces are fit well for all stations at low frequencies (α=0.5 and α=1.0). However, at high frequency (α=2.5), the fit of the traces are complicated. First of all, the effect of shallow thick sedimentary layers shown in the observed traces from 1 to 4 s are fit acceptably with the predicted traces, except at station X34A and FNO. Moreover, the fit of the PS peak around 6 s is relatively poor for some traces. One possible reason is that these observed traces are too noisy to be fit by the predicted traces. Similarly, most of the predicted receiver functions also fit relatively bad with the observed receiver functions after 6 s due to the same reason.

In fact, the stations for joint inversions were built in recent years (later than 2012). Some of them are located at either large basins with deep sediments (such as X37A in the Anadarko Basin) or fold mountains (such as X37A in the Ouachita Mountains), which might influence the quality of receiver functions. Thus good receiver functions for these stations are relatively rare due to limited events and these influence factors. However, in this study, we are interested in the upper

10 km crust where the majority of induced earthquakes occur. The receiver functions from 0 to 4 s are adequate to invert for well-determined S-wave velocity models at shallow depths (< 10 km).

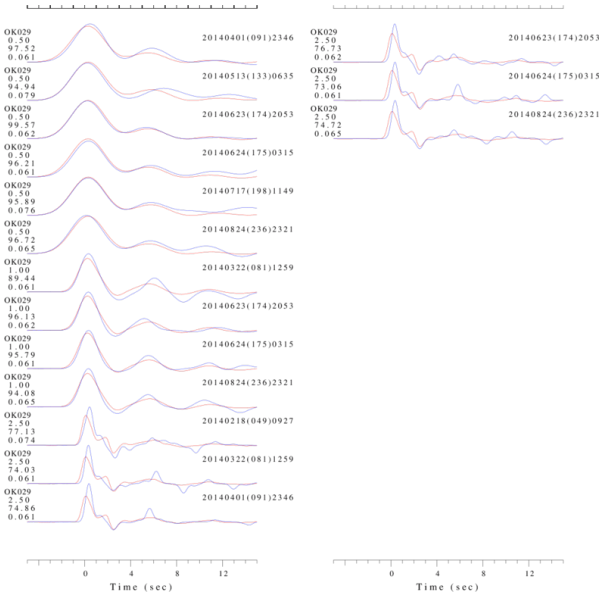

(a) OK029

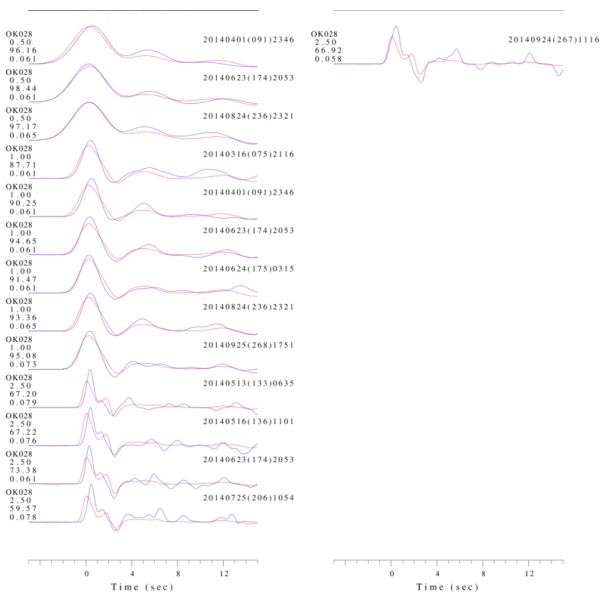

(b) OK028

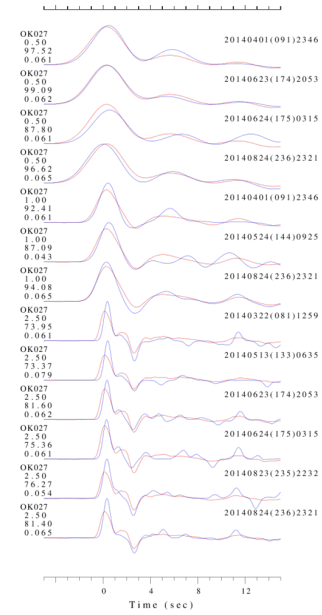

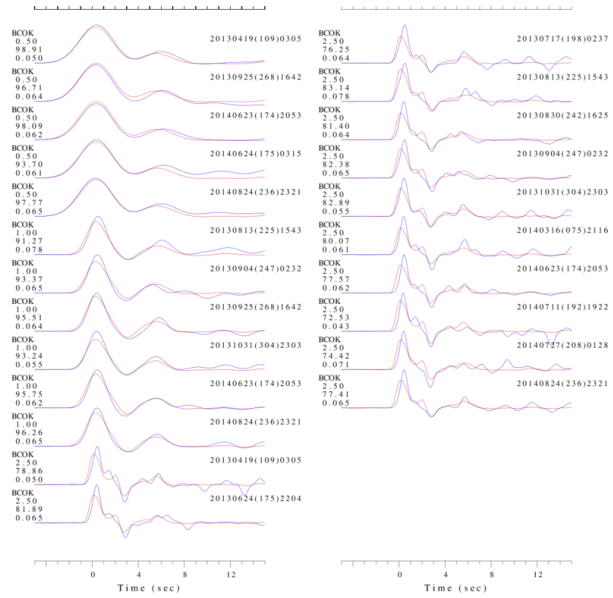

(c) OK027 (d) BCOK

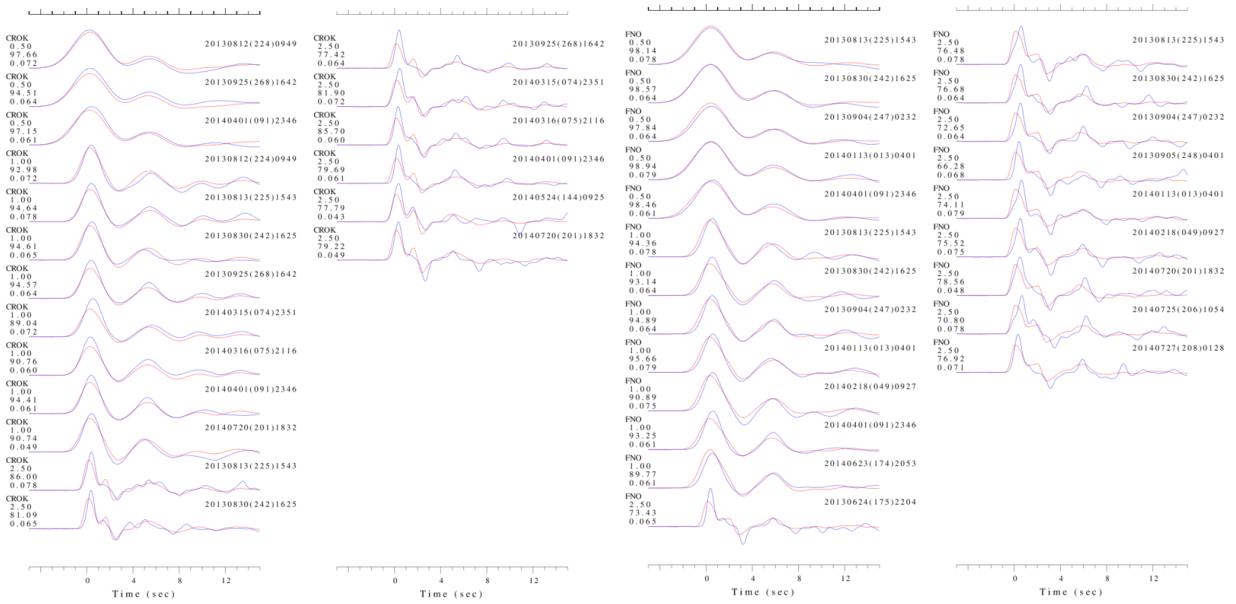

(e) CROK (f) FNO

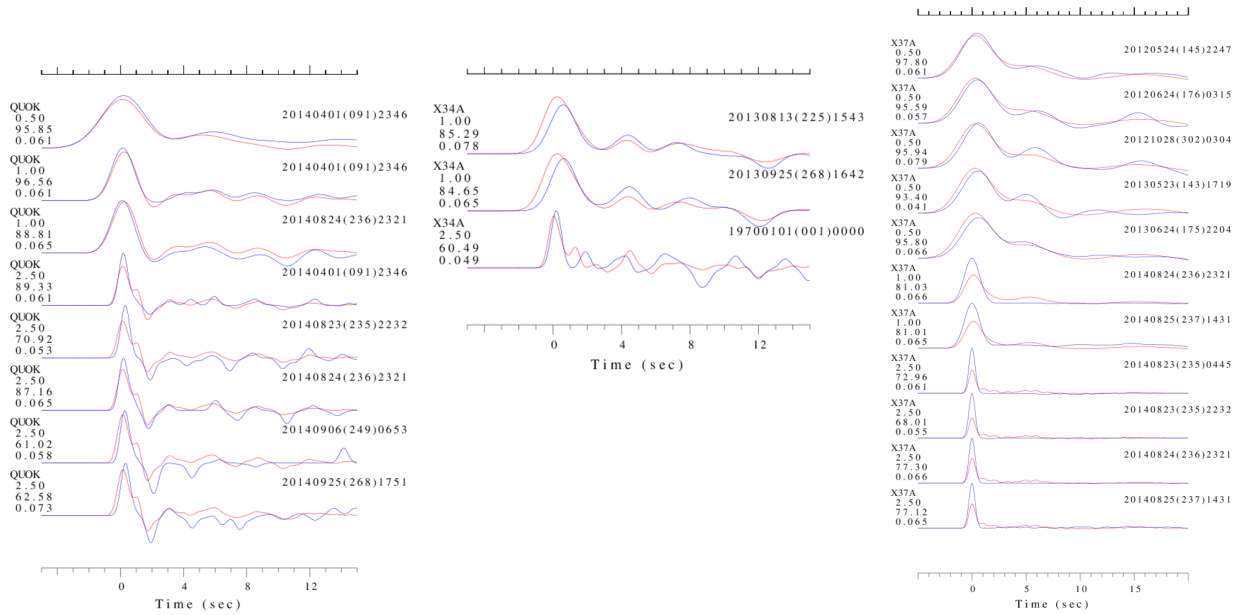

(g) QUOK (h) X34A (i) X37A

Figure 5.4: The comparison of observed and predicted receiver function at selected stations, which are arranged by the same order in Figure 5.2. The observed receiver function is shown as blue curves, and the predicted receiver function is shown as red curves. The left side of each trace shows the important information of the receiver function (from top to bottom): name, Gaussian filter parameter (α), fit percent, and ray parameter (s/km).

5.3.3 Forward tests

We use the McNamara *et al*.'s (2015) relocations to plot the record sections of local earthquakes. We processed the data by moment tensor source depth and plotted all with respect to origin time. The earthquakes near the stations OK027, OK028, and OK029 are used to plot the observed transverse waveforms for the source depths of 3-4 km and 7-9 km, respectively (Figure 5.5: a, c). The corresponding predicted transverse waveforms are generated from the velocity models at the three stations for the source depths of 4 km and 8 km, respectively (Figure 5.5: b, d). Here, we only discuss the test results at the station OK029, because the predicted waveforms for the three stations are similar to one another.

Figure 5.5 shows the comparison of predicted and observed waveform envelopes. Envelopes are plotted since differences in mechanism and azimuth may affect individual observed ray arrivals. The explanation of the observations in Figure 5.5 is simple if we consider a source beneath a simple layer. As distance increases, the number of rays that are almost supercritically trapped in the layer increases. As depth increases, this phenomenon starts at a longer distance.

It is apparent that the waveforms for different source depths show a completely different pattern (comparing Figure 5.5 a, b and c, d). Thus we believe that these earthquakes occur beneath the sedimentary layer, and the pattern supports the moment tensor depths that are greater than 3-4 km.

Besides, we also observed the agreement between the predicted and the observed waveforms. At a source depth of 4 km (Figure 5.5: a, b), the waveforms show the agreement in

the time intervals between the nearby two arrivals. For instance, the first arrival is earlier than the second arrival by 2 s in the observed waveforms (Figure 5.5, a), which is also shown in the predicted waveforms (Figure 5.5, b). In addition, the arrival times of each arrival for the predicted waveforms agree acceptably with the observed waveforms, except that some traces are slightly different in times. For example, the arrival time of the first arrival is about 6.7 s for the predicted waveforms, but 7.0 s for the observed waveforms at the distance of 20 km. At the source depth of 8 km (Figure 5.5: c, d), the predicted waveforms agree well with the observed waveforms in both arrival times and time intervals.

In the joint inversion process, we set several thin layers in the sedimentary section in the models in order to reach the agreement between the predicted and the observed data. In the forward test, this agreement in timing and appearance of multiples with distance provides confidence in the velocity models, which suggests that these models can be used for hypocenter relocation studies in the region.

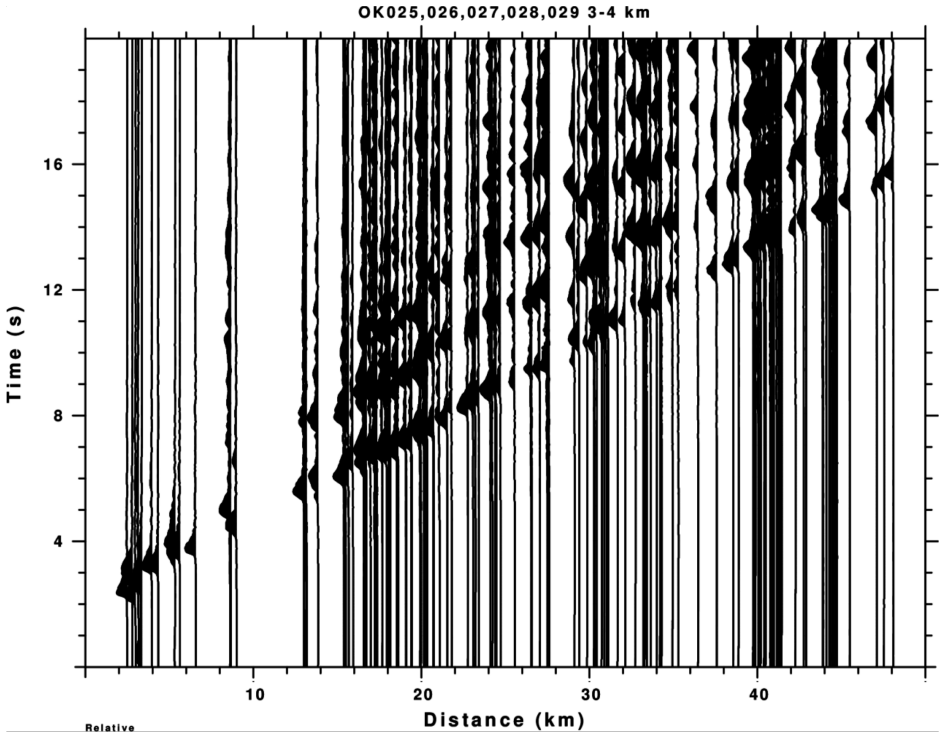
OK025,026,027,028,029 3-4 km
Time (s)
16
12
8
4
10
20
30
40
Distance (km)
Relative

(a)

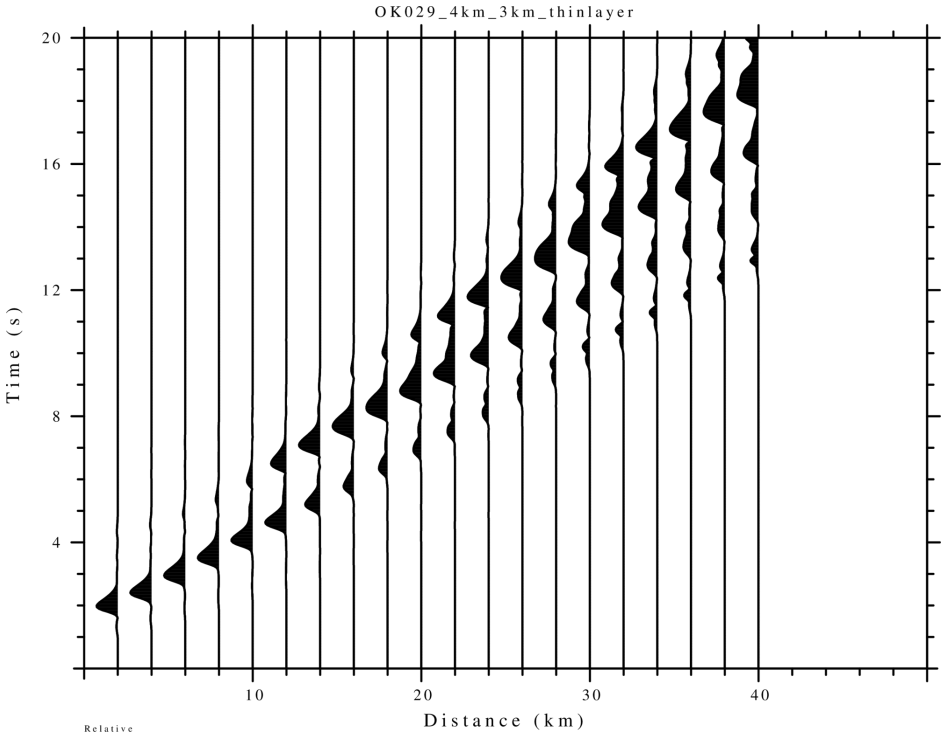
OK029_4km_3km_thinlayer
Time (s)
20
16
12
8
4
10
20
30
40
Distance (km)
Relative

(b)

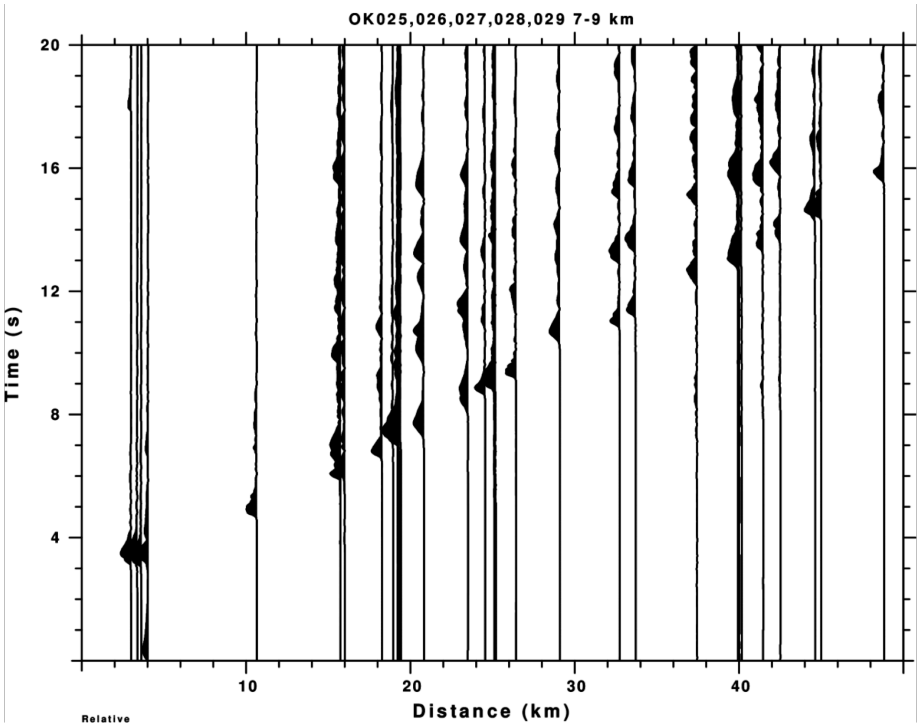

(c)

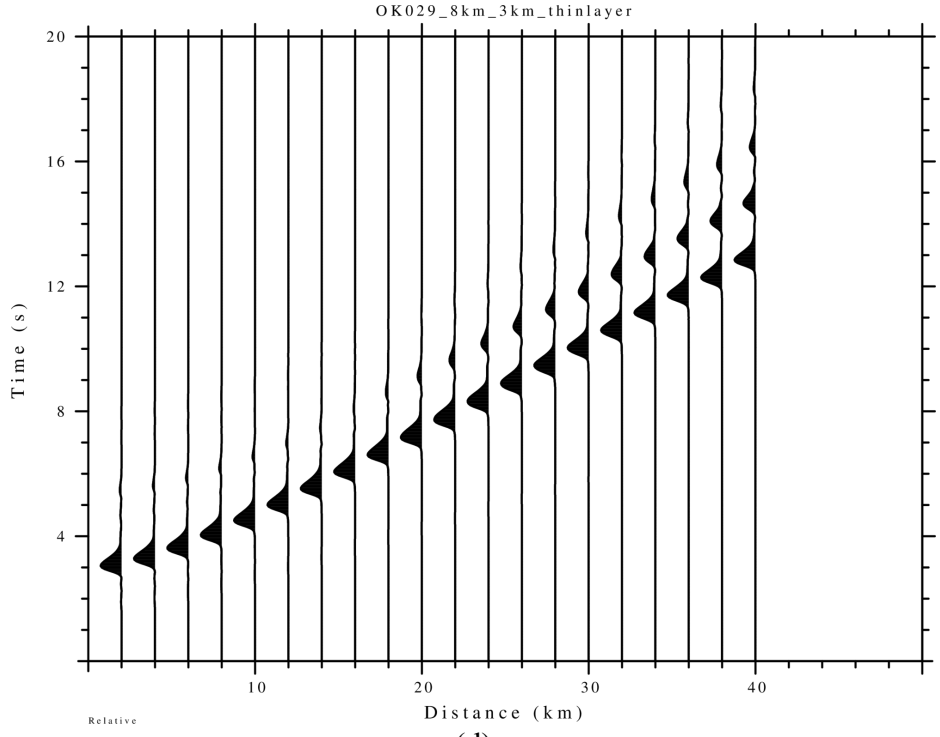

(d)

Figure 5.5: The comparison of observed and predicted trace envelops in the 0.5 – 2.0 Hz band at station OK029: (a) observed transverse waveforms for sources depths of 3 – 4 km, (b) predicted transverse waveforms for a source depth of 4 km, (c) observed transverse waveforms for sources depths of 7 – 9 km, and (b) predicted transverse waveforms for a source depth of 8 km.

CHAPTER 6: CONCLUSION

In this work, we obtained high-resolution phase and group velocity tomography maps (25 km × 25 km) from 2 s to 60 s periods for the Rayleigh wave and from 2 s to 50 s periods for the Love wave. The ambient noise data used for the cross-correlation was recorded from 2009 to 2011 at 133 TA stations across Oklahoma. We applied the Multiple Filter Technique to compute the fundamental mode phase and group velocity dispersion measurements for every inter-station path, which were used to inverse the tomography maps.

The tomography results show that the velocity variations are strong and related to shallow geology at short periods (≤ 20 s). At long period (40 s), the velocity variation dramatically decreased comparing with those maps at shorter periods, which suggests that the low velocity geological structures do not extend to deep depths.

Most significant geological structures are illustrated in the tomography maps. For instance, the fast velocity anomalies indicate uplift structures, such as Ozark Uplift. The slow velocity anomalies are associated with major basins, such as Arkoma Basin, with an exception that the Ouachita Uplift is represented by strong low velocity anomalies, which is associated with intense folding and faulting of sedimentary strata.

Besides, we conducted the receiver function analysis using the teleseismic data obtained from 3 GS stations and 6 OK stations from 2011 to 2014. Then we performed the joint inversion of surface wave dispersion and receiver functions to produce 1-D S-wave velocity models, which are also constrained by local geological structures. The derived velocity models not only match

the observed receiver functions and dispersions well but also provide a model at shallow depths that was tested with the independent data set of earthquake waveforms recorded at short distances. The comparison of model predictions to observed transverse waveforms supports the depths determined from the moment tensor inversions.

We suggest that the 1-D S-wave velocity models can be used to study hypocenter relocations in the region.

APPENDIX

This section presents upper 100 km of the velocity models for the selected stations. In these tables, H refers to thickness. V_P and V_S are the P-wave and S-wave velocities, respectively. ρ is the density. QP^{-1} and QS^{-1} represent the quality factors of P-wave and S-wave at the frequency f_P and f_S, respectively.

Table S1: OK029 Model

H (km)	Vp (km/s)	Vs (km/s)	ρ (kg/m)	QP^{-1}	QS^{-1}	f_P (Hz)	f_S (Hz)
1	3.7637	2.1504	2.2797	1.18E-03	1.67E-03	1	1
1	4.2691	2.4394	2.3575	1.18E-03	1.67E-03	1	1
1	4.7127	2.6925	2.434	1.18E-03	1.67E-03	1	1
1	6.2507	3.4865	2.7756	1.18E-03	1.67E-03	1	1
1	6.1633	3.4378	2.75	1.18E-03	1.67E-03	1	1
2	6.1272	3.4175	2.7387	1.18E-03	1.67E-03	1	1
2	6.2875	3.507	2.7859	1.18E-03	1.67E-03	1	1
2	6.4579	3.6019	2.8371	1.18E-03	1.67E-03	1	1
2	6.5879	3.6744	2.8726	1.18E-03	1.67E-03	1	1
2	6.6577	3.7136	2.8908	1.18E-03	1.67E-03	1	1
2	6.6554	3.7123	2.8904	1.18E-03	1.67E-03	1	1
2	6.6607	3.7154	2.8918	1.18E-03	1.67E-03	1	1
2	6.6415	3.7044	2.8867	1.18E-03	1.67E-03	1	1
2	6.6959	3.7354	2.9005	1.18E-03	1.67E-03	1	1
2	6.7657	3.7739	2.9185	1.18E-03	1.67E-03	1	1
2	6.8519	3.8218	2.9408	1.18E-03	1.67E-03	1	1
2	6.8366	3.8138	2.9372	1.18E-03	1.67E-03	1	1
2	6.7998	3.7928	2.9282	1.18E-03	1.67E-03	1	1
2	6.8208	3.8039	2.9339	1.18E-03	1.67E-03	1	1
2	6.8737	3.8343	2.9478	1.18E-03	1.67E-03	1	1
2	6.963	3.8837	2.971	1.18E-03	1.67E-03	1	1
2	7.0314	3.9221	2.9909	1.18E-03	1.67E-03	1	1
2	7.1145	3.9685	3.0176	1.18E-03	1.67E-03	1	1
2	7.2705	4.0549	3.0674	1.18E-03	1.67E-03	1	1
2	7.5151	4.192	3.1454	1.18E-03	1.67E-03	1	1
2	7.7923	4.346	3.2391	1.18E-03	1.67E-03	1	1
2	8.0524	4.4913	3.3282	1.18E-03	1.67E-03	1	1
2	8.267	4.6113	3.4053	1.18E-03	1.67E-03	1	1
5	8.4078	4.6897	3.4559	1.18E-03	1.67E-03	1	1
5	8.465	4.7227	3.4767	1.18E-03	1.67E-03	1	1
5	8.4619	4.7215	3.4757	1.18E-03	1.67E-03	1	1
5	8.404	4.69	3.4551	1.18E-03	1.67E-03	1	1
5	8.2795	4.6216	3.4108	1.18E-03	1.67E-03	1	1
5	8.1802	4.5581	3.3756	1.18E-03	1.67E-03	1	1
5	8.0807	4.5128	3.3404	1.18E-03	1.67E-03	1	1
5	8.0977	4.5234	3.3465	1.18E-03	1.67E-03	1	1
5	8.2185	4.589	3.3894	1.18E-03	1.67E-03	1	1
5	8.3576	4.6696	3.4386	1.18E-03	1.67E-03	1	1

Table S2: OK028 Model

H (km)	Vp (km/s)	Vs (km/s)	ρ (kg/m)	QP^{-1}	QS^{-1}	f_P (Hz)	f_S (Hz)
2	4.1569	2.3755	2.3428	1.18E-03	1.67E-03	1	1
1	4.5296	2.5885	2.3949	1.18E-03	1.67E-03	1	1
1	6.3755	3.5563	2.8116	1.18E-03	1.67E-03	1	1
1	6.3102	3.5197	2.7926	1.18E-03	1.67E-03	1	1
2	6.1637	3.4382	2.7492	1.18E-03	1.67E-03	1	1
2	6.2803	3.5029	2.7842	1.18E-03	1.67E-03	1	1
2	6.5219	3.6375	2.8557	1.18E-03	1.67E-03	1	1
2	6.6752	3.7234	2.8954	1.18E-03	1.67E-03	1	1
2	6.7028	3.7387	2.9026	1.18E-03	1.67E-03	1	1
2	6.6216	3.6932	2.8816	1.18E-03	1.67E-03	1	1
2	6.5424	3.6493	2.8613	1.18E-03	1.67E-03	1	1
2	6.5755	3.668	2.8695	1.18E-03	1.67E-03	1	1
2	6.5096	3.6306	2.8523	1.18E-03	1.67E-03	1	1
2	6.533	3.6443	2.8583	1.18E-03	1.67E-03	1	1
2	6.6025	3.6828	2.8764	1.18E-03	1.67E-03	1	1
2	6.7814	3.7824	2.923	1.18E-03	1.67E-03	1	1
2	6.995	3.9016	2.9786	1.18E-03	1.67E-03	1	1
2	7.1753	4.0021	3.036	1.18E-03	1.67E-03	1	1
2	7.2391	4.0378	3.0567	1.18E-03	1.67E-03	1	1
2	7.2518	4.0449	3.061	1.18E-03	1.67E-03	1	1
2	7.2445	4.0406	3.059	1.18E-03	1.67E-03	1	1
2	7.2494	4.0432	3.0608	1.18E-03	1.67E-03	1	1
2	7.317	4.0811	3.0825	1.18E-03	1.67E-03	1	1
2	7.4638	4.1635	3.1292	1.18E-03	1.67E-03	1	1
2	7.6731	4.2804	3.1992	1.18E-03	1.67E-03	1	1
2	7.9033	4.4087	3.2769	1.18E-03	1.67E-03	1	1
2	8.1341	4.5366	3.3576	1.18E-03	1.67E-03	1	1
5	8.3027	4.631	3.4179	1.18E-03	1.67E-03	1	1
5	8.3627	4.6653	3.4397	1.18E-03	1.67E-03	1	1
5	8.3548	4.6624	3.4374	1.18E-03	1.67E-03	1	1
5	8.3786	4.676	3.4463	1.18E-03	1.67E-03	1	1
5	8.4251	4.7033	3.4629	1.18E-03	1.67E-03	1	1
5	8.4067	4.6842	3.4564	1.18E-03	1.67E-03	1	1
5	8.3034	4.6369	3.4195	1.18E-03	1.67E-03	1	1
5	8.2336	4.599	3.3946	1.18E-03	1.67E-03	1	1
5	8.2122	4.5858	3.3869	1.18E-03	1.67E-03	1	1
5	8.2276	4.5974	3.3924	1.18E-03	1.67E-03	1	1

Table S3: OK027 Model

H (km)	Vp (km/s)	Vs (km/s)	ρ (kg/m)	QP^{-1}	QS^{-1}	f_P (Hz)	f_S (Hz)
1	3.6013	2.0578	2.251	1.18E-03	1.67E-03	1	1
1	3.8787	2.2163	2.2991	1.18E-03	1.67E-03	1	1
1	4.8348	2.7626	2.4604	1.18E-03	1.67E-03	1	1
1	6.6633	3.7169	2.8904	1.18E-03	1.67E-03	1	1
1	6.4367	3.5901	2.8305	1.18E-03	1.67E-03	1	1
2	6.2374	3.479	2.7714	1.18E-03	1.67E-03	1	1
2	6.2743	3.4997	2.7824	1.18E-03	1.67E-03	1	1
2	6.4769	3.6125	2.8431	1.18E-03	1.67E-03	1	1
2	6.5359	3.6452	2.8595	1.18E-03	1.67E-03	1	1
2	6.5385	3.6474	2.8603	1.18E-03	1.67E-03	1	1
2	6.5842	3.6727	2.8722	1.18E-03	1.67E-03	1	1
2	6.6386	3.7031	2.8863	1.18E-03	1.67E-03	1	1
2	6.6279	3.6967	2.8833	1.18E-03	1.67E-03	1	1
2	6.6198	3.6923	2.8806	1.18E-03	1.67E-03	1	1
2	6.6067	3.6846	2.8772	1.18E-03	1.67E-03	1	1
2	6.7598	3.7704	2.9169	1.18E-03	1.67E-03	1	1
2	6.9154	3.8574	2.9577	1.18E-03	1.67E-03	1	1
2	6.9744	3.8899	2.9736	1.18E-03	1.67E-03	1	1
2	7.0662	3.9412	3.0016	1.18E-03	1.67E-03	1	1
2	7.114	3.9683	3.0169	1.18E-03	1.67E-03	1	1
2	7.1392	3.982	3.0252	1.18E-03	1.67E-03	1	1
2	7.1637	3.9952	3.0333	1.18E-03	1.67E-03	1	1
2	7.2115	4.0224	3.0488	1.18E-03	1.67E-03	1	1
2	7.2911	4.067	3.0742	1.18E-03	1.67E-03	1	1
2	7.4025	4.129	3.1097	1.18E-03	1.67E-03	1	1
2	7.5462	4.2092	3.1564	1.18E-03	1.67E-03	1	1
2	7.7269	4.3101	3.2175	1.18E-03	1.67E-03	1	1
2	7.9562	4.4377	3.295	1.18E-03	1.67E-03	1	1
5	8.1909	4.5686	3.378	1.18E-03	1.67E-03	1	1
5	8.3969	4.6842	3.4519	1.18E-03	1.67E-03	1	1
5	8.4737	4.7281	3.48	1.18E-03	1.67E-03	1	1
5	8.5138	4.7519	3.4944	1.18E-03	1.67E-03	1	1
5	8.4858	4.737	3.4847	1.18E-03	1.67E-03	1	1
5	8.363	4.6603	3.441	1.18E-03	1.67E-03	1	1
5	8.2038	4.5815	3.3843	1.18E-03	1.67E-03	1	1
5	8.1432	4.5487	3.3627	1.18E-03	1.67E-03	1	1
5	8.1458	4.5489	3.3636	1.18E-03	1.67E-03	1	1
5	8.2674	4.6194	3.4067	1.18E-03	1.67E-03	1	1

Table S4: BCOK Model

H (km)	Vp (km/s)	Vs (km/s)	ρ (kg/m)	QP^{-1}	QS^{-1}	f_P (Hz)	f_S (Hz)
0.5	3.3009	1.8861	2.2014	1.18E-03	1.67E-03	1	1
0.5	3.3908	1.9377	2.2153	1.18E-03	1.67E-03	1	1
0.5	3.7204	2.1256	2.2709	1.18E-03	1.67E-03	1	1
0.5	4.1124	2.3499	2.3351	1.18E-03	1.67E-03	1	1
0.5	4.4773	2.5587	2.3849	1.18E-03	1.67E-03	1	1
0.5	4.623	2.6416	2.4134	1.18E-03	1.67E-03	1	1
2	6.3102	3.5198	2.7924	1.18E-03	1.67E-03	1	1
2	6.1858	3.4497	2.7558	1.18E-03	1.67E-03	1	1
2	6.2191	3.4688	2.7658	1.18E-03	1.67E-03	1	1
2	6.3741	3.5554	2.8125	1.18E-03	1.67E-03	1	1
2	6.5561	3.6568	2.8647	1.18E-03	1.67E-03	1	1
2	6.5929	3.6774	2.8745	1.18E-03	1.67E-03	1	1
2	6.6024	3.6827	2.8768	1.18E-03	1.67E-03	1	1
2	6.7041	3.7397	2.9028	1.18E-03	1.67E-03	1	1
2	6.7802	3.7823	2.9223	1.18E-03	1.67E-03	1	1
2	6.7947	3.7897	2.926	1.18E-03	1.67E-03	1	1
2	6.7461	3.7625	2.9135	1.18E-03	1.67E-03	1	1
2	6.7447	3.7622	2.9131	1.18E-03	1.67E-03	1	1
2	6.8448	3.8176	2.9388	1.18E-03	1.67E-03	1	1
2	6.8255	3.8072	2.9342	1.18E-03	1.67E-03	1	1
2	6.7887	3.7867	2.9255	1.18E-03	1.67E-03	1	1
2	6.9179	3.859	2.9592	1.18E-03	1.67E-03	1	1
2	7.0502	3.933	2.9969	1.18E-03	1.67E-03	1	1
2	7.1144	3.9682	3.0179	1.18E-03	1.67E-03	1	1
2	7.1728	4.0006	3.037	1.18E-03	1.67E-03	1	1
2	7.3017	4.0728	3.0781	1.18E-03	1.67E-03	1	1
2	7.5289	4.1996	3.1509	1.18E-03	1.67E-03	1	1
2	7.7956	4.3481	3.2409	1.18E-03	1.67E-03	1	1
2	8.0307	4.4796	3.3209	1.18E-03	1.67E-03	1	1
2	8.2119	4.5804	3.3858	1.18E-03	1.67E-03	1	1
5	8.3308	4.6469	3.4283	1.18E-03	1.67E-03	1	1
5	8.3761	4.6728	3.4446	1.18E-03	1.67E-03	1	1
5	8.348	4.6584	3.435	1.18E-03	1.67E-03	1	1
5	8.321	4.6437	3.4258	1.18E-03	1.67E-03	1	1
5	8.3218	4.6452	3.4261	1.18E-03	1.67E-03	1	1
5	8.3676	4.6622	3.4424	1.18E-03	1.67E-03	1	1
5	8.3486	4.6624	3.4357	1.18E-03	1.67E-03	1	1
5	8.2992	4.6353	3.4184	1.18E-03	1.67E-03	1	1
5	8.3056	4.6382	3.4205	1.18E-03	1.67E-03	1	1
5	8.3695	4.6767	3.4429	1.18E-03	1.67E-03	1	1

Table S5: CROK Model

H (km)	Vp (km/s)	Vs (km/s)	ρ (kg/m)	QP^{-1}	QS^{-1}	f_P (Hz)	f_S (Hz)
0.5	3.5243	2.0138	2.237	1.18E-03	1.67E-03	1	1
0.5	3.5583	2.0337	2.2429	1.18E-03	1.67E-03	1	1
0.5	3.8026	2.1732	2.2852	1.18E-03	1.67E-03	1	1
0.5	4.0836	2.3336	2.3311	1.18E-03	1.67E-03	1	1
0.5	4.5224	2.5845	2.3919	1.18E-03	1.67E-03	1	1
2	6.6124	3.688	2.8785	1.18E-03	1.67E-03	1	1
2	6.412	3.5763	2.8236	1.18E-03	1.67E-03	1	1
2	6.3831	3.5603	2.8148	1.18E-03	1.67E-03	1	1
2	6.3557	3.5454	2.8067	1.18E-03	1.67E-03	1	1
2	6.4143	3.5776	2.8243	1.18E-03	1.67E-03	1	1
2	6.4881	3.6191	2.8471	1.18E-03	1.67E-03	1	1
2	6.699	3.7364	2.902	1.18E-03	1.67E-03	1	1
2	6.8212	3.8044	2.9334	1.18E-03	1.67E-03	1	1
2	6.8807	3.8376	2.9485	1.18E-03	1.67E-03	1	1
2	6.8284	3.8086	2.9349	1.18E-03	1.67E-03	1	1
2	6.7761	3.7795	2.9214	1.18E-03	1.67E-03	1	1
2	6.7174	3.7463	2.9062	1.18E-03	1.67E-03	1	1
2	6.6695	3.7199	2.8938	1.18E-03	1.67E-03	1	1
2	6.6456	3.7071	2.8879	1.18E-03	1.67E-03	1	1
2	6.7356	3.7572	2.9115	1.18E-03	1.67E-03	1	1
2	6.8565	3.8247	2.9431	1.18E-03	1.67E-03	1	1
2	6.9345	3.8681	2.9635	1.18E-03	1.67E-03	1	1
2	7.0412	3.9271	2.994	1.18E-03	1.67E-03	1	1
2	7.2535	4.0459	3.0618	1.18E-03	1.67E-03	1	1
2	7.5647	4.219	3.1623	1.18E-03	1.67E-03	1	1
2	7.8662	4.388	3.2644	1.18E-03	1.67E-03	1	1
2	8.1047	4.5205	3.3474	1.18E-03	1.67E-03	1	1
2	8.2735	4.6148	3.4081	1.18E-03	1.67E-03	1	1
2	8.3871	4.6781	3.4489	1.18E-03	1.67E-03	1	1
5	8.4369	4.7054	3.4668	1.18E-03	1.67E-03	1	1
5	8.3384	4.6524	3.4318	1.18E-03	1.67E-03	1	1
5	8.1414	4.5429	3.3614	1.18E-03	1.67E-03	1	1
5	8.0194	4.4757	3.3177	1.18E-03	1.67E-03	1	1
5	8.0496	4.4928	3.3284	1.18E-03	1.67E-03	1	1
5	8.1955	4.5667	3.3806	1.18E-03	1.67E-03	1	1
5	8.3523	4.6644	3.4366	1.18E-03	1.67E-03	1	1
5	8.4576	4.724	3.4742	1.18E-03	1.67E-03	1	1
5	8.3883	4.6839	3.4494	1.18E-03	1.67E-03	1	1
5	8.2415	4.605	3.3968	1.18E-03	1.67E-03	1	1

Table S6: FNO Model

H (km)	Vp (km/s)	Vs (km/s)	ρ (kg/m)	QP^{-1}	QS^{-1}	f_P (Hz)	f_S (Hz)
0.5	3.4843	1.9909	2.2284	1.18E-03	1.67E-03	1	1
0.5	3.402	1.9438	2.2158	1.18E-03	1.67E-03	1	1
0.5	3.5238	2.0134	2.2353	1.18E-03	1.67E-03	1	1
0.5	3.7534	2.1444	2.2756	1.18E-03	1.67E-03	1	1
0.5	4.5674	2.6099	2.4021	1.18E-03	1.67E-03	1	1
0.5	4.558	2.6046	2.4004	1.18E-03	1.67E-03	1	1
2	6.246	3.4838	2.7741	1.18E-03	1.67E-03	1	1
2	6.1911	3.4536	2.7575	1.18E-03	1.67E-03	1	1
2	6.1561	3.4336	2.7467	1.18E-03	1.67E-03	1	1
2	6.2568	3.4898	2.7775	1.18E-03	1.67E-03	1	1
2	6.4516	3.5983	2.836	1.18E-03	1.67E-03	1	1
2	6.6689	3.7198	2.8939	1.18E-03	1.67E-03	1	1
2	6.6946	3.7338	2.9005	1.18E-03	1.67E-03	1	1
2	6.7652	3.7731	2.9187	1.18E-03	1.67E-03	1	1
2	6.8934	3.8447	2.9517	1.18E-03	1.67E-03	1	1
2	6.9239	3.8616	2.9595	1.18E-03	1.67E-03	1	1
2	6.7584	3.7697	2.917	1.18E-03	1.67E-03	1	1
2	6.617	3.6909	2.8805	1.18E-03	1.67E-03	1	1
2	6.6599	3.7151	2.8913	1.18E-03	1.67E-03	1	1
2	6.7528	3.7665	2.9153	1.18E-03	1.67E-03	1	1
2	6.8453	3.8186	2.9394	1.18E-03	1.67E-03	1	1
2	6.909	3.8538	2.9562	1.18E-03	1.67E-03	1	1
2	6.9637	3.8843	2.9708	1.18E-03	1.67E-03	1	1
2	7.0423	3.9282	2.9943	1.18E-03	1.67E-03	1	1
2	7.1347	3.9797	3.0244	1.18E-03	1.67E-03	1	1
2	7.2776	4.0591	3.0701	1.18E-03	1.67E-03	1	1
2	7.5031	4.1852	3.1421	1.18E-03	1.67E-03	1	1
2	7.7925	4.3463	3.2398	1.18E-03	1.67E-03	1	1
2	8.0793	4.5066	3.3382	1.18E-03	1.67E-03	1	1
2	8.3058	4.6328	3.4195	1.18E-03	1.67E-03	1	1
5	8.4277	4.7007	3.4634	1.18E-03	1.67E-03	1	1
5	8.3851	4.6775	3.4486	1.18E-03	1.67E-03	1	1
5	8.2253	4.5893	3.392	1.18E-03	1.67E-03	1	1
5	8.2332	4.5949	3.3946	1.18E-03	1.67E-03	1	1
5	8.3431	4.657	3.4334	1.18E-03	1.67E-03	1	1
5	8.4572	4.7123	3.4738	1.18E-03	1.67E-03	1	1
5	8.4613	4.7251	3.4752	1.18E-03	1.67E-03	1	1
5	8.3657	4.672	3.4414	1.18E-03	1.67E-03	1	1
5	8.2957	4.6328	3.4166	1.18E-03	1.67E-03	1	1
5	8.3302	4.6542	3.4288	1.18E-03	1.67E-03	1	1

Table S7: QUOK Model

H (km)	Vp (km/s)	Vs (km/s)	ρ (kg/m)	QP^{-1}	QS^{-1}	f_P (Hz)	f_S (Hz)
0.5	3.3601	1.9201	2.2087	1.18E-03	1.67E-03	1	1
1	3.5556	2.0316	2.2398	1.18E-03	1.67E-03	1	1
1	6.2363	3.4782	2.7717	1.18E-03	1.67E-03	1	1
1	6.3639	3.5498	2.8088	1.18E-03	1.67E-03	1	1
2	6.3692	3.5522	2.8104	1.18E-03	1.67E-03	1	1
2	6.4298	3.5863	2.8286	1.18E-03	1.67E-03	1	1
2	6.3676	3.5517	2.8101	1.18E-03	1.67E-03	1	1
2	6.2468	3.4845	2.7741	1.18E-03	1.67E-03	1	1
2	6.2932	3.5104	2.788	1.18E-03	1.67E-03	1	1
2	6.3666	3.5512	2.8102	1.18E-03	1.67E-03	1	1
2	6.3548	3.5448	2.8068	1.18E-03	1.67E-03	1	1
2	6.4856	3.6175	2.8457	1.18E-03	1.67E-03	1	1
2	6.6937	3.7336	2.9004	1.18E-03	1.67E-03	1	1
2	6.8594	3.8256	2.9433	1.18E-03	1.67E-03	1	1
2	6.8143	3.8005	2.9316	1.18E-03	1.67E-03	1	1
2	6.7125	3.7443	2.9053	1.18E-03	1.67E-03	1	1
2	6.8508	3.8211	2.941	1.18E-03	1.67E-03	1	1
2	6.9619	3.8832	2.9699	1.18E-03	1.67E-03	1	1
2	7.0007	3.905	2.9803	1.18E-03	1.67E-03	1	1
2	7.0993	3.9594	3.0117	1.18E-03	1.67E-03	1	1
2	7.2113	4.0216	3.0474	1.18E-03	1.67E-03	1	1
2	7.3212	4.0835	3.0827	1.18E-03	1.67E-03	1	1
2	7.4326	4.1455	3.1185	1.18E-03	1.67E-03	1	1
2	7.5523	4.2125	3.1582	1.18E-03	1.67E-03	1	1
2	7.716	4.3038	3.2139	1.18E-03	1.67E-03	1	1
2	7.9229	4.4185	3.2841	1.18E-03	1.67E-03	1	1
2	8.1258	4.5325	3.3552	1.18E-03	1.67E-03	1	1
5	8.2455	4.5993	3.398	1.18E-03	1.67E-03	1	1
5	8.221	4.5861	3.3892	1.18E-03	1.67E-03	1	1
5	8.1119	4.5262	3.3504	1.18E-03	1.67E-03	1	1
5	8.1069	4.5243	3.3488	1.18E-03	1.67E-03	1	1
5	8.226	4.5918	3.3916	1.18E-03	1.67E-03	1	1
5	8.3316	4.6426	3.4298	1.18E-03	1.67E-03	1	1
5	8.3451	4.6604	3.4346	1.18E-03	1.67E-03	1	1
5	8.3051	4.6391	3.4199	1.18E-03	1.67E-03	1	1
5	8.1795	4.5674	3.3747	1.18E-03	1.67E-03	1	1
5	8.1261	4.5406	3.3554	1.18E-03	1.67E-03	1	1

Table S8: X34A Model

H (km)	Vp (km/s)	Vs (km/s)	ρ (kg/m)	QP^{-1}	QS^{-1}	f_P (Hz)	f_S (Hz)
1	3.8664	2.2092	2.2978	1.18E-03	1.67E-03	1	1
1	4.0003	2.286	2.3209	1.18E-03	1.67E-03	1	1
1	4.7658	2.7231	2.448	1.18E-03	1.67E-03	1	1
1	5.0876	2.9075	2.5154	1.18E-03	1.67E-03	1	1
1	5.5777	3.1875	2.6135	1.18E-03	1.67E-03	1	1
1	5.3295	3.0458	2.5651	1.18E-03	1.67E-03	1	1
1	5.2974	3.0266	2.5596	1.18E-03	1.67E-03	1	1
1	5.1715	2.9545	2.5351	1.18E-03	1.67E-03	1	1
2	6.4053	3.5726	2.8226	1.18E-03	1.67E-03	1	1
2	6.4215	3.5816	2.8272	1.18E-03	1.67E-03	1	1
2	6.5094	3.6309	2.8529	1.18E-03	1.67E-03	1	1
2	6.5968	3.6792	2.8751	1.18E-03	1.67E-03	1	1
2	6.6043	3.6834	2.8768	1.18E-03	1.67E-03	1	1
2	6.5237	3.6385	2.8562	1.18E-03	1.67E-03	1	1
2	6.6884	3.7309	2.8988	1.18E-03	1.67E-03	1	1
2	6.9347	3.8678	2.9624	1.18E-03	1.67E-03	1	1
2	7.1052	3.9628	3.0122	1.18E-03	1.67E-03	1	1
2	6.9563	3.88	2.9679	1.18E-03	1.67E-03	1	1
2	6.8967	3.8467	2.953	1.18E-03	1.67E-03	1	1
2	7.0493	3.932	2.9954	1.18E-03	1.67E-03	1	1
2	7.165	3.9967	3.0323	1.18E-03	1.67E-03	1	1
2	7.2272	4.0316	3.0525	1.18E-03	1.67E-03	1	1
2	7.206	4.0188	3.0459	1.18E-03	1.67E-03	1	1
2	7.1501	3.988	3.0283	1.18E-03	1.67E-03	1	1
2	7.1661	3.997	3.0335	1.18E-03	1.67E-03	1	1
2	7.2543	4.0459	3.0619	1.18E-03	1.67E-03	1	1
2	7.4343	4.1461	3.1198	1.18E-03	1.67E-03	1	1
2	7.6102	4.2442	3.1786	1.18E-03	1.67E-03	1	1
5	7.833	4.3689	3.2545	1.18E-03	1.67E-03	1	1
5	8.0973	4.5173	3.3462	1.18E-03	1.67E-03	1	1
5	8.3878	4.6803	3.45	1.18E-03	1.67E-03	1	1
5	8.6395	4.8218	3.5373	1.18E-03	1.67E-03	1	1
5	8.7347	4.8759	3.5695	1.18E-03	1.67E-03	1	1
5	8.6751	4.8335	3.5496	1.18E-03	1.67E-03	1	1
5	8.5499	4.7748	3.5074	1.18E-03	1.67E-03	1	1
5	8.5036	4.7498	3.4913	1.18E-03	1.67E-03	1	1
5	8.5639	4.7824	3.511	1.18E-03	1.67E-03	1	1
5	8.5629	4.7847	3.5099	1.18E-03	1.67E-03	1	1

Table S9: X37A Model

H (km)	Vp (km/s)	Vs (km/s)	ρ (kg/m)	QP^{-1}	QS^{-1}	f_P (Hz)	f_S (Hz)
2	4.8399	2.6999	2.4657	1.18E-03	1.67E-03	1	1
2	5.1532	2.874	2.5303	1.18E-03	1.67E-03	1	1
2	5.3797	3.0004	2.5758	1.18E-03	1.67E-03	1	1
2	5.6854	3.1713	2.637	1.18E-03	1.67E-03	1	1
2	6.0081	3.3512	2.702	1.18E-03	1.67E-03	1	1
2	6.2246	3.4719	2.7672	1.18E-03	1.67E-03	1	1
2	6.3807	3.5591	2.8143	1.18E-03	1.67E-03	1	1
2	6.5154	3.6345	2.8542	1.18E-03	1.67E-03	1	1
2	6.5995	3.681	2.8761	1.18E-03	1.67E-03	1	1
2	6.643	3.7051	2.8875	1.18E-03	1.67E-03	1	1
2	6.6762	3.724	2.8961	1.18E-03	1.67E-03	1	1
2	6.7068	3.7406	2.9037	1.18E-03	1.67E-03	1	1
2	6.7243	3.7508	2.9081	1.18E-03	1.67E-03	1	1
2	6.7405	3.7599	2.9122	1.18E-03	1.67E-03	1	1
2	6.7791	3.7813	2.9222	1.18E-03	1.67E-03	1	1
2	6.835	3.8123	2.9368	1.18E-03	1.67E-03	1	1
2	6.9217	3.8607	2.9595	1.18E-03	1.67E-03	1	1
2	7.0336	3.9232	2.9908	1.18E-03	1.67E-03	1	1
2	7.1637	3.9956	3.0326	1.18E-03	1.67E-03	1	1
2	7.31	4.0771	3.0795	1.18E-03	1.67E-03	1	1
2	7.4666	4.1647	3.1295	1.18E-03	1.67E-03	1	1
2	7.621	4.2508	3.1812	1.18E-03	1.67E-03	1	1
2	7.7677	4.3326	3.2311	1.18E-03	1.67E-03	1	1
2	7.9034	4.4084	3.2772	1.18E-03	1.67E-03	1	1
2	8.0441	4.4867	3.3258	1.18E-03	1.67E-03	1	1
5	8.1606	4.5516	3.3676	1.18E-03	1.67E-03	1	1
5	8.2648	4.6108	3.405	1.18E-03	1.67E-03	1	1
5	8.3475	4.6578	3.4347	1.18E-03	1.67E-03	1	1
5	8.3989	4.6874	3.4532	1.18E-03	1.67E-03	1	1
5	8.4142	4.6969	3.4589	1.18E-03	1.67E-03	1	1
5	8.4173	4.6901	3.4603	1.18E-03	1.67E-03	1	1
5	8.3747	4.6768	3.4453	1.18E-03	1.67E-03	1	1
5	8.3495	4.664	3.4363	1.18E-03	1.67E-03	1	1
5	8.3199	4.6458	3.4257	1.18E-03	1.67E-03	1	1
5	8.2804	4.6269	3.4116	1.18E-03	1.67E-03	1	1

BIBLIOGRAPHY

Abramowitz, M., & Stegun, I. A. (1965). *Handbook of mathematical functions* (Vol. 1046). New York: Dover.

Ammon, C. J. (1991). The isolation of receiver effects from teleseismic P waveforms. *Bull. Seismol. Soc. Am*, *81*(6), 2504-2510.

Bensen, G. D., Ritzwoller, M. H., & Shapiro, N. M. (2008). Broadband ambient noise surface wave tomography across the United States. *Journal of Geophysical Research: Solid Earth (1978–2012)*, *113*(B5).

Bhattacharya, S. N. (1983). Higher order accuracy in multiple filter technique. *Bulletin of the Seismological Society of America*, *73*(5), 1395-1406.

Campillo, M., & Paul, A. (2003). Long-range correlations in the diffuse seismic coda. *Science*, *299*(5606), 547-549.

Chiu, J. M., Johnston, A. C., & Yang, Y. T. (1992). Imaging the active faults of the central New Madrid seismic zone using PANDA array data. *Seismological Research Letters,* 63(3), 375-393.

Cho, K. H., Herrmann, R. B., Ammon, C. J., & Lee, K. (2007). Imaging the upper crust of the Korean Peninsula by surface-wave tomography. *Bulletin of the Seismological Society of America*, *97*(1B), 198-207.

Dziewonski, A., Bloch, S., & Landisman, M. (1969). A technique for the analysis of transient seismic signals. *Bulletin of the seismological Society of America*, *59*(1), 427-444.

Ekström, G., Tromp, J., & Larson, E. W. (1997). Measurements and global models of surface wave propagation. *Journal of Geophysical Research: Solid Earth (1978–2012)*, *102*(B4), 8137-8157.

Ekström, G. (2011). A global model of Love and Rayleigh surface wave dispersion and anisotropy, 25-250 s. *Geophysical Journal International*, *187*(3), 1668-1686.

Ekström, G. (2014). Love and Rayleigh phase-velocity maps, 5–40 s, of the western and central USA from USArray data. *Earth and Planetary Science Letters*, *402*, 42-49.

Evanzia, D., Pulliam, J., Ainsworth, R., Gurrola, H., & Pratt, K. (2014). Seismic Vp & Vs tomography of Texas & Oklahoma with a focus on the Gulf Coast margin. *Earth and Planetary Science Letters*, *402*, 148-156.

Frohlich, C., Ellsworth, W., Brown, W. A., Brunt, M., Luetgert, J., MacDonald, T., & Walter, S. (2014). The 17 May 2012 M4. 8 earthquake near Timpson, East Texas: An event possibly triggered by fluid injection. *Journal of Geophysical Research: Solid Earth*, *119*(1), 581-593.

Herrmann, R. B. (1973). Some aspects of band-pass filtering of surface waves. *Bulletin of the Seismological Society of America*, *63*(2), 663-671.

Herrmann, R. B. (1979). Surface wave focal mechanisms for eastern North American earthquakes with tectonic implications. *Journal of Geophysical Research: Solid Earth (1978–2012)*, *84*(B7), 3543-3552.

Herrmann, R. B., & Ammon, C. J. (1997). Faulting parameters of earthquakes in the New Madrid, Missouri, region. *Engineering geology*, *46*(3), 299-311.

Herrmann, R. B., Ammon, C. J. (2002), Surface waves, receiver functions and crustal structure, in *Computer Programs in Seismology*, Version 3.30, Saint Louis University. http://www.eas.slu.edu/eqc/eqccps.html

Herrmann, R. B., Benz, H., & Ammon, C. J. (2011). Monitoring the earthquake source process in North America. *Bulletin of the Seismological Society of America*, *101*(6), 2609-2625.

Herrmann, R. B., Ammon, C. J., & Benz, H. (2013). Group velocity dispersion for North America. Accessed Aug 1st, 2015, http://www.eas.slu.edu/eqc/eqc_research/NATOMO

Herrmann, R. B. (2013), Update to do_mft for the determination of phase velocities from empirical Green's functions from noise cross-correlation, in *Computer Programs in Seismology – Tutorials,* accessed Aug 8th, 2015, http://www.eas.slu.edu/eqc/eqc_cps/TUTORIAL/EMPIRICAL_GREEN/index.html

Hough, S. E. (2014). Shaking from injection‐induced earthquakes in the central and eastern United States. *Bulletin of the Seismological Society of America*.

Jachens, R. C., Simpson, R. W., Blakely, R. J., & Saltus, R. W. (1989). Isostatic residual gravity and crustal geology of the United States. *Geological Society of America Memoirs*, *172*, 405-424.

Jin, G., & Gaherty, J. B. (2015). Surface wave phase-velocity tomography based on multichannel cross-correlation. *Geophysical Journal International*, *201*(3), 1383-1398.

Johnson, K. S., Amsden, T. W., Denison, R. E., Dutton, S. P., Goldstein, A. G., Rascoe Jr, B., ... & Thompson, D. M. (1988). Southern Midcontinent Region – Geologic Provinces, Basement Rocks, Thickness and Dominant Lithologies of Sedimentary Rocks, *Sedimentary cover—North American craton: US: Boulder, Colorado, Geological Society of America, The Geology of North America*, *2*, 261-306.

Johnson, K. S., & Luza, K. V. (2008). Earth sciences and mineral resources of Oklahoma. *Oklahoma Geological Survey*.

Julià, J., Ammon, C. J., Herrmann, R. B., & Correig, A. M. (2000). Joint inversion of receiver function and surface wave dispersion observations. *Geophysical Journal International*, *143*(1), 99-112.

Julià, J., Ammon, C. J., & Herrmann, R. B. (2003). Lithospheric structure of the Arabian Shield from the joint inversion of receiver functions and surface-wave group velocities. *Tectonophysics*, *371*(1), 1-21.

Kafka, A. L., & Reiter, E. C. (1987). Dispersion of Rg waves in southeastern Maine: Evidence for lateral anisotropy in the shallow crust. *Bulletin of the Seismological Society of America*, *77*(3), 925-941.

Kane, M. F., & Godson, R. H. (1989). A crust/mantle structural framework of the conterminous United States based on gravity and magnetic trends. *Geological Society of America Memoirs*, *172*, 383-404.

Keranen, K. M., Savage, H. M., Abers, G. A., & Cochran, E. S. (2013). Potentially induced earthquakes in Oklahoma, USA: Links between wastewater injection and the 2011 Mw 5.7 earthquake sequence. *Geology*, *41*(6), 699-702.

Keranen, K. M., Weingarten, M., Abers, G. A., Bekins, B. A., & Ge, S. (2014). Sharp increase in central Oklahoma seismicity since 2008 induced by massive wastewater injection. *Science*, *345*(6195), 448-451.

Kikuchi, M., & Kanamori, H. (1982). Inversion of complex body waves. *Bulletin of the Seismological Society of America*, *72*(2), 491-506.

Kocaoğlu, A. H., & Long, L. T. (1993). Tomographic inversion of Rg wave group velocities for regional near‐surface velocity structure. *Journal of Geophysical Research: Solid Earth (1978–2012)*, *98*(B4), 6579-6587.

Langston, C. A. (1979). Structure under Mount Rainier, Washington, inferred from teleseismic body waves. *Journal of Geophysical Research: Solid Earth (1978–2012)*, *84*(B9), 4749-4762.

Langston, C. A., & Horton, S. P. (2014). Three‐Dimensional Seismic‐Velocity Model for the Unconsolidated Mississippi Embayment Sediments from H/V Ambient Noise Measurements. *Bulletin of the Seismological Society of America*, *104*(5), 2349-2358.

Lin, F. C., Moschetti, M. P., & Ritzwoller, M. H. (2008). Surface wave tomography of the western United States from ambient seismic noise: Rayleigh and Love wave phase velocity maps. *Geophysical Journal International*, *173*(1), 281-298.

Liang, C., & Langston, C. A. (2008). Ambient seismic noise tomography and structure of eastern North America. *Journal of Geophysical Research: Solid Earth (1978–2012)*, *113*(B3).

Ligorría, J. P., & Ammon, C. J. (1999). Iterative deconvolution and receiver-function estimation. *Bulletin of the seismological Society of America*, *89*(5), 1395-1400.

Lowrie, W. (2007). *Fundamentals of geophysics*. Cambridge University Press.

Luza, K. V., and Lawson, J. E., Jr., 1982, Seismicity and tectonic relationships of the Nemaha uplift in Oklahoma, part IV, *Oklahoma Geological Survey*, Special Publication 82-1, 52p.

"Magnitude 5.6 – Oklahoma, Earthquake Summary" (2011). *USGS Earthquake Hazards Program*, accessed April 10th, 2015, http://earthquake.usgs.gov/earthquakes/eqinthenews/2011/usb0006klz/#summary

McNamara, D. E., Benz, H. M., Herrmann, R. B., Bergman, E. A., Earle, P., Holland, A., ... & Gassner, A. (2015). Earthquake hypocenters and focal mechanisms in central Oklahoma reveal a complex system of reactivated subsurface strike‐slip faulting. *Geophysical Research Letters*, *42*(8), 2742-2749.

Menke, W. (2012). Geophysical data analysis: discrete inverse theory. *Academic press*.

"Ohio Quakes Probably Triggered by Waste Disposal Well, Say Seismologists" (2012), *Lamont-Doherty Earth Observatory, Earth Institute, Columbia University*, accessed April 10th, 2015,
http://www.ldeo.columbia.edu/news-events/seismologists-link-ohio-earthquakes-waste-disposal-wells

"Oil and Gas Data Files", *Oklahoma Corporation Commission*, accessed April 5th, 2015,
http://imaging.occeweb.com/

Owens, T. J., Zandt, G., & Taylor, S. R. (1984). Seismic evidence for an ancient rift beneath the Cumberland Plateau, Tennessee: A detailed analysis of broadband teleseismic P waveforms. *Journal of Geophysical Research: Solid Earth (1978–2012)*, *89*(B9), 7783-7795.

Phinney, R. A., & Roy-Chowdhury, K. (1989). Reflection seismic studies of crustal structure in the eastern United States. *Geological Society of America Memoirs*, *172*, 613-624.

Pollitz, F. F., & Mooney, W. D. (2014). Seismic structure of the Central US crust and shallow upper mantle: Uniqueness of the Reelfoot Rift. *Earth and Planetary Science Letters*, *402*, 157-166.

Ramírez‐Guzmán, L., Boyd, O. S., Hartzell, S., & Williams, R. A. (2012). Seismic velocity model of the central United States (Version 1): description and simulation of the 18 April 2008 Mt. Carmel, Illinois, earthquake. *Bulletin of the Seismological Society of America*, *102*(6), 2622-2645.

Ritzwoller, M. H., Shapiro, N. M., Pasyanos, M. E., Bensen, G. D., & Yang, Y. (2005). Short period surface wave dispersion measurements from ambient seismic noise in North Africa, the Middle East, and Central Asia. *Proceedings of the 27th Seismic Research Review: Ground-Based Nuclear Explosion Monitoring*, 20-22.

"Search Earthquake Archives", ANSS catalog, *United States Geological Survey*, accessed April 5th, 2015,
http://earthquake.usgs.gov/earthquakes/search/,

Shapiro, N. M., Campillo, M., Stehly, L., & Ritzwoller, M. H. (2005). High-resolution surface-wave tomography from ambient seismic noise. *Science*, *307*(5715), 1615-1618.

Shen, W., Ritzwoller, M. H., Schulte-Pelkum, V., & Lin, F. C. (2012). Joint inversion of surface wave dispersion and receiver functions: A Bayesian Monte-Carlo approach. *Geophysical Journal International*, ggs050.

Snieder, R. (2004). Extracting the Green's function from the correlation of coda waves: A derivation based on stationary phase. *Physical Review E*, *69*(4), 046610.

Su, H., Herrmann, R. B., Guo, H. (2015). Lithospheric structure beneath Northern Mississippi Embayment from joint inversion of surface wave dispersion and receiver functions. Master Thesis.

"Types of Earthquake Waves", *DOMUS* (*web page)*, accessed July 10th, 2015, http://allshookup.org/quakes/wavetype.htm

Van Der Lee, S., & G. Nolet (1997). Upper mantle S velocity structure of North America. *Journal of Geophysical Research: Solid Earth (1978–2012)*, *102*(B10), 22815-22838.

Viele, G. W., & Thomas, W. A. (1989). Tectonic synthesis of the Ouachita orogenic belt. *The Appalachian-Ouachita orogen in the United States: Geological Society of America, The Geology of North America*, *2*, 695-728.

Walker, J.D., Geissman, J.W., Bowring, S.A., and Babcock, L.E., compilers, 2012, Geologic Time Scale v. 4.0: *Geological Society of America*, doi: 10.1130/2012.CTS004R3C.

VITA

Hao Guo was born in Tianshui, Gansu Prov., China. After finishing the schoolwork at Changchen High school in 2007, He entered China University of Petroleum (Huadong) in Shandong Prov., China. Between 2010 and 2013, he studied geophysics at Missouri University of Science and Technology as a transfer student. He received two Bachelors of Science with a major in Geophysics from China University of Petroleum (Huadong) and Missouri University of Science and Technology in 2013, respectively. In the autumn of 2013, he started the graduate study with a major in Geophysics in Saint Louis University.